

Nanostructured Materials for Biomedical Applications

Guest Editors: Donglu Shi and Hongchen Gu





Nanostructured Materials for Biomedical Applications

Journal of Nanomaterials

Nanostructured Materials for Biomedical Applications

Guest Editors: Donglu Shi and Hongchen Gu



Copyright © 2008 Hindawi Publishing Corporation. All rights reserved.

This is a special issue published in volume 2008 of “Journal of Nanomaterials.” All articles are open access articles distributed under the Creative Commons Attribution License, which permits unrestricted use, distribution, and reproduction in any medium, provided the original work is properly cited.

Editor-in-Chief

Michael Z. Hu, Oak Ridge National Laboratory, USA

Advisory Board

James H. Adair, USA
C. Brinker, USA
Taeghwan Hyeon, South Korea
Nathan Lewis, USA

Ed Ma, USA
Alon V. McCormick, USA
Gary L. Messing, USA
Zhonglin Wang, USA

Enge Wang, China
Alan Weimer, USA
N. Xu, China
Jackie Ying, USA

Associate Editors

Xuedong Bai, China
John Bartlett, Australia
Theodorian Borca-Tasciuc, USA
Michael Harris, USA
Wanqin Jin, China
Do Kyung Kim, South Korea

Burtrand Lee, USA
S. J. Liao, China
Gong-Ru Lin, Taiwan
Jun Liu, USA
Sanjay Mathur, Germany
Nobuhiro Matsushita, Japan

Sherine Obare, USA
Maryam Tabrizian, Canada
Theodore T. Tsotsis, USA
Michael S. Wong, USA

Editorial Board

Donald A. Bansleben, USA
C. Brosseau, France
Siu Wai Chan, USA
Sang-Hee Cho, South Korea
C. Cui, China
Ali Eftekhari, Iran
Claude Estournes, France
Alan Fuchs, USA
Lian Gao, China
Hongchen Gu, China

Justin Holmes, Ireland
David Hui, USA
Rakesh K. Joshi, USA
Alan K. T. Lau, Hong Kong
Burtrand I. Lee, USA
Jun Li, Singapore
J. -Y. Liu, USA
Songwei Lu, USA
P. Panine, France
Donglu Shi, China

Bohua Sun, South Africa
Xiaogong Wang, China
Y. Wang, USA
Ching Ping Wong, USA
Ping Xiao, UK
Zhili Xiao, USA
Doron Yadlovker, Israel
Kui Yu, Canada

Contents

Nanostructured Materials for Biomedical Applications, Donglu Shi and Hongchen Gu
Volume 2008, Article ID 529890, 2 pages

Fibronectin Adsorption to Nanopatterned Silicon Surfaces, I. Salakhutdinov, P. VandeVord, O. Palyvoda, H. Matthew, G. Tatagiri, H. Handa, G. Mao, G. W. Auner, and G. Newaz
Volume 2008, Article ID 543170, 5 pages

Field Emission from Self-Assembled Arrays of Lanthanum Monosulfide Nanoprotrusions, V. Semet, Vu Thien Binh, M. Cahay, K. Garre, S. Fairchild, L. Grazulis, J. W. Fraser, D. J. Lockwood, S. Pramanik, B. Kanchibotla, and S. Bandyopadhyay
Volume 2008, Article ID 682920, 4 pages

Mesoporous Silica Coated CeF₃:Tb³⁺ Particles for Drug Release, Deyan Kong, Piaoping Yang, Zhenling Wang, Ping Chai, Shanshan Huang, Hongzhou Lian, and Jun Lin
Volume 2008, Article ID 312792, 7 pages

Nanostructural Organization of Naturally Occurring Composites—Part I: Silica-Collagen-Based Biocomposites, Hermann Ehrlich, Sascha Heinemann, Christiane Heinemann, Paul Simon, Vasily V. Bazhenov, Nikolay P. Shapkin, René Born, Konstantin R. Tabachnick, Thomas Hanke, and Hartmut Worch
Volume 2008, Article ID 623838, 8 pages

On the Complexity of Electrostatic Suspension Stabilization of Functionalized Silica Nanoparticles for Biotargeting and Imaging Applications, Lotta Bergman, Jessica Rosenholm, Anna-Brita Öst, Alain Duchanoy, Pasi Kankaanpää, Jyrki Heino, and Mika Lindén
Volume 2008, Article ID 712514, 9 pages

Atomic Layer Thermopile Materials: Physics and Application, P. X. Zhang and H.-U. Habermeier
Volume 2008, Article ID 329601, 12 pages

The Role of Filler-Matrix Interaction on Viscoelastic Response of Biomimetic Nanocomposite Hydrogels, Alireza S. Sarvestani, Xuezhong He, and Esmail Jabbari
Volume 2008, Article ID 126803, 9 pages

Effect of Carbon Nanofiber-Matrix Adhesion on Polymeric Nanocomposite Properties—Part II, Khalid Lafdi, William Fox, Matthew Matzek, and Emel Yildiz
Volume 2008, Article ID 310126, 8 pages

Low-Temperature Preparation of Amorphous-Shell/Nanocrystalline-Core Nanostructured TiO₂ Electrodes for Flexible Dye-Sensitized Solar Cells, Dongshe Zhang, Hengyao Hu, Laifeng Li, and Donglu Shi
Volume 2008, Article ID 271631, 4 pages

Nanostructural Organization of Naturally Occurring Composites—Part II: Silica-Chitin-Based Biocomposites, Hermann Ehrlich, Dorte Janussen, Paul Simon, Vasily V. Bazhenov, Nikolay P. Shapkin, Christiane Erler, Michael Mertig, René Born, Sascha Heinemann, Thomas Hanke, Hartmut Worch, and John N. Vournakis
Volume 2008, Article ID 670235, 8 pages

Editorial

Nanostructured Materials for Biomedical Applications

Donglu Shi^{1,2,3} and Hongchen Gu³

¹ *Department of Chemical and Materials Engineering, College of Engineering, University of Cincinnati, Cincinnati, OH 45221, USA*

² *The Institute for Advanced Materials and Nano Biomedicine, Tongji University, Shanghai 200092, China*

³ *Research Institute of Micro/Nano Science and Technology, Shanghai JiaoTong University, Shanghai 200240, China*

Correspondence should be addressed to Donglu Shi, shid@email.uc.edu

Received 9 September 2008; Accepted 9 September 2008

Copyright © 2008 D. Shi and H. Gu. This is an open access article distributed under the Creative Commons Attribution License, which permits unrestricted use, distribution, and reproduction in any medium, provided the original work is properly cited.

Current developments in nanostructured materials and nanotechnology will have profound impact in many areas such as energy technologies and biomedical applications. These include solar cells, energy storage, environmental control, tissue engineering, bioprobe, biomarking, cancer diagnosis, cancer therapy, and drug delivery. Many critical issues in nanostructured materials, particularly their applications in biomedicine must be addressed before clinical applications. Some of the key issues in biomedicine, deal with bioactivity, compatibility, toxicity, and nano-bio interfacial properties. In the biomedical applications, traditional materials science and engineering face new challenges in the synthesis and microstructure development since the requirements for general materials must be based on special medical needs. The most fascinating development in nano-biomedicine is to be found in biomedical diagnosis and treatment, and involves the direct use of nanomaterials within a biological system. Today, *in vivo* imaging by fluorescent nanoparticles such as quantum dots is progressing rapidly; and cell targeting via surface functionalized nanoparticles is undergoing animal tests and should be available within a few years. Localized drug delivery for tumor treatment by specially designed nanoscale systems is also being tested. Up to now, investigators have attempted to develop particular nanoscaled systems with surface functionalized groups that are able to conjugate with a variety of biological molecules including DNA, RNA, and viruses. These new technologies will also have significant potential in environmental monitoring, bio-probe, and quantitative virus detection. The challenge for future nano-biomedicine concerns how nanoparticles interface with biological systems with high biodegradability and minimum toxicity. We need to know how to design and synthesize nanoscale structures for a variety of medical and biological applications.

This special issue summarizes the most recent research and developments in nanostructured materials and their applications in a variety of applications. The articles in this issue address the critical problems in nanomaterials synthesis, structure, and properties. The special issue devotes several articles to various aspects of nanomaterials and biomedical applications. Detailed experimental procedures are presented in conjunction with biomedical considerations. Importantly, these articles give overviews of nanoscience and technology and the basic information relevant to the synthesis of nanomaterials. As nanoscience advances rapidly, extensive research activities have been emphasized on the design and development of new nanomaterials. Due to special requirements in both engineering and biomedicine, the materials developments have been directed to solving key problems that are different from those of traditional materials. For instance, medical diagnosis requires multifunctionality such that imaging and drug delivery are preferred to take place at the same time. Therefore, novel nanomaterials and technologies are needed for dealing with specific medical issues. Another critical issue deals with the nano- and biointerfaces involving nanoparticle surface functionalization. This is particularly important in nano-biocomposites. Functional groups must be deposited on the nanoparticles surfaces in order to conjugate biological molecules for purpose of targeting, virus detection, and drug delivery.

We intend this special issue of Journal of Nanomaterials to provide up-to-date information in the field of nanostructured materials and applications in nano-biomedicine. The focus of the special issue is on the basic concepts and recent developments in nanomaterials and related fields. This special issue covers a wide range of nanomaterials research for a variety of applications including biomedicine.

Fundamental understanding of basic mechanisms on nanostructures and biomedical processes related to the unique nanoscale properties of the materials will be the highlight of this special issue. All authors are prominent researchers and have extensive research experience in diverse fields of materials and biomedical sciences. We are grateful to them for these important contributions from which, we trust, many readers will benefit significantly.

Donglu Shi
Hongcheng Gu

Research Article

Fibronectin Adsorption to Nanopatterned Silicon Surfaces

I. Salakhutdinov,¹ P. VandeVord,² O. Palyvoda,¹ H. Matthew,^{2,3} G. Tatagiri,² H. Handa,³
G. Mao,^{2,3} G. W. Auner,^{1,2} and G. Newaz⁴

¹Electrical and Computer Engineering Department, Wayne State University, Detroit, MI 48202, USA

²Biomedical Engineering Department, Wayne State University, Detroit, MI 48202, USA

³Chemical Engineering and Material Science Department, Wayne State University, Detroit, MI 48202, USA

⁴Department of Mechanical Engineering, College of Engineering, Wayne State University, Detroit, MI 48202, USA

Correspondence should be addressed to I. Salakhutdinov, ildar@eng.wayne.edu

Received 14 September 2007; Accepted 26 December 2007

Recommended by Donglu Shi

The possibility of using surface topography for guidance of different biological molecules and cells is a relevant topic that can be applied to a wide research activity. This study investigated the adsorption of fibronectin to a diffraction grating silicon surface. The rectangular grating profile featured a controlled surface with 350 nm period and a corrugation depth of 90 nm. Results demonstrated that the controlled surface had a significantly positive effect on the fibronectin binding. Thus, nanoscale surface topography can enhance fibronectin binding.

Copyright © 2008 I. Salakhutdinov et al. This is an open access article distributed under the Creative Commons Attribution License, which permits unrestricted use, distribution, and reproduction in any medium, provided the original work is properly cited.

1. INTRODUCTION

The possibility of using surface topography for guidance of different biological molecules and cells is a relevant topic that can be applied to a wide research activity [1]. One important subject is the attachment of various plasma and extracellular proteins to biomaterial surfaces [2]. Fibronectin (FN) is a well defined extracellular protein consisting of two dimer subunits, each is about 250 kilodaltons (kD) and an elongated shape with dimensions 45 nm × 9 nm × 6 nm [3]. FN plays a key role in cell adhesion and mediating cell response, thus it will be used as a model for protein adherence in our study. Although FN adsorption on different materials has been investigated very actively, it has not been identified how FN adherence is altered in response to nano- and micropattern roughness. We used diffraction grating on silicon substrate as controllable roughness to investigate alterations in FN adsorption. Diffraction grating fabrication technologies are well developed, thus it is possible to fabricate diffraction gratings with a wide range of grating periods, corrugation depth, and grating profile.

Many engineering applications have focused on biomimetic sensors based on waveguide technology. Considering new advances in microelectromechanical systems/na-

noelectromechanical systems (MEMS/NEMS) fabrication, soft lithography, and the development of smart adhesives, integration of complementary metal-oxide-semiconductor (CMOS) and MEMS/NEMS should be further explored to provide the infrastructure for integration of the whole silicon-based sensory system especially in controlling host-biomaterial interactions. Any attempt to make a sophisticated, functional surface for biointeractions must take into account the highly developed ability of biological systems to recognize specially designed features on the molecular scale [4]. The materials used in BioMEMS/BioNEMS devices must exhibit desirable micro-/nanoscale tribological and mechanical properties [5]. From the cellular perspective, the interactions of cells with each other and extracellular materials (proteins, matrices, solid surfaces, etc.) are of vital importance to proper cell functioning. These interactions have major effects on the proliferation, differentiation, migration, and organization of cells [6, 7]. When designing novel biomaterials properties, one must understand that when an implant surface comes into contact with physiological solutions, proteins adsorb immediately on material surface. This adsorption is known to cause conformational changes in the native protein structure with the possibility of subsequently promoting or inhibiting nearby cells to interact with material,

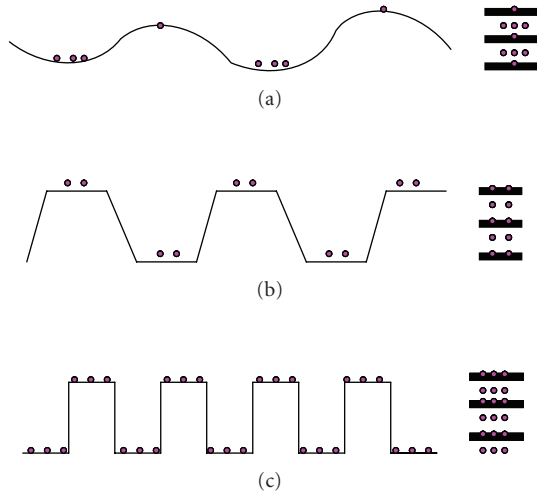


FIGURE 1: Attachment model for different diffraction grating profiles.

thus leading to implant integration or rejection [4, 6, 8]. Recent studies on protein/material surface interactions have increased the knowledge base on this topic and this relationship appears to be mediated by a class of high molecular weight glycoproteins that are involved both in these interactions and in the actual structure of extracellular matrices. Some of the most intensively studied glycoproteins are FN, laminin, Willebrand protein, thrombospondin, and vitronectin [9–11]. The general structural outline of FN consists of a dimer of two subunits, each is about 250 kilodaltons (kD) [12]. Each subunit is folded into an elongated and flexible arm 60 nm long, and the two subunits are joined by disulfide bonds very near their C-termini. Within each subunit, there is a series of tightly folded globular domains; each specialized for binding to other molecules such as collagen, glycosaminoglycans, transglutaminase, or to cellular membrane receptors [13, 14]. Since it is known that cells may never see the native biomaterial, the configuration of the absorbed proteins is of utmost importance in cell activation and response. By optimally designing a surface for a specific protein conformational change, we must take into account how the protein 3D topography and chemical structure will affect its absorption onto the material surface. To further investigate the phenomenon of protein adsorption and the effect of nanoscale modulation of the surface, we chose to examine how nanoscale modulation affects FN binding to silicon surfaces.

2. GRATING CHARACTERIZATION

As mentioned, the mechanisms of protein absorption to patterned structures are not clear yet. We chose diffraction grating technology for two reasons. Firstly, there are several results with regards to the role of periodic structures positively affecting the attachment of biological objects, with emphasis on cells [15, 16]. Secondly, diffraction gratings are one of the most widely used optical instruments that are very well inves-

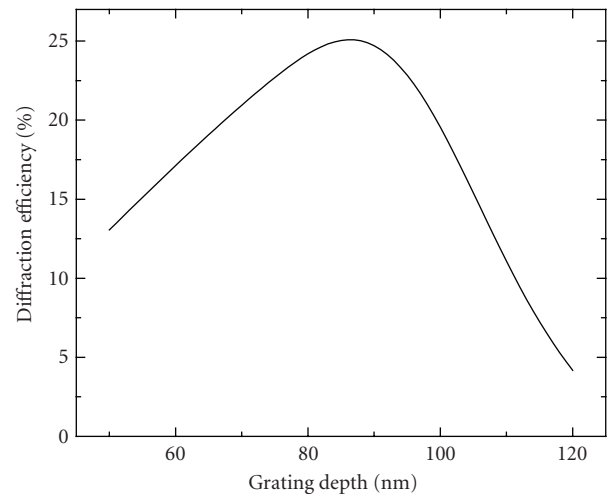


FIGURE 2: Diffraction efficiency at 1st order dependence versus the corrugation depth.

tigated both theoretically and practically. Diffraction grating technologies are recognized to permit for a defined grating period, corrugation profile, and corrugation depth.

There are three main practical diffraction grating profiles: sinusoidal, trapezoidal, and rectangular. Figure 1 presents a simplified model for optimal grating profile and hypothesized protein attachment based on assumptions described in [17].

The next parameter to determine is corrugation depth. We expect that optimal corrugation depth will correspond to the maximum of diffraction efficiency. Figure 2 presents results of calculations of diffraction efficiency versus the corrugation depth made by modified C-method [18].

In total, we decided to use nanopatterned surfaces with a period about 350 nm (175 nm plateaus and 175 nm valleys), a corrugation depth about 90 nm and rectangular grating profile to explore protein adsorption onto silicon surfaces.

3. TECHNOLOGY AND EXPERIMENT

3.1. Grating fabrication

P(boron)-type silicon wafers from Silicon Quest International, (Santa Clara, Calif, USA), with $\langle 1-0-0 \rangle$ orientation with thickness equal to 510–540 μm ; material resistivity was 4–20 $\Omega\text{-cm}$, were utilized for this study. Diffraction gratings were fabricated by optical holography. As a laser source, we used Coherent INNOVA 300C FReD Ar laser with frequency doubling. The diffraction grating was fabricated on the silicon substrates by holography with UV5 photoresist as a mask material. The mask structures were etched by RIE DryTek system at the following conditions: C_2F_6 —40 sccm; O_2 —8 sccm; RF power—120 W; pressure—223 mTorr. These conditions resulted in diffraction gratings with rectangular profile having size of 3 mm \times 5 mm within the total 10 mm \times 10 mm silicon substrate.

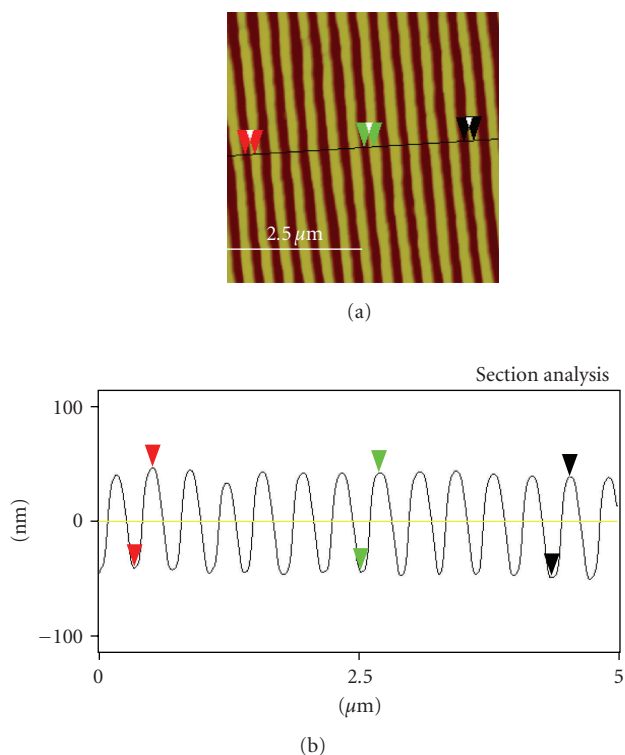


FIGURE 3: AFM image of fabricated diffraction grating used as controllable rough surface and the sectional height profile along the line.

3.2. Atomic force microscope (AFM) and scanning electron microscope (SEM) measurements

In order to assess surface topography of the grated surfaces, AFM (Nanoscope III, Digital Instruments/VEECO) was used. All the AFM images were obtained using an E scanner with maximum scan area $14.2 \times 14.2 \mu\text{m}^2$. Height, deflection, and friction images were obtained in contact mode in ambient air with silicon nitride tips (NP, VEECO). The scan rate used was 0.8–1 Hz. Integral and proportional gains were approximately 2.0 and 3.0, respectively. Figure 3 presents an example of AFM measurements for the fabricated gratings. It is very important that our samples have highly homogeneous nanopatterned structure. Five different areas of the diffraction grating were analyzed to check the periodicity and the depth of the grating. Nanoscope software was used to analyze the images. Using sectional analysis, the periodicity of the grating was found to be $355 \text{ nm} \pm 0.08 \text{ nm}$ and the height was found to be $87 \text{ nm} \pm 3 \text{ nm}$ (Height information might not be very accurate as may be the tip is not reaching the bottom most point of the grating).

In order to verify AFM measurements, we made SEM image of the fabricated grating. These measurements confirmed the high uniformity of the fabricated gratings; this is an important factor for our biomedical research.

In summary, the grating was found to be highly uniform in periodicity and height at various places. A 2D image of a two-dimensional grating is shown in Figure 5. The homo-

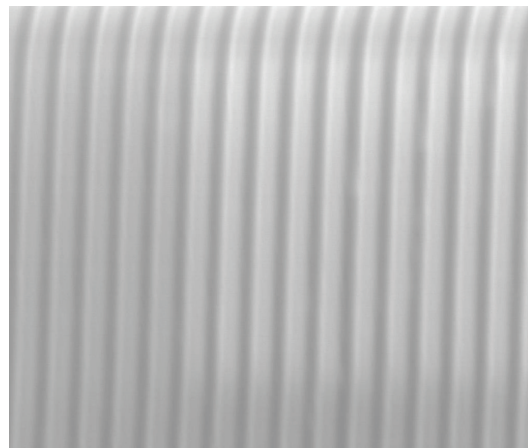


FIGURE 4: SEM image of the fabricated grating.

geneity was demonstrated to be 0.02% for the grating period and 2.0% for the grating corrugation depth.

3.3. Protein adsorption assay

Prior to protein adsorption, all silicon samples were cleaned via the RCA cleaning procedure. After which, human FN (Sigma, St. Louis, Mo, USA) was reconstituted to a final concentration of $10 \mu\text{g}/\text{ml}$ in phosphate buffered saline (PBS). Protein was adsorbed onto experimental silicon surfaces by immersion in the prepared FN solution for 2 hours at room temperature with gentle rotation. Additional samples were also immersed in PBS solution without protein to be used as control surfaces. After incubation, the solutions were removed and the samples were carefully washed 3 times with PBS to eliminate any unbound protein. Care was taken in order to prevent the drying of the protein-coated surfaces before further analysis.

3.4. Immunodetection of adsorbed proteins

Patterned and control surfaces were removed from PBS and incubated with 2% bovine serum albumin (BSA; Sigma, St. Louis, Minn, USA) solution for 2 hours in room temperature in order to block later nonspecific antibodies binding. Immunostaining procedure was performed with FN chicken antihuman antibodies (Invitrogen, Chicago, Ill, USA) diluted 1 : 1000. Following a PBS wash, samples were then incubated for 2 hours with an Alexa Fluor 488 goat antichicken IgG (H+L) (Invitrogen, Chicago Ill, USA) diluted 1 : 200. Both primary and secondary antibodies were individually diluted in PBS with 1% BSA. Between each step of the immunostaining procedure, samples were repeatedly washed with PBS. For each assay, an additional control was prepared consisting of a protein-coated sample submitted to the same described procedure but instead of incubating with the primary antibody, PBS was used. Thus, the protein-coated samples were exposed to the secondary antibody only as a control. Subsequently, the silicon wafers were mounted on glass slides using ProLong Gold Antifade reagent (Invitrogen,

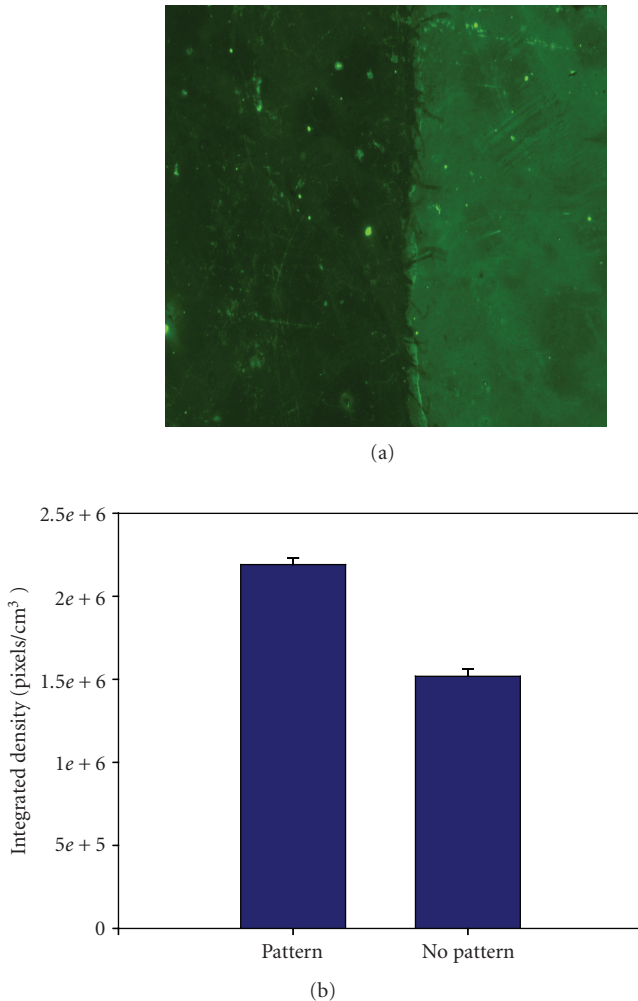


FIGURE 5: (a) Fluorescence micrograph of the border between the patterned surface (right) and the nonpatterned surface (left) (200x). (b) Graph depicts the average pixel density from the fluorescence microscopy analysis.

Chicago Ill, USA). Immunostaining results were observed and recorded using fluorescent microscope (Nikon Eclipse TE2000-U). Ten digital images of each sample ($n = 3$) were captured and analyzed for average pixel intensity on both the patterned and nonpatterned areas using Image J Software. The results demonstrated a significantly higher ($P = 01$) level of fluorescence on the patterned area as compared to the nonpatterned surface (Figure 4). These results strongly indicate a higher level of FN protein attachment occurring on the patterned surface as compared to the nonpatterned surface.

3.5. Further development

The mechanisms of why there was an increase in protein attachment on the patterned surfaces are not clear yet. Thus it will be interesting to investigate variations in nanopatterned structures (size and shapes) which could be effective for alterations in protein attachment. After fabrication of 1D diffraction grating by deep UV lithography, we also fabricated 2D

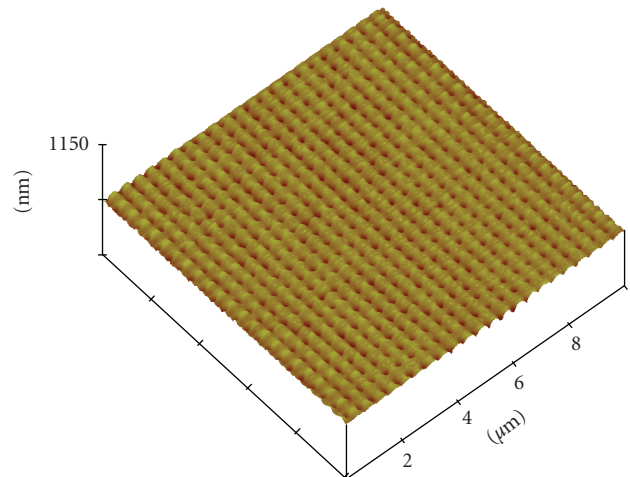


FIGURE 6: 2D diffraction grating with grating period $\Lambda = 351.2$ nm.

gratings with the same period $\Lambda = 351.2$ nm in both coordinates (Figure 5).

To fabricate such structures, we simply exposed the surface twice. Prior to the second exposure, we rotated structure on 90° . We expect that 2D gratings will give another prospective structure for examining changes in protein adsorption. It has been shown that 2D periodical structure is a good candidate for using of tuning localized plasmons for the surface-enhanced Raman scattering [19]. Future studies will compare protein adhesion of 1D and 2D nanopatterned surfaces.

4. DISCUSSION

FN is a representative of a cell adhesion protein that is present in both plasma and the extracellular matrix. Altering the attachment of this protein suggests that our nanopatterned structures may lead to changes in the acceptance level of biomaterials by the host. Rechendorff et al. proposed that protein shape effects its interaction with biomaterial surface [20]. They created random nanosize rough surface by evaporation of tantalum films, with surface roughness in the range between 2.0 and 32.9 nm. They determined that fibrinogen, due to of its elongated shape, is much more sensitive to the surface roughness as compared to bovine serum albumin, a protein which has a nearly globular shape.

5. CONCLUSIONS

We proposed a simple model for protein attachment regarding grating corrugation profile. From our model, we examined diffraction gratings with rectangular grating profile.

We found that diffraction grating could serve as a controlled rough surface for FN. Our results strongly indicate a higher level of FN attachment occurring on the patterned surface. Thus the nanopatterned surface has a significant positive effect on the binding of FN.

Such a positive result for FN, which plays a key role in cell adhesion and mediating cell response, proves that

cell attachment could be improved on investigated nanopatterned structures.

ACKNOWLEDGMENTS

Authors want to thank Professor Ivan Avrutsky of ECE Department of Wayne State University for his assistance and useful discussions. Funding for this work was provided by Wayne State University Research Office through the Nanotechnology Initiative. The AFM part of the work was partially supported by the National Science Foundation (CTS-0553533).

REFERENCES

- [1] C. S. Chen, M. Mrksich, S. Huang, G. M. Whitesides, and D. E. Ingber, "Geometric control of cell life and death," *Science*, vol. 276, no. 5317, pp. 1425–1428, 1997.
- [2] S. Yamamoto, M. Tanaka, H. Sunami, et al., "Relationship between adsorbed fibronectin and cell adhesion on a honeycomb-patterned film," *Surface Science*, vol. 600, no. 18, pp. 3785–3791, 2006.
- [3] F. Höök, J. Vörös, M. Rodahl, et al., "A comparative study of protein adsorption on titanium oxide surfaces using in situ ellipsometry, optical waveguide lightmode spectroscopy, and quartz crystal microbalance/dissipation," *Colloids and Surfaces B*, vol. 24, no. 2, pp. 155–170, 2002.
- [4] B. Kasemo, "Biological surface science," *Surface Science*, vol. 500, no. 1–3, pp. 656–677, 2002.
- [5] B. Bhushan, D. R. Tokachichu, M. T. Keener, and S. C. Lee, "Morphology and adhesion of biomolecules on silicon based surfaces," *Acta Biomaterialia*, vol. 1, no. 3, pp. 327–341, 2005.
- [6] L. Tang, "Mechanisms of fibrinogen domains: biomaterial interactions," *Journal of Biomaterials Science. Polymer Edition*, vol. 9, no. 12, pp. 1257–1266, 1998.
- [7] L. Stryer, *Biochemistry*, W. H. Freeman, New York, NY, USA, 1998.
- [8] C. M. Alves, R. L. Reis, and J. A. Hunt, "Preliminary study on human protein adsorption and leukocyte adhesion to starch-based biomaterials," *Journal of Materials Science: Materials in Medicine*, vol. 14, no. 2, pp. 157–165, 2003.
- [9] D. Couchourel, C. Escoffier, R. Rohanizadeh, et al., "Effects of fibronectin on hydroxyapatite formation," *Journal of Inorganic Biochemistry*, vol. 73, no. 3, pp. 129–136, 1999.
- [10] D. Pellenc, H. Berry, and O. Gallet, "Adsorption-induced fibronectin aggregation and fibrillogenesis," *Journal of Colloid and Interface Science*, vol. 298, no. 1, pp. 132–144, 2006.
- [11] D. J. Romberger, "Fibronectin," *The International Journal of Biochemistry & Cell Biology*, vol. 29, no. 7, pp. 939–943, 1997.
- [12] R. O. Hynes, "Molecular biology of fibronectin," *Annual Review of Cell Biology*, vol. 1, pp. 67–90, 1985.
- [13] R. O. Hynes and K. M. Yamada, "Fibronectins: multifunctional modular glycoproteins," *Journal of Cell Biology*, vol. 95, no. 2, pp. 369–377, 1982.
- [14] D. F. Mosher, "Cross-linking of fibronectin to collagenous proteins," *Molecular and Cellular Biochemistry*, vol. 58, no. 1–2, pp. 63–68, 1984.
- [15] M. J. Dalby, D. McCloy, M. Robertson, C. D. W. Wilkinson, and R. O. C. Oreffo, "Osteoprogenitor response to defined topographies with nanoscale depths," *Biomaterials*, vol. 27, no. 8, pp. 1306–1315, 2006.
- [16] A. M. P. Turner, N. Dowell, S. W. P. Turner, et al., "Attachment of astroglial cells to microfabricated pillar arrays of different geometries," *Journal of Biomedical Materials Research*, vol. 51, no. 3, pp. 430–441, 2000.
- [17] R. A. Freitas Jr., *Nanomedicine, Volume IIA: Biocompatibility*, Landes Bioscience, Georgetown, Tex, USA, 2003.
- [18] L. Li, J. Chandezon, G. Granet, and J.-P. Plumey, "Rigorous and efficient grating-analysis method made easy for optical engineers," *Applied Optics*, vol. 38, no. 2, pp. 304–313, 1999.
- [19] N. M. B. Perney, J. J. Baumberg, M. E. Zoorob, M. D. B. Charlton, S. Mahnkopf, and C. M. Netti, "Tuning localized plasmons in nanostructured substrates for surface-enhanced Raman scattering," *Optics Express*, vol. 14, no. 2, pp. 847–857, 2006.
- [20] K. Rechendorff, M. B. Hovgaard, M. Foss, V. P. Zhdanov, and F. Besenbacher, "Enhancement of protein adsorption induced by surface roughness," *Langmuir*, vol. 22, no. 26, pp. 10885–10888, 2006.

Research Article

Field Emission from Self-Assembled Arrays of Lanthanum Monosulfide Nanoprotrusions

V. Semet,¹ Vu Thien Binh,¹ M. Cahay,² K. Garre,² S. Fairchild,³ L. Grazulis,³ J. W. Fraser,⁴
D. J. Lockwood,⁴ S. Pramanik,⁵ B. Kanchibotla,⁵ and S. Bandyopadhyay⁵

¹Equipe Emission Electronique, LPCMN-CNRS, Universite Claude Bernard Lyon 1, 69622 Villeurbanne, France

²Department of Electrical and Computer Engineering and Computer Science, University of Cincinnati, Cincinnati, OH 45221, USA

³Materials and Manufacturing Directorate, Air Force Research Laboratory, Wright-Patterson AFB, OH 45433, USA

⁴Institute for Microstructural Sciences, National Research Council, Ottawa, ON, Canada K1A 0R6

⁵Department of Electrical and Computer Engineering, Virginia Commonwealth University, Richmond, VA 23284, USA

Correspondence should be addressed to M. Cahay, marc.cahay@uc.edu

Received 30 October 2007; Accepted 10 January 2008

Recommended by Donglu Shi

The field emission properties of LaS nanoprotrusions called nanodomes, formed by pulsed laser deposition on porous anodic alumina films, have been analyzed with scanning anode field emission microscopy. The voltage necessary to produce a given field emission current is ~ 3.5 times less for nanodomes than for thin films. Assuming the same work function for LaS thin films and nanoprotrusions, that is, ~ 1 eV, a field enhancement factor of ~ 5.8 is extracted for the nanodome emitters from Fowler-Nordheim plots of the field emission data. This correlates well with the aspect ratio of the tallest nanodomes observed in atomic force micrograph measurements.

Copyright © 2008 V. Semet et al. This is an open access article distributed under the Creative Commons Attribution License, which permits unrestricted use, distribution, and reproduction in any medium, provided the original work is properly cited.

The promise of producing extremely high current densities in near-vacuum with no external source (such as heater, primary electron-beam, or intense light source) has generated significant interest in robust, reproducible, and field-emission-based cold cathodes [1, 2]. Several promising approaches to achieving cold cathode emission from a dense array of nanoscale field emitters have been investigated including metallic field emitter arrays (FEAs) or Spindt emitters [3], carbon nanotube (CNT) arrays [4], and arrays of semiconductor nanowires [5–9]. To date, metallic FEAs with uniformly high emission have been difficult to fabricate. They are prone to failure and present long-term reliability problems [3]. Carbon nanotubes (CNTs), on the other hand, can be fabricated easily, but the emission current density that they can support, while adequate for some applications, is currently not enough for mainstream high power devices such as traveling wave tubes (TWTs). Semiconductor and semimetallic nanowires therefore appear as perhaps the most promising route to realizing field emitters that can support a large total emission current, in particular if regular high density arrays of them can be fabricated in a self-assembled

growth mode. Moreover, to achieve high current densities under low applied voltage, the field emitter material must have low work function. Rare earth monosulfides are therefore ideal for this purpose.

Recently, we reported the first successful deposition of lanthanum monosulfide (LaS) thin films on Si substrates using pulsed laser deposition (PLD) [10, 11]. They were flat layers composed of nanocrystallites having dimensions of the order of 5 nm. The scanning anode field emission microscopy (SAFEM) technique was used to measure the field emission (FE) properties of these LaS thin films (about $0.1 \mu\text{m}$ thick) [12]. It was shown experimentally that electrons are easily extracted by FE from patchwork areas of few nanometer dimensions having a measured effective work function of ~ 1 eV, corresponding to some outcropping LaS nanocrystallites with (100) orientation, embedded in a ~ 2.8 eV work function surface related to other crystallographic orientations. A LaS thin film obtained by PLD can therefore be an excellent field emitter material, especially if we can take advantage of a field enhancement factor at the tip of nanoscale protrusions formed from such material.

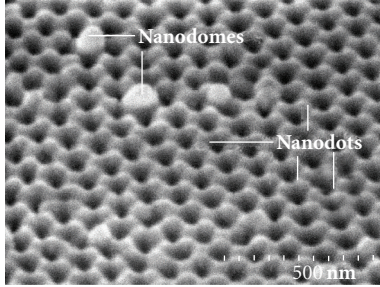


FIGURE 1: FE-SEM images of a $1 \times 1 \mu\text{m}^2$ area of an anodic porous alumina film after PLD of LaS. The nanoprotusions are the nanodomes and nanodots indicated in the figure.

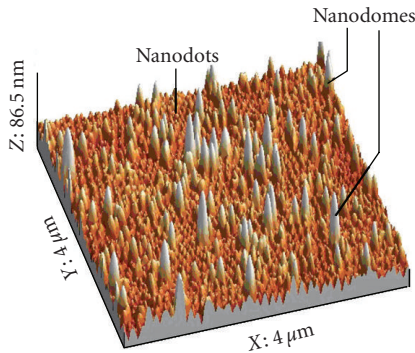


FIGURE 2: Three-dimensional AFM image of an area of $4 \times 4 \mu\text{m}^2$ of the alumina template after PLD of LaS. The tallest irregular features are the LaS nanodomes. The smaller and more regular pyramidal structures are the LaS nanodots forming in the regions between adjacent pores.

In this letter, we report FE properties of arrays of LaS nanoprotusions self-assembled with a density as high as $10^9/\text{cm}^2$. These nanoprotusions, called nanodomes and nanodots hereafter, are produced when LaS is pulse-laser-deposited on nanoporous anodic alumina films containing hexagonal arrays of cylindrical pores that are ~ 50 nm wide and ~ 500 nm deep. The details of the self-assembly growth of arrays of nanoprotusions using a porous anodic alumina film as a template are given in [13].

The nanodomes are cone-shaped LaS structures with base diameter $2r$ ranging from 50 to 100 nm and height h ranging from 100 to 150 nm. They were found to grow on the boundaries separating regions of the anodic alumina film that have near perfect pore ordering. Their density is $\sim 10^9/\text{cm}^2$, as extracted from the field emission-scanning electron micrographs (FE-SEM) and atomic force micrographs (AFM) such as those shown in Figures 1 and 2, respectively. In addition to nanodomes, nanodots (or quantum dots) of LaS nucleate on top of the alumina islands between adjacent pores. These are sites of minimal strain. The dots have a diameter $2r \sim 50$ nm, a density equal to the pore density ($10^{10}/\text{cm}^2$), and an aspect ratio $h/2r$ less than 1.

The SAFEM technique was used to measure the FE current-voltage (I - V) characteristics at different surface locations. As the nanowires are buried inside the pores, they

contribute very little, if any at all, to the net FE current. Moreover, FE measurements from the arrays of nanodomes and nanodots were possible because the regions joining adjacent nanodomes and nanodots are covered with a thin percolating network of LaS over the entire array. Its presence was confirmed by measuring a low resistance value of about 2 Ohms between two electrical contacts about 1 cm apart. For each location, a full set of I - V characteristics (total measured current versus applied voltage) for different values of d , the distance between the cathode surface and the probe ball, was measured. This set of measurements was then analyzed in order to extract the apparent current density αJ versus actual applied local field γF , where γ is the local geometrical field enhancement at the surface of the cathode [14], F is the notional electric field at the corresponding flat LaS cathode surface (when $\gamma = 1$), α a factor taking into account the actual emitting area, and J the notional FE current density. In Figure 2, we see that the nanodome structures dominate the landscape and therefore they have the highest field enhancement factor γ . The relative contribution of the nanodots to the total FE current is minor due to a smaller value of the γ associated with them. In all probability, the majority of the measured FE current is then extracted from the highest nanodomes.

In order to assess the FE properties from LaS nanoprotusions, we have compared the FE from nanodome cathodes with that from planar thin film LaS cathodes. This comparative methodology was chosen because a precise quantitative estimation of γ from topographic measurements is still subject to controversy, except for a flat surface. These experimental measurements were performed for both LaS thin films of 100 nm thickness on Si wafers and LaS nanodomes on anodic alumina films. The analysis consisted of the following steps.

- (1) In order to restrict the analysis of the differences in the I - V data to the surface morphology of the cathodes, both SAFEM measurements were performed with the same probe ball-to-cathode distance $d = 3.65 \mu\text{m}$. Typical I - V characteristics are shown in Figure 3 for both thin film and nanodome cathodes. We found that in order to extract the same total FE current, the applied voltage for nanodome cathodes was ~ 3.5 times less than that for thin film cathodes. This indicates clearly the contribution of the protruding geometry of the nanodomes to the FE current.
- (2) The total FE current versus applied voltage (I - V) characteristics were measured for different values of the probe-ball-to-cathode-surface distance d . From these data, the apparent current densities ($\alpha_{tf}J$ and $\alpha_{nd}J$) as a function of the applied local field were extracted [15, 16], assuming that the applied local electric field included the local enhancement factor γ , that is, $\gamma_{tf}F$ and $\gamma_{nd}F$, for LaS thin film and nanodome cathodes, respectively. α_{tf} and α_{nd} are parameters taking into account the actual emitting areas from low work function nanocrystallite zones [12] and the density of emitting nanodomes. The corresponding Fowler-Nordheim plots ($\ln(\alpha J/(\gamma F)^2)$ versus $1/\gamma F$) of the data are shown in Figure 4. As a result of the field

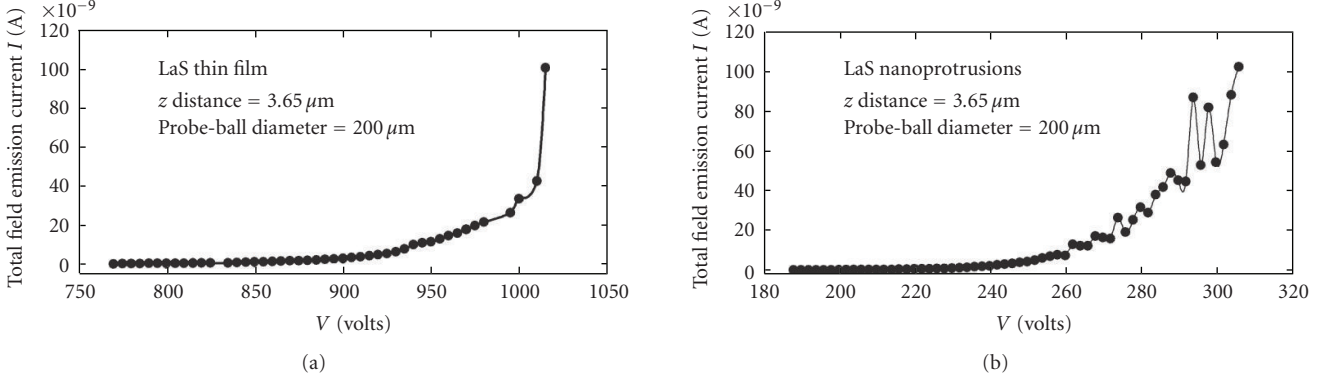


FIGURE 3: (a) Typical I - V characteristic recorded using the SAFEM technique for FE from LaS thin film deposited via PLD on a Si substrate. (b) The same for LaS nanostructures self-assembled on a porous anodic alumina template. To allow immediate comparison, the sample to SAFEM probe distance is kept the same in both measurements.

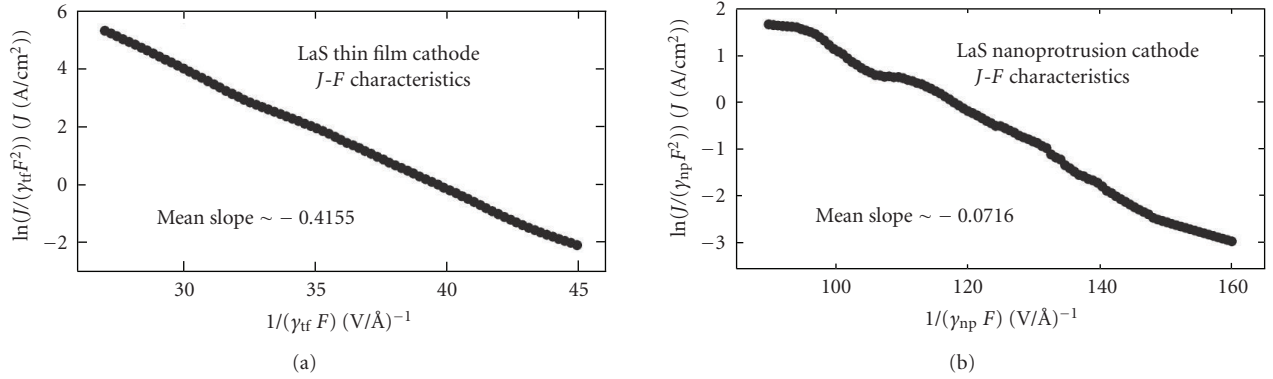


FIGURE 4: Fowler-Nordheim plots of the FE data corresponding to the cathodes shown in Figure 3.

enhancement factor, the emission area for nanodome cathodes was restricted to the nanodome apices. The actual current densities J extracted from each nanodome are then much more important than the values of the apparent current densities in the plot of Figure 4. The exact estimation of the ratio α_{nd}/α_{tf} would require a self-consistent approach, which is in progress, but one can estimate it in first approximation to be proportional to the inverse of the density of the emitting nanodomains. This ratio could be in the range of 10^4 to 10^5 .

- (3) The FE analysis for both cathodes, presented in the previous paragraph, was limited only to the region where the analytical FE relation developed by Murphy and Good is applicable [15, 16]. Under such conditions, the slopes m_{tf} and m_{nd} of the Fowler-Nordheim plots are, respectively, proportional to $\Phi^{3/2}/\gamma_{tf}$ and $\Phi^{3/2}/\gamma_{nd}$, where Φ is the effective work function of the cathodes. In Figure 4, a straight line fit to the Fowler-Nordheim plots of the data gave slope values $m_{tf} = -0.4155$ and $m_{nd} = -0.0716$ for LaS/Si and nanodome cathodes, respectively.
- (4) Under the assumption that the nanodome cathodes have the same effective work function as the planar

cathodes on Si, that is, $\Phi \sim 1\text{eV}$, [12] the ratio of the slopes extracted from the Fowler-Nordheim plots is equal to the inverse ratio of the field enhancement factors. Since AFM measurements of LaS thin films on Si substrates have shown that surface corrugation is negligible [10, 11], the error introduced by taking $\gamma_{tf} = 1$ is minor. Under this assumption, $\gamma_{nd} = 5.8$. This value is in very good agreement with the geometrical aspect ratio of the tallest nanodomains observed by AFM [13].

In conclusion, the SAFEM technique was used to demonstrate successful FE from LaS nanodomains grown by PLD on top of flexible alumina templates. The SAFEM measurements were found to be reproducible after a period of several months without taking any special precaution to store the template. LaS nanodome arrays are therefore very stable field emitters with a work function around 1 eV. Even though not discussed here, cross sectional FE-SEM images have shown that LaS nanowires grow inside the pores with a density of $10^{10}/\text{cm}^2$. The nanowires have a diameter of 50 nm and a maximum length equal to the length of the pores (~ 500 nm) [13]. This density could approach $10^{11}/\text{cm}^2$ by using templates with pores size down to 10 nm. Actually, the exposure of the tips of the LaS nanowires filling the pores can be done by etching the back aluminum substrate and the

small alumina barrier at the bottom of the pores, which could lead to field enhancement factors for the LaS nanowires more comparable to those reported for CNTs. This would lead to a much lower threshold voltage for field emission compared to the one reported here and a large increase in the density of nanoemitters culminating in the realization, therefore the realization of flexible cold cathodes using a self-assembling process with reliable and low cost production.

ACKNOWLEDGMENT

The work at the University of Cincinnati and Virginia Commonwealth University is financially supported by the US National Science Foundation under the collaborative GOALI Grant ECS-0523966. Part of this work was performed by M. Cahay under the Air Force Summer Fellowship Program, Contract No. FA9550-07-C-0052.

REFERENCES

- [1] A. G. Rinzler, J. H. Hafner, P. Nikolaev, et al., "Unraveling nanotubes: field emission from an atomic wire," *Science*, vol. 269, no. 5230, pp. 1550–1553, 1995.
- [2] R. H. Baughman, A. A. Zakhidov, and W. A. de Heer, "Carbon nanotubes—the route toward applications," *Science*, vol. 297, no. 5582, pp. 787–792, 2002.
- [3] D. Temple, "Recent progress in field emitter array development for high performance applications," *Materials Science and Engineering R*, vol. 24, no. 5, pp. 185–239, 1999.
- [4] M. Mauger, V. T. Binh, A. Levesque, and D. Guillot, "Free-standing vertically aligned arrays of individual carbon nanotubes on metallic substrates for field emission cathodes," *Applied Physics Letters*, vol. 85, no. 2, pp. 305–307, 2004.
- [5] Y. B. Li, Y. Bando, D. Golberg, and K. Kurashima, "Field emission from MoO₃ nanobelts," *Applied Physics Letters*, vol. 81, no. 26, pp. 5048–5050, 2002.
- [6] Y.-H. Lee, C.-H. Choi, Y.-T. Jang, et al., "Tungsten nanowires and their field electron emission properties," *Applied Physics Letters*, vol. 81, no. 4, pp. 745–747, 2002.
- [7] J. Chen, S. Z. Deng, N. S. Xu, et al., "Field emission from crystalline copper sulphide nanowire arrays," *Applied Physics Letters*, vol. 80, no. 19, pp. 3620–3622, 2002.
- [8] C. Y. Zhi, X. D. Bai, and E. G. Wang, "Synthesis and field-electron-emission behavior of aligned GaAs nanowires," *Applied Physics Letters*, vol. 86, no. 21, Article ID 213108, 3 pages, 2005.
- [9] R. C. Wang, C. P. Liu, J. L. Huang, S.-J. Chen, Y.-K. Tseng, and S.-C. Kung, "ZnO nanopencils: efficient field emitters," *Applied Physics Letters*, vol. 87, no. 1, Article ID 013110, 3 pages, 2005.
- [10] S. Fairchild, J. Jones, M. Cahay, et al., "Pulsed laser deposition of lanthanum monosulfide thin films on silicon substrates," *Journal of Vacuum Science & Technology B*, vol. 23, no. 1, pp. 318–321, 2005.
- [11] M. Cahay, K. Garre, X. Wu, D. Poitras, D. J. Lockwood, and S. Fairchild, "Physical properties of lanthanum monosulfide thin films grown on (100) silicon substrates," *Journal of Applied Physics*, vol. 99, no. 12, Article ID 123502, 6 pages, 2006.
- [12] V. Semet, M. Cahay, V. T. Binh, S. Fairchild, X. Wu, and D. J. Lockwood, "Patchwork field emission properties of lanthanum monosulfide thin films," *Journal of Vacuum Science & Technology B*, vol. 24, no. 5, pp. 2412–2416, 2006.
- [13] M. Cahay, K. Garre, J. W. Fraser, et al., unpublished.
- [14] R. G. Forbes, C. J. Edgcombe, and U. Valdrè, "Some comments on models for field enhancement," *Ultramicroscopy*, vol. 95, pp. 57–65, 2003.
- [15] V. Semet, R. Mouton, and V. T. Binh, "Scanning anode field emission microscopy analysis for studies of planar cathodes," *Journal of Vacuum Science & Technology B*, vol. 23, no. 2, pp. 671–675, 2005.
- [16] V. Semet, C. Adessi, and V. T. Binh, "Field emission from low barrier surface cathodes," in *Proceedings of the 19th International Vacuum Nanoelectronics Conference, and the 50th International Field Emission Symposium (IVNC/IFES '06)*, pp. 25–26, Guilin, China, July 2006.

Research Article

Mesoporous Silica Coated $\text{CeF}_3:\text{Tb}^{3+}$ Particles for Drug Release

Deyan Kong,^{1,2} Piaoping Yang,¹ Zhenling Wang,¹ Ping Chai,¹ Shanshan Huang,¹
Hongzhou Lian,¹ and Jun Lin¹

¹ State Key Laboratory of Application of Rare Earth Resources, Changchun Institute of Applied Chemistry,
Chinese Academy of Sciences, Changchun 130022, China

² Graduate School of the Chinese Academy of Sciences, Beijing 100049, China

Correspondence should be addressed to Jun Lin, jlin@ciac.jl.cn

Received 5 March 2007; Revised 10 July 2007; Accepted 6 August 2007

Recommended by Donglu Shi

$\text{CeF}_3:\text{Tb}^{3+}$ nanoparticles were successfully prepared by a polyol process using diethylene glycol (DEG) as solvent. After being coated with dense silica, these $\text{CeF}_3:\text{Tb}^{3+}$ nanoparticles can be coated with mesoporous silica using nonionic triblock copolymer $\text{EO}_{20}\text{PO}_{70}\text{EO}_{20}$ (P 123) as structure-directing agent. The composite can load ibuprofen and release the drug in the PBS. The composite was characterized by X-ray diffraction (XRD), transmission electron microscopy (TEM), nitrogen absorption/desorption isotherms, fluorescence spectra, and UV/Vis absorption spectra, respectively. The composite particles have considerable large pore volume and large surface area. In addition, the composite still emits strong green fluorescence (Tb^{3+}) and can be used as fluorescent probes in drug delivery system.

Copyright © 2008 Deyan Kong et al. This is an open access article distributed under the Creative Commons Attribution License, which permits unrestricted use, distribution, and reproduction in any medium, provided the original work is properly cited.

1. INTRODUCTION

Currently, nanomaterials have been applied in many medical and biological fields, such as clinical diagnosis, drug delivery, fluorescent markers in vitro and in vivo [1–7], and so forth. Among these applications, drug delivery technology can bring both commercial and therapeutic values to health care products [8]. At the same time, mesoporous silica materials have been interesting in the use as controlled drug delivery matrixes to meet the need for prolonged and better controlled drug administration [9], due to their nontoxic and highly biocompatible nature, a highly regular pore structures, high specific pore volumes [9–13], and very high specific surface area with abundant Si–OH groups on the pore surface, which can react with appropriate drug functional groups and is suitable for loading and releasing drug in a more reproducible and predictable manner [14–24].

Several research groups have investigated the conventional mesoporous silica materials (such as M41S and SBA-n) used as drug delivery systems [14–21]. These systems exhibit sustained release properties [8, 17, 24, 25]. However, the use of bulk mesoporous silica materials in many applications suffers from some limitations, especially in targeted drug delivery mechanisms as the carrier and drug kinetics marker in

the pharmacological research [9]. Recently, the composites of the nanoparticles and mesoporous silica have obtained more and more interest [26–28], especially the magnetic mesoporous silica materials which have been investigated for separation and delivery systems [3, 9, 27, 28]. However, the fluorescent mesoporous silica materials, as the delivery systems, were reported rarely. If one could combine the advantages of mesoporous silica and fluorescent particles to fabricate a composite, the composite can also be potential in the fields of drug delivery, disease diagnosis, and therapy. This is because the composite material not only has high pore volume for the storage and delivery of drugs, but also possesses fluorescence properties by which can be used to track and evaluate the efficiency of the drug release. The composite may target the path of delivery, furthermore supply the information about the mechanism of drugs delivery, and can be employed for qualitative and quantitative detection of disease position and drug release efficiency. Therefore, the design of mesoporous composite materials with fluorescence property and drug storage capability plays the key role in achieving this application.

In this paper, we choose the $\text{CeF}_3:\text{Tb}^{3+}$ nanoparticles as the fluorescent labels and ibuprofen as the drug model. CeF_3 is a luminescent material with 100% activator concentration

[29, 30]. Doping Tb^{3+} in CeF_3 resulted in a strong green emission from Tb^{3+} due to an efficient energy transfer from Ce^{3+} to Tb^{3+} [31–34]. $CeF_3:Tb^{3+}$ nanoparticles have potential application as fluorescent labels for biological molecules [34]. On the other hand, ibuprofen was used as a model drug due to its good pharmacological activity and the suitable molecule size of about 1.0×0.6 nm as well, which ensures its easy diffusion into or out of the mesoporous channels of as-prepared mesoporous silica [35–37]. Furthermore, ibuprofen is a nonsteroidal drug. Herein, we report the template-assisted scheme to fabricate uniform fluorescent nanoparticles with a fluorescent core/mesoporous silica shell structure. Then its drug storage and in vitro release property are demonstrated.

2. EXPERIMENTAL SECTION

2.1. Materials

$Tb(NO_3)_3$, $Ce(NO_3)_3 \cdot 6H_2O$ (99.99%, Shanghai Yuelong New Materials Co., Ltd., Shanghai, China), NH_4F (96%, Beijing Beihua Fine Chemical products Co., Ltd., Beijing, China) were used as starting materials and diethylene glycol (DEG) (analytical reagent, A. R. Beijing Yili Fine Chemicals Co., Ltd., Beijing, China) as the solvent for the preparation of $CeF_3:Tb^{3+}$ nanoparticles, respectively. $Tb(NO_3)_3$ was prepared by dissolving Tb_4O_7 (99.99%, Shanghai Yuelong New Materials Co., Ltd.,) in dilute nitric acid.

Tetraethoxysilane (TEOS) (A. R. Beijing Beihua Fine Chemical products Co., Ltd.) and ammonia solution (25%) (NH_4OH) (A. R. Beijing Beihua Fine Chemical products Co., Ltd.) were used as the materials for thin silica layers deposition on the surfaces of $CeF_3:Tb^{3+}$ nanoparticles with isopropyl alcohol (A. R. Beijing Beihua Fine Chemical products Co., Ltd.) as the solvent. Amphiphilic triblock copolymer $EO_{20}PO_{70}EO_{20}$ (poly (ethylene oxide)-block-poly (propylene oxide)-block-poly (ethylene oxide), with trade name Pluronic 123) (Aldrich Chemical Inc., Wis, USA) was used as the template source, deionized water and hydrochloric acid (HCl) (A. R. Beijing Beihua Fine Chemical products Co., Ltd.) as solvent and ethanol (A. R. Beijing Beihua Fine Chemical products Co., Ltd.) as the solvent for extracting the surfactant P123.

Ibuprofen (IBU) (Nanjing Chemical Reagent Co., Ltd., Nanjing, China) was used as model drug and phosphate buffer solution (PBS, pH = 7.4) consisting of 8.00 g dm^{-3} NaCl, 0.20 g dm^{-3} KCl, 1.44 g dm^{-3} Na_2HPO_4 , and 0.24 g dm^{-3} KH_2PO_4 as solvent.

2.2. Synthesis of $CeF_3:Tb^{3+}$ nanoparticles

The doping concentration of Tb^{3+} in CeF_3 host was 15 mol% of Ce^{3+} in CeF_3 host, which had been optimized previously [34]. Typically, 18 mmol NH_4F was dissolved in 50 mL DEG in an oil bath at $70^\circ C$ to form a clear solution. At the same time, 50 mL DEG containing 5.1 mmol of $Ce(NO_3)_3 \cdot 6H_2O$ and 0.9 mmol of $Tb(NO_3)_3$ in 250 mL round-bottomed flask was stirred and heated until $100^\circ C$ in the oil bath in an Ar atmosphere. When $Ce(NO_3)_3 \cdot 6H_2O$ and $Tb(NO_3)_3$ were dis-

solved completely, the temperature was increased to $200^\circ C$. Then, the solution of NH_4F was injected into it and the mixture was kept stirring for 1 hour at $200^\circ C$. The obtained suspension was cooled to room temperature and diluted with 100 mL ethanol. The $CeF_3:Tb^{3+}$ nanoparticles were obtained by centrifugation at a speed of 4500 rpm. Then they were re-dispersed in ethanol and centrifuged several times to remove any extraneous material. Finally, the obtained $CeF_3:Tb^{3+}$ nanoparticles were dried at $70^\circ C$ in air.

2.3. Thin layers silica deposition on $CeF_3:Tb^{3+}$ nanoparticles

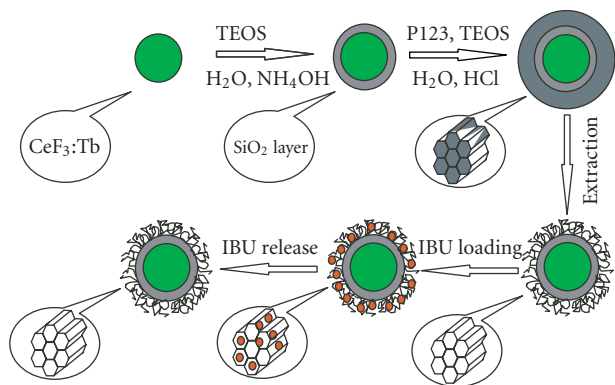
In a typical procedure [38–40], 0.1715 g $CeF_3:Tb^{3+}$ nanoparticles were added into 200 mL isopropyl alcohol solution containing 0.45 mol dm^{-3} of NH_4OH and 3.05 mol dm^{-3} of H_2O , then the suspension was stirred $40^\circ C$ for 30 minutes. Then, 0.8 mmol TEOS was added into the suspension and the mixture was stirred for 2 hours at $40^\circ C$. The product was obtained by the procedure of centrifugation and dispersion the same as the above part. In this way, silica coating $CeF_3:Tb^{3+}$ nanoparticles were obtained.

2.4. Synthesis of mesoporous silica encapsulation $CeF_3:Tb^{3+}$ nanoparticles

In a typical synthesis [12], 1 g P123 was completely dissolved in 7.5 mL H_2O and 29 mL of 2.0 M HCl solution, then 0.7550 g $CeF_3:Tb^{3+}$ nanoparticles with thin layers of silica were added and stirred at room temperature for 1 hour. The suspension was stirred at $40^\circ C$ for 30 minutes. Then 1.2 mL TEOS was added into the suspension and the mixture was stirred for 15 minutes and then aged for 30 minutes at $40^\circ C$. The solid sample was washed and separated by centrifugation-dispersion cycles with ethanol, then dried for 3 hours at $100^\circ C$ in air. Finally, the surfactant was removed by stirring the as-synthesized product in 100 mL ethanol and 2 g of dilute HCl solution at $80^\circ C$ for 10 hours. After this treatment, the product was recovered by filtration, and washed with water and ethanol, and finally dried at $70^\circ C$ in air.

2.5. Drug loading procedure and in vitro release study

To load IBU into mesoporous silica coating $CeF_3:Tb^{3+}$ nanoparticles, 0.1585 g of the composite powder sample was added to 10 mL of ibuprofen ethanol solution (2.3 mg/mL) and soaked for 3 days under stirring. Then the powders were separated and thoroughly washed with ethanol, dried at $70^\circ C$ in air. Filtrate was collected and properly diluted to determine the drug-loading amount by spectrophotometer. In order to evaluate the release profile of the material, the drug-loaded samples were compressed into tablet form (9 mm \times 0.5 mm) by pressure (4 MPa). 0.0952 g of the tablet was soaked in 25 mL preheated PBS under mild stirring and the temperature was kept at $37 \pm 1^\circ C$. Samples of 4 mL were withdrawn at a predetermined time, replaced by fresh preheated PBS, and spectrophotometrically analyzed for IBU at 222 nm. Calibration curve of IBU was determined by



SCHEME 1: The diagram shows the whole formation processes for the mesoporous silica coating $\text{CeF}_3:\text{Tb}^{3+}$ nanoparticles and IBU loading and release processes.

taking absorbance versus IBU concentration between 0 and $22.4 \mu\text{g}/\text{mL}$ as parameters.

The whole formation processes for the mesoporous silica coating $\text{CeF}_3:\text{Tb}^{3+}$ nanoparticles and the subsequent IBU loading and release processes are shown in Scheme 1.

2.6. Characterization

X-ray diffraction (XRD) was carried out on a Rigaku-Dmax 2500 diffractometer with $\text{Cu K}\alpha$ radiation ($\lambda = 0.15405 \text{ nm}$). The accelerating voltage and emission current were 40 kV and 200 mA, respectively. TEM images were obtained using a JEOL 2010 transmission electron microscope operating at 200 kV. Samples for TEM were prepared by depositing a drop of ethanol suspension of the powder sample onto a copper grid and dried in air. The excitation and emission spectra were taken on an F-4500 spectrophotometer equipped with a 150 W xenon lamp as the excitation source. The UV/Vis absorption spectra were measured on a TU-1901 spectrophotometer. All the measurements were performed at room temperature. Nitrogen adsorption and desorption isotherms were carried out on a Nova 1000 analyzer at 77 K under a continuous adsorption condition, and the samples were degassed at 100°C overnight before measurement. Brunauer-Emmett-Teller (BET) and Barrett-Joyner-Halenda (BJH) analyses were used to determine the surface area, pore size, and pore volume.

3. RESULTS AND DISCUSSION

3.1. Structure and morphological properties of the mesoporous silica coating $\text{CeF}_3:\text{Tb}^{3+}$ nanocrystals

XRD, TEM, and nitrogen adsorption/desorption isotherms were employed to characterize the structure and morphological properties of the mesoporous silica coating $\text{CeF}_3:\text{Tb}^{3+}$ nanocrystals. Figure 1 shows XRD patterns of the core material of mesoporous silica coating $\text{CeF}_3:\text{Tb}^{3+}$ sample with the standard data for bulk CeF_3 as a reference and (a) the low-angle portion in the shell material (b). The results of XRD

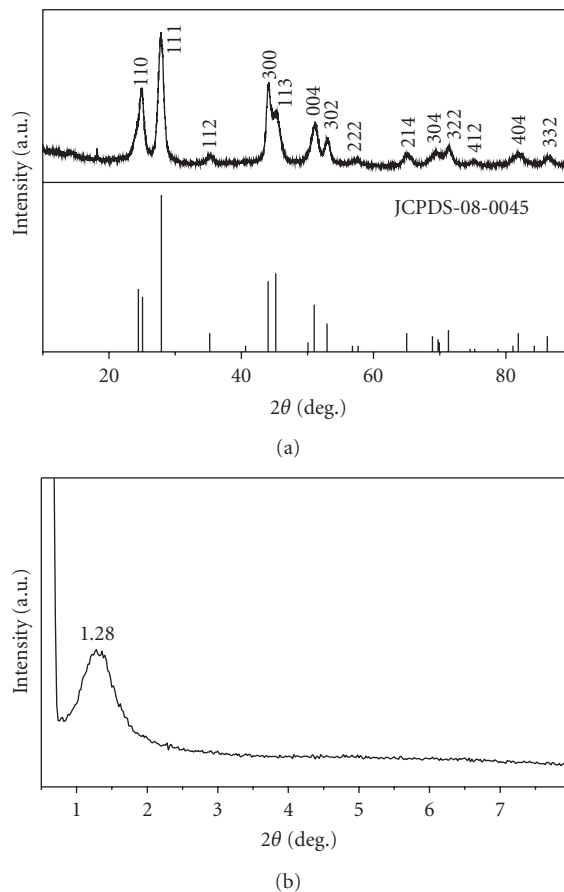


FIGURE 1: XRD patterns of the mesoporous silica coating $\text{CeF}_3:\text{Tb}^{3+}$ sample with the core material with the standard data for bulk CeF_3 as a reference (a) and the low-angle portion in the shell material (b).

(in Figure 1(a)) indicate that the core material is crystallized well and all the peaks are in good agreement with hexagonal phase structure known from bulk CeF_3 phase (JCPDS card no. 08-0045). The diffraction peaks for $\text{CeF}_3:\text{Tb}^{3+}$ core material are broadened due to the smaller crystallite size. The low-angle XRD pattern of the composite (in Figure 1(b)) shows a unique intense maximum at $2\theta = 1.28^\circ$. This pattern indicates that mesoscopic order is preserved in the outer layer of silica.

Figure 2 shows the TEM micrographs of the mesoporous silica coating $\text{CeF}_3:\text{Tb}^{3+}$ sample (a) with high-resolution micrographs of the outer layer (b) and the core part (c). TEM micrograph in Figure 2(a) shows that the composite sample was aggregated to some extent and the size of the composite particles is between 50 nm and 100 nm. The size is very suitable to drug delivery, because a particle size range between 50 and 300 nm is strictly demanded for drug delivery, and above 300 nm, a significant proportion of particles will be trapped in the lungs and liver, while too small particles will not carry large quantity of drug. TEM micrograph in Figure 2(b) shows that the mesoporous silica possesses ordered hexagonal pore systems, which confirmed the result of the low-angle part of XRD and was further confirmed by the nitrogen

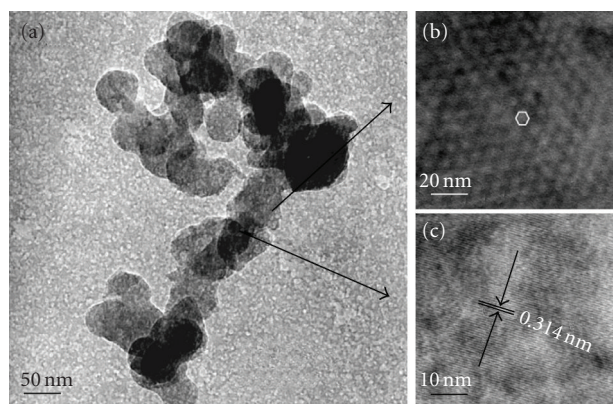


FIGURE 2: TEM micrographs of the mesoporous silica coating $\text{CeF}_3:\text{Tb}^{3+}$ sample (a) with high-resolution micrographs of the outer layer (b) and the core part (c).

adsorption/desorption isotherms. The high-resolution TEM micrograph of the core material (Figure 2(c)) clearly displays the resolved lattice fringes with a constant spacing of 0.314 nm ascribed to the (111) plane of CeF_3 , which is indicative of the high crystallinity of these $\text{CeF}_3:\text{Tb}^{3+}$ nanoparticles. The purpose of this thin dense silica layer is to protect the fluorescent core from leaching into the mother system and the resultant silica surface also facilitates the assembly of structure-directing agent (P 123).

The nitrogen adsorption/desorption isotherms of mesoporous silica coating $\text{CeF}_3:\text{Tb}^{3+}$ particles in Figure 3(a) indicate a linear increase in the amount of adsorbed nitrogen at a low relative pressure ($P/P_0 = 0.45$). According to the IUPAC, it can be classified as a type of H2 hysteresis. The steep increase in nitrogen at relative pressures in the range between $P/P_0 = 0.45$ and 0.85 reflects a type of IV isotherm characteristic of mesoporous materials. A large hysteresis between the adsorption and desorption branches, which is characteristic of highly porous materials, confirms the formation of mesopores on the fluorescent particles. From the inset curve (a), the porous silica shell of the composite consists of two kinds of pores, a part of micropores and the other part of mesopores. Calculated from the nitrogen isotherm with the BJH method, an average pore diameter is determined to be 5.9 nm. The BET surface area and the BJH pore volume are $428 \text{ m}^2/\text{g}$ and $0.63 \text{ cm}^3/\text{g}$, respectively, which is considerably large since all the cores have been included in the calculations. Compared with that in Figure 3(a), the isotherms of IBU-loading composite (in Figure 3(b)) have changed, so do the pore distribution in the inset curve (b). From these results, we can draw a conclusion that the drug was successfully loaded into the pores of the composite.

3.2. Photoluminescent properties

Figure 4 gives the excitation (a) and emission spectra (b) of the mesoporous silica coating $\text{CeF}_3:\text{Tb}^{3+}$ particles and the inserted photograph of the IBU-loading composite in the release process under irradiation of a 254 nm UV lamp. Monitored with the 543 nm emission ($^5\text{D}_4\text{-}^7\text{F}_5$) of Tb^{3+} , the ex-

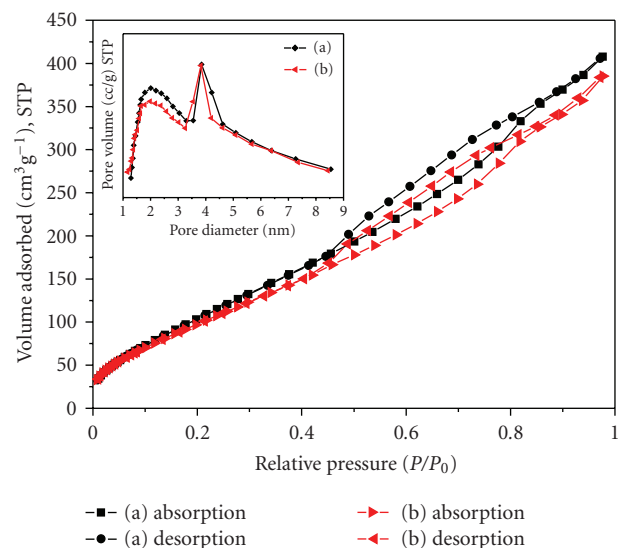


FIGURE 3: The nitrogen adsorption/desorption isotherms of the mesoporous silica coating $\text{CeF}_3:\text{Tb}^{3+}$ particles and IBU-loading composite and their pore size distributions in the inset pattern.

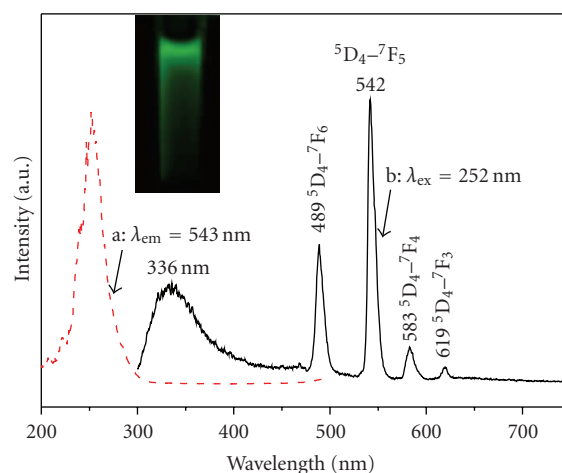


FIGURE 4: The excitation (a) and emission spectra (b) of the mesoporous silica coating $\text{CeF}_3:\text{Tb}^{3+}$ particles and the inserted photograph of the IBU-loading composite in the release process under irradiation of a 254 nm UV lamp.

citation spectrum (in Figure 4(a)) consists of a broad and strong band with a maximum of 252 nm, which corresponds to the transitions from the ground state $^2\text{F}_{5/2}$ of Ce^{3+} to the excited Ce^{3+} 5d states [41]. Under the excitation of 252 nm UV lamp, the emission spectrum (in Figure 4b) consists of two parts: the broad band emission in the region of 300–450 nm (peaking at 336 nm) and the sharp peaks between 450 and 650 nm (peaking at 489, 543, 584, 618 nm). The former is due to 5d–4f transition of Ce^{3+} ion, and the latter due to $^5\text{D}_4\text{-}^7\text{F}_j$ ($J = 6, 5, 4, 3$) transitions of Tb^{3+} ion with $^5\text{D}_4\text{-}^7\text{F}_5$ (543 nm) being the most prominent group, respectively [34]. In the inserted photograph, the IBU-loading composite

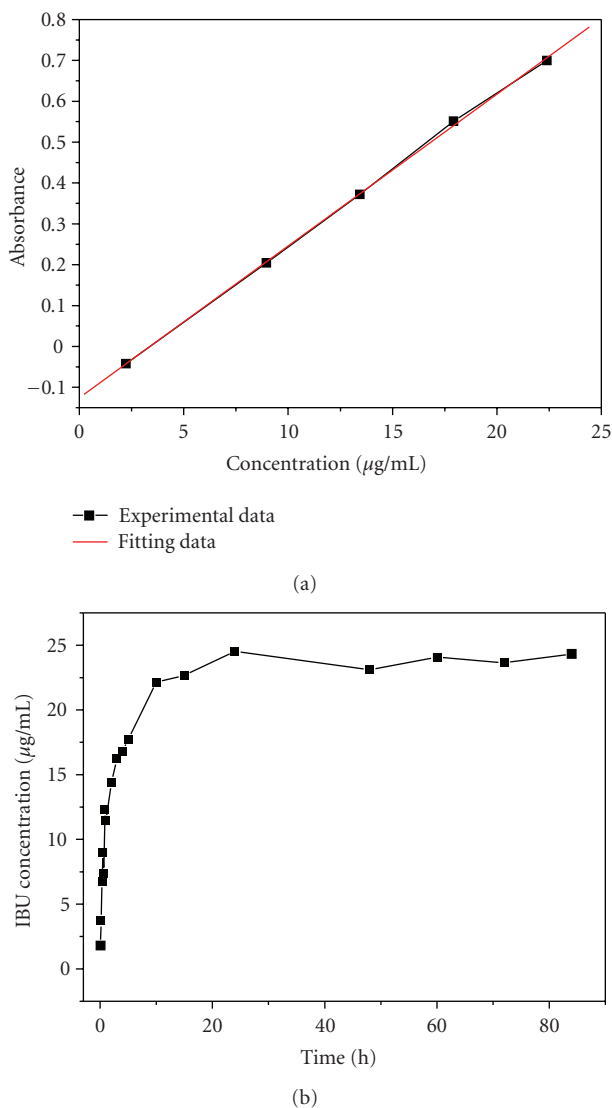


FIGURE 5: The calibration curve of IBU (a) and the release kinetics result of IBU as a function of time from the mesoporous silica coating $\text{CeF}_3:\text{Tb}^{3+}$ particles (b).

in the release process shows strong green emission under the irradiation of a 254 nm UV lamp. The photograph indicates that the mesoporous silica coating $\text{CeF}_3:\text{Tb}^{3+}$ nanoparticles can be used as a fluorescent label in the drug system.

3.3. In vitro IBU release

Figure 5 shows the calibration curve of IBU (a) and the release kinetics result of IBU as a function of time from the mesoporous silica coating $\text{CeF}_3:\text{Tb}^{3+}$ nanoparticles (b). The calibration curve (in Figure 5(a)) fits the Lambert and Beers law

$$A = 0.03715 \times C - 0.12562, \quad (1)$$

where A is the absorbance and C is the concentration ($\mu\text{g/mL}$).

During the drug release study in vitro, calculation of the corrected concentration of released IBU is based on the following equation [21]:

$$C_{\text{tcorr}} = C_t + \frac{v}{V \sum_0^{t-1} C_t}, \quad (2)$$

where C_{tcorr} is the corrected concentration at time t , C_t is the apparent concentration at time t , v is the volume of sample taken and V is the total volume of dissolution medium. Small and large molecular drugs can be entrapped within the mesopores by an impregnation process and liberated via diffusion-controlled mechanism [8]. The silanol groups presented at the mesopores surface were selected as reaction sites to form hydrogen bonding with the carboxyl group of IBU, when IBU was impregnated into the pore channels. In the release process, the solvent entered the drug-matrix phase through pores. The drug was dissolved slowly into the fluid phase and diffused from the system along the solvent-filled capillary channels. The result (in Figure 5(b)) shows that the burst release of 50% of drug is in 2 hours followed by the slow release and 100% complete release reached in 24 hours. The initial burst release may be due to the excessive drugs which were weakly entrapped inside the mesopores or located at the outer surface of mesoporous silica coating nanoparticles, and the slow release of the rest of IBU is attributed to the strong interaction between IBU molecules and the mesopore surface.

4. CONCLUSIONS

In conclusion, the $\text{CeF}_3:\text{Tb}^{3+}$ nanoparticles have been successfully coating by mesoporous silica using P123 as structure-directing agent. The mesoporous silica shell possesses a part of ordered hexagonal mesoporous system and a part of microporous structure. The composite retains the green fluorescent properties and possesses considerable large pore volume and large surface area. Ibuprofen can be loaded into the channels of the composite and the drug incorporated can be released in 24 hours. Therefore, this composite can be potentially used as fluorescent probes in the targeted drug delivery system.

ACKNOWLEDGMENTS

This project is financially supported by the Foundation of "Bairen Jihua" of Chinese Academy of Sciences, the MOST of China (2003CB314707, 2007CB935502), and the National Natural Science Foundation of China (50572103, 20431030, 00610227, 50702057).

REFERENCES

- [1] D. R. Larson, W. R. Zipfel, R. M. Williams, et al., "Water-soluble quantum dots for multiphoton fluorescence imaging in vivo," *Science*, vol. 300, no. 5624, pp. 1434–1436, 2003.
- [2] Y.-S. Lin, C.-P. Tsai, H.-Y. Huang, et al., "Well-ordered mesoporous silica nanoparticles as cell makers," *Chemistry of Materials*, vol. 17, no. 18, pp. 4570–4573, 2005.

- [3] T. Sen, A. Sebastianelli, and I. J. Bruce, "Mesoporous silica-magnetite nanocomposite: fabrication and applications in magnetic bioseparations," *Journal of the American Chemical Society*, vol. 128, no. 22, pp. 7130–7131, 2006.
- [4] F. van de Rijke, H. Zijlmans, S. Li, et al., "Up-converting phosphor reporters for nucleic acid microarrays," *Nature Biotechnology*, vol. 19, no. 3, pp. 273–276, 2001.
- [5] A. Doat, M. Fanjul, F. Pellé, E. Hollande, and A. Lebugle, "Europium-doped bioapatite: a new photostable biological probe, internalizable by human cells," *Biomaterials*, vol. 24, no. 19, pp. 3365–3371, 2003.
- [6] E. Schröck, E. du Manoir, T. Veldman, et al., "Multicolor spectral karyotyping of human chromosomes," *Science*, vol. 273, no. 5274, pp. 494–497, 1996.
- [7] L. M. Ying, A. Bruckbauer, A. M. Rothery, Y. E. Korchev, and D. Klenerman, "Programmable delivery of DNA through a nanopipet," *Analytical Chemistry*, vol. 74, no. 6, pp. 1380–1385, 2002.
- [8] S.-W. Song, K. Hidajat, and S. Kawi, "Functionalized SBA-15 surfaces as carriers for controlled drug delivery: influence of surface properties on matrix-drug interactions," *Langmuir*, vol. 21, no. 21, pp. 9568–9575, 2005.
- [9] W. R. Zhao, J. L. Gu, L. X. Zhang, H. R. Chen, and J. L. Shi, "Fabrication of uniform magnetic nanocomposite spheres with a magnetic core/mesoporous silica shell structure," *Journal of American Chemical Society*, vol. 127, no. 25, pp. 8916–8917, 2005.
- [10] M. Arruebo, M. Galán, N. Navascués, et al., "Development of magnetic nanostructured silica-based materials as potential vectors for drug-delivery applications," *Chemistry of Materials*, vol. 18, no. 7, pp. 1911–1919, 2006.
- [11] C. T. Kresge, M. E. Leonowicz, W. J. Roth, J. C. Vartuli, and J. S. Beck, "Ordered mesoporous molecular-sieves synthesized by a liquid-crystal template mechanism," *Nature*, vol. 359, no. 6397, pp. 710–712, 1992.
- [12] D. Y. Zhao, J. L. Feng, Q. S. Huo, et al., "Triblock copolymer syntheses of mesoporous silica with periodic 50 to 300 angstrom pores," *Science*, vol. 279, no. 5350, pp. 548–552, 1998.
- [13] M. Hartmann, "Ordered mesoporous materials for bioadsorption and biocatalysis," *Chemistry of Materials*, vol. 17, no. 18, pp. 4577–4593, 2005.
- [14] M. Vallet-Regí, A. Rámila, R. P. del Real, and J. Pérez-Pariente, "A new property of MCM-41: drug delivery system," *Chemistry of Materials*, vol. 13, no. 2, pp. 308–311, 2001.
- [15] A. Rámila, R. P. del Real, R. Marcos, P. Horcajada, and M. Vallet-Regí, "Drug release and in vitro assays of bioactive polymer/glass mixtures," *Journal of Sol-Gel Science and Technology*, vol. 26, no. 1–3, pp. 1195–1198, 2003.
- [16] B. Muñoz, A. Rámila, J. Pérez-Pariente, I. Díaz, and M. Vallet-Regí, "MCM-41 organic modification as drug delivery rate regulator," *Chemistry of Materials*, vol. 15, no. 2, pp. 500–503, 2003.
- [17] P. Horcajada, A. Rámila, J. Pérez-Pariente, and M. Vallet-Regí, "Influence of pore size of MCM-41 matrices on drug delivery rate," *Microporous and Mesoporous Materials*, vol. 68, no. 1–3, pp. 105–109, 2004.
- [18] A. L. Doadrio, E. M. B. Sousa, J. C. Doadrio, J. Pérez-Pariente, I. Izquierdo-Barba, and M. Vallet-Regí, "Mesoporous SBA-15 HPLC evaluation for controlled gentamicin drug delivery," *Journal of Controlled Release*, vol. 97, no. 1, pp. 125–132, 2004.
- [19] C. Tourné-Péteuil, D. A. Lerner, C. Charnay, L. Nicole, S. Bégu, and J. M. Devoisselle, "The potential of ordered mesoporous silica for the storage of drugs: the example of a pentapeptide encapsulated in a MSU-tween 80," *ChemPhysChem*, vol. 4, no. 3, pp. 281–286, 2003.
- [20] K. A. Fisher, K. D. Huddersman, and M. J. Taylor, "Comparison of micro- and mesoporous inorganic materials in the uptake and release of the drug model fluorescein and its analogues," *Chemistry—A European*, vol. 9, no. 23, pp. 5873–5878, 2003.
- [21] H. Hata, S. Saeki, T. Kimura, Y. Sugahara, and K. Kuroda, "Adsorption of taxol into ordered mesoporous silicas with various pore diameters," *Chemistry of Materials*, vol. 11, no. 4, pp. 1110–1119, 1999.
- [22] C.-Y. Lai, B. G. Trewyn, D. M. Jeftinija, et al., "A mesoporous silica nanosphere-based carrier system with chemically removable CdS nanoparticles caps for stimuli-responsive controlled release of neurotransmitters and drug molecules," *Journal of American Chemical Society*, vol. 125, no. 15, pp. 4451–4459, 2003.
- [23] N. K. Mal, M. Fujiwara, and Y. Tanaka, "Photocontrolled reversible release of guest molecules from coumarin-modified mesoporous silica," *Nature*, vol. 421, no. 9621, pp. 350–353, 2003.
- [24] Y. F. Zhu, J. L. Shi, W. H. Shen, et al., "Stimuli-responsive controlled drug release from a hollow mesoporous silica sphere/polyelectrolyte multilayer core-shell structure," *Angewandte Chemie International Edition*, vol. 44, no. 32, pp. 5083–5087, 2005.
- [25] J. Andersson, J. Rosenholm, S. Areva, and M. Lindén, "Influences of material characteristic on ibuprofen drug loading and release profiles from ordered micro- and mesoporous silica matrices," *Chemistry of Materials*, vol. 16, no. 21, pp. 4160–4167, 2004.
- [26] L. Babes, B. Denizot, G. Tanguy, J. J. Le Jeune, and P. J. Jallet, "Synthesis of iron oxide nanoparticles used as MRI contrast agents: a parametric study," *Journal of Colloid Interface Science*, vol. 212, no. 2, pp. 474–482, 1999.
- [27] P. Wu, J. Zhu, and Z. Xu, "Template-assisted synthesis of mesoporous magnetic nanocomposite particles," *Advanced Functional Materials*, vol. 14, no. 4, pp. 345–351, 2004.
- [28] A.-H. Lu, W.-C. Li, A. Kiefer, et al., "Fabrication of magnetically separable mesostructured silica with an open pore system," *Journal of the American Chemical Society*, vol. 126, no. 28, pp. 8616–8617, 2004.
- [29] A. J. Wojtowicz, M. Balcerzyk, E. Berman, and B. Lempicki, "Optical spectroscopy and scintillation mechanisms of $Ce_xLa_{1-x}F_3$," *Physical Review B*, vol. 49, no. 21, pp. 14880–14895, 1994.
- [30] K. Wei, C. Guo, J. Deng, and C. Shi, "Electronic structure of CeF_3 crystal," *Journal of Electron Spectroscopy and Related Phenomena*, vol. 79, pp. 83–85, 1996.
- [31] J. W. Stouwdam and F. C. J. M. Van Veggel, "Improvement in the luminescence properties and processability of LaF_3/Ln and $LaPO_4/Ln$ nanoparticles by surface modification," *Langmuir*, vol. 20, no. 26, pp. 11763–11771, 2004.
- [32] K. Riwozki, H. Meyssamy, H. Schnablegger, A. Kornowski, and M. Haase, "Liquid-phase synthesis of colloids and redispersible powders of strongly luminescing $LaPO_4 : Ce, Tb$ nanocrystals," *Angewandte Chemie International Edition*, vol. 40, no. 3, pp. 573–576, 2001.
- [33] K. Riwozki, H. Meyssamy, A. Kornowski, and M. Haase, "Liquid-phase synthesis of doped nanoparticles: colloids of luminescing $LaPO_4 : Eu$ and $CePO_4 : Tb$ particles with a narrow particle size distribution," *Journal of Physical Chemistry B*, vol. 104, no. 13, pp. 2824–2828, 2000.

- [34] Z. L. Wang, Z. W. Quan, P. Y. Jia, et al., "A Facile synthesis and photoluminescent properties of redispersible CeF_3 , $\text{CeF}_3:\text{Tb}^{3+}$, and $\text{CeF}_3:\text{Tb}^{3+}/\text{LaF}_3$ (core/shell) nanoparticles," *Chemistry of Materials*, vol. 18, no. 8, pp. 2030–2037, 2006.
- [35] I. Izquierdo-Barba, Á. Martínez, A. L. Doadrio, J. Pérez-Pariante, and M. Vallet-Regí, "Release evaluation of drugs from ordered three-dimensional silica structures," *European Journal of Pharmaceutical Sciences*, vol. 26, no. 5, pp. 365–373, 2005.
- [36] C. Charnay, S. Bégu, C. Tourné-Péteilh, L. Nicole, D. A. Lerner, and J. M. Devoisselle, "Inclusion of ibuprofen in mesoporous templated silica: drug loading and release property," *European Journal of Pharmaceutics and Biopharmaceutics*, vol. 57, no. 3, pp. 533–540, 2004.
- [37] Y.-F. Zhu, J.-L. Shi, Y.-S. Li, H.-R. Chen, W.-H. Shen, and X.-P. Dong, "Storage and release of ibuprofen drug molecules in hollow mesoporous silica spheres with modified pore surface," *Microporous and Mesoporous Materials*, vol. 85, no. 1-2, pp. 75–81, 2005.
- [38] W. Stöber, A. Fink, and E. Bohn, "Controlled growth of monodisperse silica spheres in the micron size range," *Journal of Colloid and Interface Science*, vol. 26, no. 1, pp. 62–69, 1968.
- [39] M. Ohmori and E. Matijević, "Preparation and properties of uniform coated colloidal particles. VII. Silica on hematite," *Journal of Colloid and Interface Science*, vol. 150, no. 2, pp. 594–598, 1992.
- [40] M. Ohmori and E. Matijević, "Preparation and properties of uniform coated inorganic colloidal particles. 8. Silica on iron," *Journal of Colloid and Interface Science*, vol. 160, no. 2, pp. 288–292, 1993.
- [41] M. Yu, J. Lin, J. Fu, H. J. Zhang, and Y. C. Han, "Sol-gel synthesis and photoluminescent properties of $\text{LaPO}_4 : \text{A}$ ($\text{A} = \text{Eu}^{3+}, \text{Ce}^{3+}, \text{Tb}^{3+}$) nanocrystalline thin films," *Journal of Materials Chemistry*, vol. 13, no. 6, pp. 1413–1419, 2003.

Research Article

Nanostructural Organization of Naturally Occurring Composites—Part I: Silica-Collagen-Based Biocomposites

Hermann Ehrlich,¹ Sascha Heinemann,¹ Christiane Heinemann,¹ Paul Simon,²
Vasily V. Bazhenov,³ Nikolay P. Shapkin,³ René Born,¹ Konstantin R. Tabachnick,⁴
Thomas Hanke,¹ and Hartmut Worch¹

¹Max Bergmann Center of Biomaterials and Institute of Materials Science, Dresden University of Technology, 01069 Dresden, Germany

²Max Planck Institute of Chemical Physics of Solids, 01187 Dresden, Germany

³Institute of Chemistry and Applied Ecology, Far Eastern National University, 690650 Vladivostok, Russia

⁴P.P. Shirshov Institute of Oceanology, Russian Academy of Sciences, Nahimovsky pr. 36, 117997 Moscow, Russia

Correspondence should be addressed to Hermann Ehrlich, hermann.ehrlich@tu-dresden.de

Received 2 November 2007; Accepted 31 December 2007

Recommended by Donglu Shi

Glass sponges, as examples of natural biocomposites, inspire investigations aiming at both a better understanding of biomineralization mechanisms and novel developments in the synthesis of nanostructured biomimetic materials. Different representatives of marine glass sponges of the class Hexactinellida (Porifera) are remarkable because of their highly flexible basal anchoring spicules. Therefore, investigations of the biochemical compositions and the micro- and nanostructure of the spicules as examples of naturally structured biomaterials are of fundamental scientific relevance. Here we present a detailed study of the structural and biochemical properties of the basal spicules of the marine glass sponge *Monorhaphis chuni*. The results show unambiguously that in this glass sponge a fibrillar protein of collagenous nature is the template for the silica mineralization in all silica-containing structural layers of the spicule. The structural similarity and homology of collagens derived from *M. chuni* spicules to other sponge and vertebrate collagens have been confirmed by us using FTIR, amino acid analysis and mass spectrometric sequencing techniques. We suggest that nanomorphology of silica formed on proteinous structures could be determined as an example of biodirected epitaxial nanodistribution of amorphous silica phase on oriented fibrillar collagen templates. Finally, the present work includes a discussion relating to silica-collagen-based hybrid materials for practical applications as biomaterials.

Copyright © 2008 Hermann Ehrlich et al. This is an open access article distributed under the Creative Commons Attribution License, which permits unrestricted use, distribution, and reproduction in any medium, provided the original work is properly cited.

1. INTRODUCTION

Glass sponges (Hexactinellida: Porifera) provide an abundant source of unusual skeleton structures, which could be defined as natural silica-based nanostructured composite materials. They are intriguing research objects because of the hierarchical organization of their spicules from the nanoscale to the macroscale [1–3]. First observations reported by Lévi et al. [4] on silica-based spicules of a *Monorhaphis* sponge generated great interest because of their combination of properties, namely, toughness combined with stiffness, and resilience. This sponge species synthesizes the largest biosilica structures on earth [5]. Pencil-sized rod spicules, a meter or more in length, could be bent into a circle without breaking. When the load was released, the spicule recovered

its original shape. When the bending of the spicule rod was compared with that of a synthetically derived pure silica rod, the toughness of the spicule was found to be nearly an order of magnitude higher [2]. Recently, the micromechanical properties of biological silica in the giant anchor spicule of *Monorhaphis chuni* were reported on [6]. Nanoidentation showed a considerably reduced stiffness of the spicule compared to technical quartz glass with different degrees of hydration. Moreover, stiffness and hardness were shown to oscillate as a result of the laminate structure of the spicules. Raman spectroscopic imaging showed that the organic layers are protein-rich and that there is an OH-enrichment in silica near the central axial filament of the spicule. Small-angle X-ray scattering revealed the presence of nanospheres with a diameter of only 2.8 nm as the basic unit of silica.

It was suggested that biogenic silica formed by glass sponges possesses reduced stiffness but substantially higher toughness than technical glass due to its architecture, determined by structure at the nanometer and the micrometer level [6]. Unfortunately, the nature and the origin of the protein matrix were not investigated in this study.

There is no doubt that glass sponge anchoring spicules are remarkable objects because of their size, durability, high flexibility, and their exceptional fibre-optic properties, which all together render them of interest as novel biomimetic materials [7]. Of course, the materials science aspects of glass sponges can be studied by model systems, and utilized for biomimetic engineering. However, we cannot mimic nature with a view to designing novel biomaterials without knowledge of the nature and origin of the organic nanostructured matrices of corresponding natural biocomposites which are present in these sponges. Therefore, the biggest shortcoming common to all publications relating to mechanical [2], structural [3], and optical [8] properties of glassy sponge skeletal formations is a lack of real information regarding the chemical nature of corresponding organic matrices.

The finding of collagen within basal spicules of the glass sponge *Hyalonema sieboldi* [9–11], as well as the occurrence of chitin within the framework skeleton of the glass sponges *Farrea occa* [12], and spicules of *Euplectella aspergillum* [7] as revealed by gentle desilicification in alkali, stimulated further attempts to search for materials of organic nature in skeletal structures of these unique deep-sea organisms. Consequently, the objective of the current study was to test our hypothesis that collagen is also an essential component of the giant anchoring silica spicules of *Monorhaphis chuni*, and if so, to unravel its involvement in the mechanical behavior of these formations, which was well investigated recently [6].

In the present work, we provide a detailed study confirming our hypothesis that the nanofibrillar organic matrix of collagenous nature within the giant spicules of *M. chuni* is responsible for their extraordinary mechanical properties. We performed structural, spectroscopic, and biochemical analyses of these glassy composites. Finally, this work includes a discussion relating to practical applications of silica-collagen composites artificially derived in vitro as biomaterials for use in biomedicine, engineering, and materials science.

2. EXPERIMENTAL

2.1. Chemical etching of spicules and extraction of collagen

Monorhaphis chuni was collected by the R.V. “Vitiaz-2 (4),” voyage 17, St. 2601, 12° 31.5′–25.04′ S 48° 05.5′–08.0′ E, depth 700 m. Dried *Monorhaphis* basal spicules (length 120 cm, diameter 1.5–4.5 mm, Figure 1) were washed three times in distilled water, cut into 2–5 cm long pieces and placed in a solution containing purified *Clostridium histolyticum* collagenase (Sigma) to digest any possible collagen contamination of exogenous nature. After incubation for 24 hours at 15°C [13], the pieces of spicules were washed again three times in distilled water, dried and placed in 10 ml plastic vessels containing 5 ml of 2.5 M NaOH solution. The

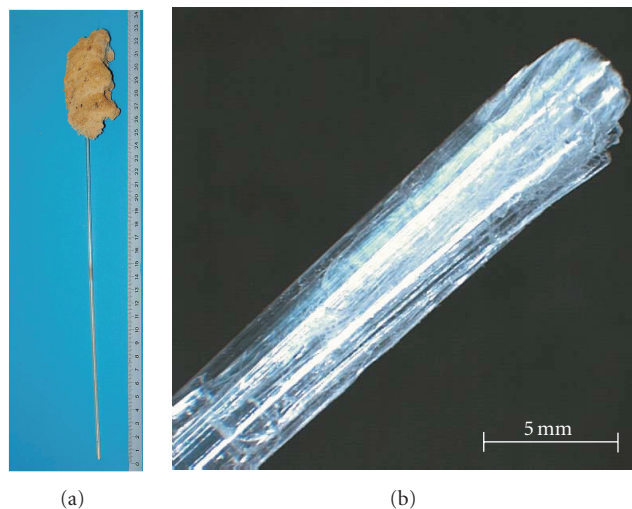


FIGURE 1: (a) Marine glass sponge *Monorhaphis chuni*, a member of the hexactinellids, (b) the sponge consists of a giant basal spicule which anchors *Monorhaphis* to the sandy substratum.

vessel was covered, placed under thermostatic conditions at 37°C and shaken slowly for 14 days. The effectiveness of the slow alkali etching was monitored using scanning electron microscopy (SEM) at different locations along the spicules' length and within the cross-sectional area.

2.2. Biochemical analysis of collagen

Alkali extracts of *Monorhaphis* spicules containing fibrillar protein were dialyzed against deionized water on Roth (Germany) membranes with a cut-off of 14 kDa. Dialysis was performed for 48 hours at 4°C. The dialyzed material was dried under vacuum conditions in a CHRIST lyophilizer (Germany). The approximate molecular weights of proteins in the lyophilizate were determined by gel electrophoresis in the presence of sodium dodecyl sulphate in 10% and 12% gel plates. The kit of molecular weight markers (Silver stain SDS molecular standard mixtures) from Sigma, USA, was used. Lyophilizates were dissolved in sample buffer (1 M Tris-HCl, pH 6.8, 2.5% SDS, 10% glycerine, 0.0125% bromphenol blue) incubated at 95°C for 5 minutes and then applied to 10% or 12% of SDS-polyacrylamide gels. After electrophoresis at 75 V for 1.5 hours, 10% gels were stained with GelCode SilverSNAP Stain Kit II (Pierce, USA), and 12% gels were stained with coomassie brilliant blue R250 to allow proteins to be visualized. To elucidate the nature of proteins isolated from glass sponge spicules, corresponding electrophoretic gels stained with Coomassie were used for the determination of the amino acid sequence by the mass spectrometric sequencing technique (MALDI, Finnigan LTQ) as described earlier [14].

2.3. Structural analysis of spicule layers

Structural analysis of the glass sponge basal spicules and corresponding extracted proteinaceous components was performed using scanning electron microscopy (SEM)

(ESEM XL 30, Philips) and transmission electron microscopy (TEM) (Zeiss EM 912). Additional transmission electron microscopy experiments were carried out at the Special Triebenberg Laboratory for electron holography and high-resolution microscopy of the Technical University Dresden. A field-emission microscope of the FEI company (Endhoven, NL) CM200 FEG/ST-Lorentz was used equipped with a 1×1 k CCD camera (multiscan, Gatan, USA). The analysis of the TEM images was realized by means of the Digital Micrograph software (Gatan, USA). Infrared spectra were recorded with a Perkin Elmer FTIR Spectrometer Spectrum 2000, equipped with an AutoImage Microscope using the fourier transform infrared reflection absorption spectroscopy (FT-IRRAS) technique. In the case of the FTIR-analyses, calf skin collagen (Fluka) and *Chondrosia reniformis* sponge collagen (Klinipharma GmbH, Germany) were investigated as reference samples.

2.4. Silicification of collagen in vitro

Tetramethoxysilan (TMOS 98%, ABCR GmbH, Germany) was chosen as a silica precursor and was hydrolysed for 24 h at 4°C by adding water as well as HCl as a catalyst. This procedure results in the soluble form of silica—orthosilicic acid—whose further polycondensation reactions can be divided into monomer polymerisation, nuclei growth, and aggregation of particles. Hybridization—the combination of silica and collagen—was performed by intensive mixing of prehydrolysed TMOS and the homogeneous collagen suspensions under ambient conditions as described in [15].

2.5. Biocompatibility of the silica-collagen hybrid materials

was evaluated by cultivating human mesenchymal stem cells on the material followed by induced differentiation into osteoblast-like cells [16].

3. RESULTS AND DISCUSSION

It was generally accepted that the skeletons of Hexactinellida are composed of amorphous hydrated silica deposited around a proteinaceous axial filament [17, 18]. The nanolocalization of the proteinaceous component of the glass sponge spicules was not investigated in detail because of lack of a demineralization method which preserved the organic matrix during desilicification. Up to now, the common technique for the desilicification of sponge spicules was based on hydrogen fluoride solutions [5], however this kind of demineralization is rather aggressive chemical procedure which could drastically change the structure of proteins [19, 20]. To overcome this obstacle, Ehrlich et al. [9–11] developed novel, slow etching methods, which use solutions of 2.5 M NaOH at 37°C and take 14 days. Using these methods, it was shown for the first time that the same class of proteins—collagen—involved in cartilage and bone formation also forms the matrix and deposition site of amorphous silica in *H. sieboldi* glass sponge spicules [9, 21]. It was suggested that the *H. sieboldi* basal spicule is an example of a biocomposite con-

taining a silicified collagen matrix and that the high collagen content is the origin of the high mechanical flexibility of the spicules.

SEM investigations of the alkali-etched *Monorhaphis chuni* spicules (Figure 2(a)) confirmed the multilayered silica structure, well-known since the first microscopically investigation of hexactinellid sponges by Schultze in 1860 [22], and present in all representatives of lyssacine Hexactinellida [18]. We focused on the investigation of fibrillar components observable at the sites of interstitial layer fractures within partially desilicified spicules. SEM investigations parallel to the slow etching procedures reveal that a fibrillar organic matrix is the template for silica mineralization. Typical fibrillar formations were observed within the tubular silica structures in all layers starting from the inner axial channel containing axial filament (Figure 3(a)) up to the outermost surface layer of the spicules as shown in Figures 2(b) and 2(c). The fibrils in each cylinder form individual concentric 2D networks with the curvature of the corresponding silicate layers. These layers of about 1 μ m in thickness are connected among each other by protein fibres (Figure 2(a)), which possess a characteristic nanofibrillar organization (Figures 2(b) and 2(d)). Partially desilicified nanofibrillar organic matrix observed on the surface of silica-based inner layers of the demineralized spicule provides strong evidence that silica nanoparticles of diameter about 35 nm are localized on the surface of corresponding nanofibrils (Figures 2(c), 2(e), and Figure 3(b)). This kind of silica nanodistribution is very similar to the silica distribution on the surface of collagen fibrils in the form of nanopearl necklets, firstly observed by us in the glass sponge *H. sieboldi* [21]. We suggest that the nanomorphology of silica on proteinous structures described here could be determined as an example of biodirected epitaxial nanodistribution [23] of the amorphous silica phase on oriented organic fibrillar templates.

The nonsilicified microfibrils of the *M. chuni* axial filament with a diameter of approximately 20–30 nm are organized in bundles with a thickness of 1–2 μ m oriented along the axis of the spicule. They can be easily identified by SEM (Figure 3(a)). The morphology of these microfibrils observed by TEM (Figures 4(a) and 4(b)) is very similar to nonstriated collagen fibrils isolated previously from *H. sieboldi* [9–11, 21] and examined using electron microscopy.

Except for collagen, there are some other possible candidates (e.g., silicateins of axial filaments such as in Demospongiae [24, 25] or as recently reported by Müller et al. [5, 26] in *M. chuni*) which would explain the nature and origin of these fibrillar formations. Therefore, a thorough biochemical analysis of isolated fibrils was performed.

The results of the amino acid analysis of protein extracts isolated from demineralized spicules showed an amino acid content typical for collagens isolated from several sources listed in Figure 4 and also reported previously [21]. The same extracts were investigated using PAG-electrophoresis. Corresponding electrophoretic gels stained with Coomassie were used for the determination of the amino acid sequence by a mass spectrometric sequencing technique as described above. We excised two main bands and digested protein material in-gel with trypsin to obtain tryptic peptide mixtures

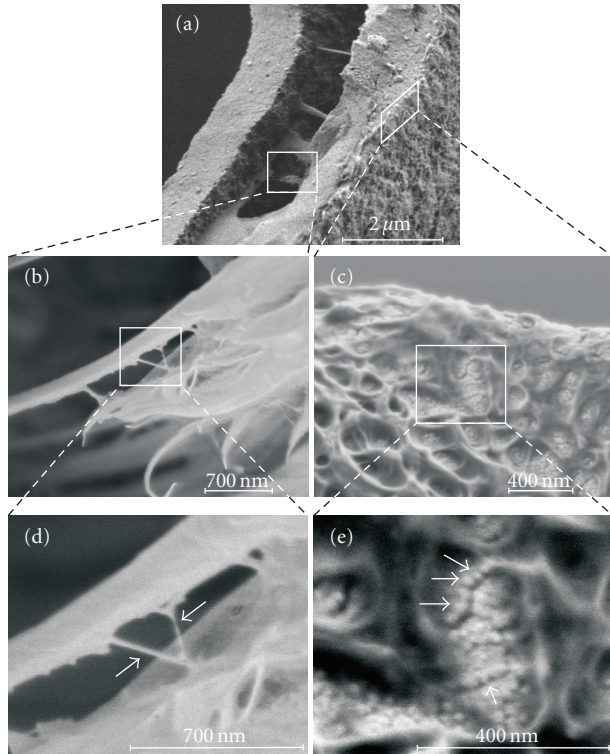


FIGURE 2: SEM images of multilayer constructed *M. chuni* spicule (a) treated with alkali solution which provides strong evidence that the multifibrillar organic matrix is the template for silica mineralization (b)–(e). Spicule layers are connected among each other by nanostructured protein fibres (arrows) (b), (d). Micrograph (e) shows a silica distribution on the surface of nanofibrils in the form of nanopearl necklets (arrows).

for further analysis using LTQ and MALDI peptide finger printings. A comparison to the MSDB protein database [27] led to the identification of collagen alpha 1 in two high MW bands. In contrast to *H. sieboldi* [9], collagen isolated and identified by the same way from *Monorhaphis sp.* was matched only to type I collagen pre-pro-alpha (I) chain (COL1A1) from dog (AAD34619) (MW 139,74). To our best knowledge, this work is the first study which confirms the presence of collagen within the spicules of *Monorhaphis* sponge and not only on their surface in the form of a collagen net which covers spicules as recently described by Müller et al. [5].

We also used highly sensitive FTIR methods for the identification of collagen isolated from spicules of *M. chuni*. Spectra obtained from this collagen, calf skin collagen type I and *C. reniformis* collagen standards were compared to each other in order to elucidate changes in protein secondary structure. The results obtained from the FTIR study (data not shown) show that collagen derived from this glass sponge exhibited spectra very similar to those from calf skin and *C. reniformis* collagens [28]. The presence of collagen fibrils in alkali solution is no surprise. Hattori et al. [29] investigated the resistance of collagen to alkali treatment at a concentration range of between 3 and 4% NaOH at 37°C in vitro. The results ob-

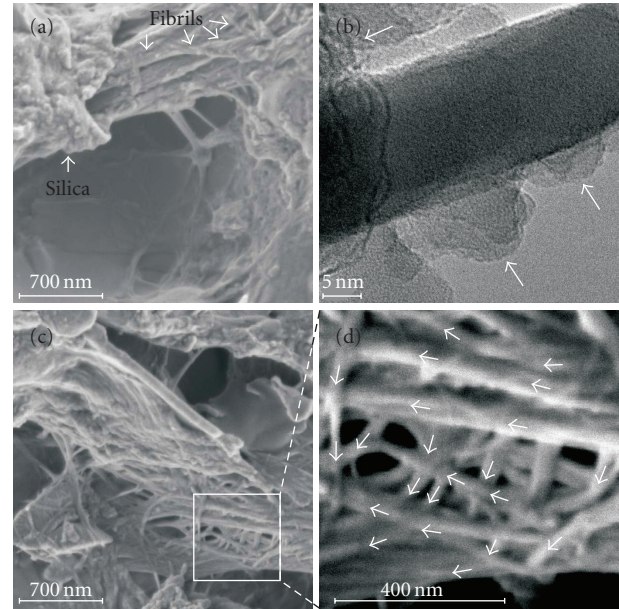


FIGURE 3: SEM and TEM nanoimagery of the fibrillar organic matrix within partially demineralized spicule. (a) Axial filament is an organization of microfibrils with a diameter of approximately 25–30 nm covered with a silica-containing layer and distributed along the axis of spicule. (b) Nanolocalization of amorphous silica particles (arrows) on the surface of partially demineralized protein fibrils using HRTEM. (c), (d) Collagen fibrils' orientation within spicule possesses a twisted plywood architecture (arrows).

tained indicated that the triple helical conformation and the helicity of the collagen molecule were maintained throughout the period of the alkaline treatment.

The procedure of alkali slow etching opens the possibility to observe the forms of collagen fibrils located within silica layers of spicules and their distribution. The results obtained by SEM observations of the desilicified spicular layers provide strong evidence that collagen fibrils' orientation within *M. chuni* spicules possesses twisted plywood architecture (Figures 3(c) and 3(d)). The twisted plywood or helicoidal structure of collagen fibrils is well-described by Giraud-Guille [30] for both in vivo and in vitro [31] systems. Spiral twisting of the collagen fibril orientation was found in several biological tissues and described for different organisms including cuticular collagens of polychaete, vestimentifera, scale collagens of primitive and bony fishes, and finally collagen fibers inside bone (all reviewed in [21]).

According to the model proposed by Giraud-Guille, adjacent lamellae have different orientations; either longitudinal (with the collagen fibers along the long axis of the lamellar sheet) or transverse (with the collagen fibers perpendicular to the long axis). From a mechanical point of view, helicoidal structures have certain advantages in resisting mechanical loads compared to orthogonal plywood structures since the twisted orientation enables a higher extensibility in tension and compression [32]. The twisted plywood architecture of collagen fibrils within basal spicules of *Monorhaphis* visible after alkali treatment (Figure 3) is very

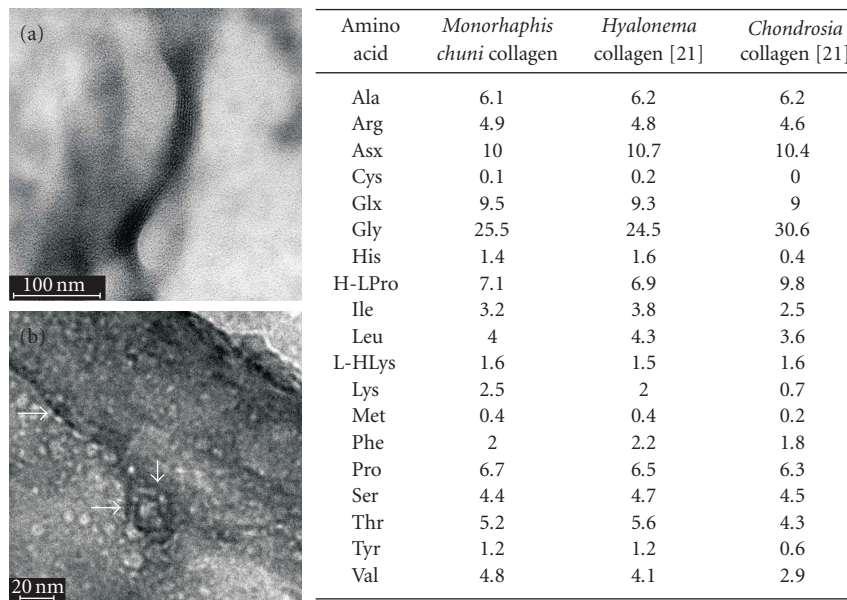


FIGURE 4: (a) High-resolution transmission electron microscopy image of the fragment of *M. chuni* collagen microfibril; (b) the arrows indicate the presence of nanofibrillar structures with a diameter which corresponds to that of collagen triple helices (1.5 nm). The results of aminoacid analysis (right) of these microfibrills showed an aminoacid content typical for collagens isolated from different sources [21].

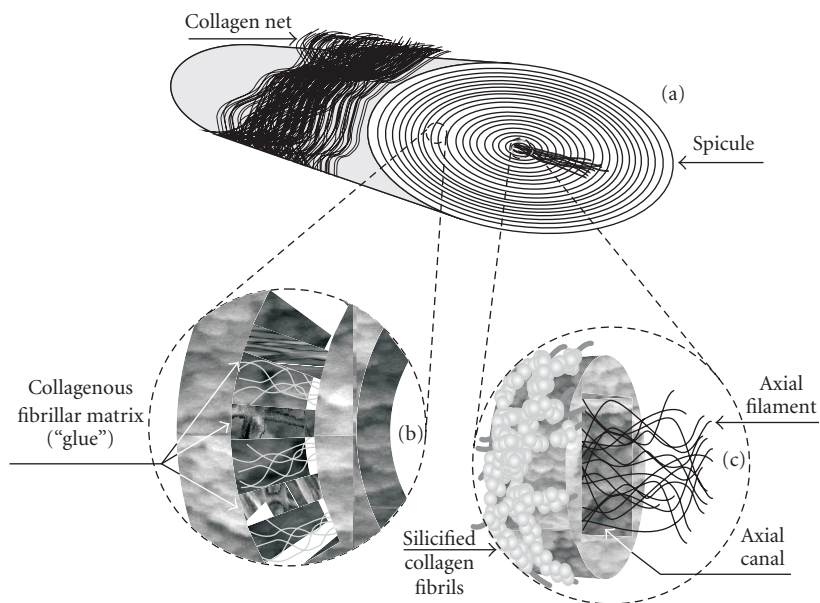


FIGURE 5: proposed model of micro- and nanostructural organisation of the basal spicule of *M. chuni* with respect to the organic matrix. (a) Collagen nets, surrounding the spicules, showed a tight mat of nanofibrils. Schematic view (b) shows a collagenous fibrillar matrix which could function as a glue between concentric layers. Image (c) represents the region of the axial canal and axial filament. The axial canal of *M. chuni* possesses a characteristic quadratic opening (c) and contains oriented bundles of unsilicified collagenous nanofibrils. The base material of the walls of the axial canal and concentric layers distributed above it consists of silicified collagen fibrils with a twisted plywood orientation. This kind of fibrillar architecture could be responsible for the remarkable micromechanical properties of the spicule as a biocomposite.

similar to that reported for lamellar bone and thus could also confirm the Girault-Guille model in the case of biosilicification in vivo. Correspondingly, this kind of collagen fibril orientation could explain why sponge spicules exhibit specific flexibility and can be bent even to a circle as reported previously [2, 4, 21]. From this point of view, basal

spicules of *Monorhaphis* sponges could be also defined as natural plywood-like silica-ceramics organized similarly to the crossed-lamellar layers of seashells [33]. Thus, we suggest that the matrix of the *M. chuni* anchoring spicule is silicified fibrillar collagen rather than collagen-containing silica which is the reason for their remarkable mechanical flexibility.

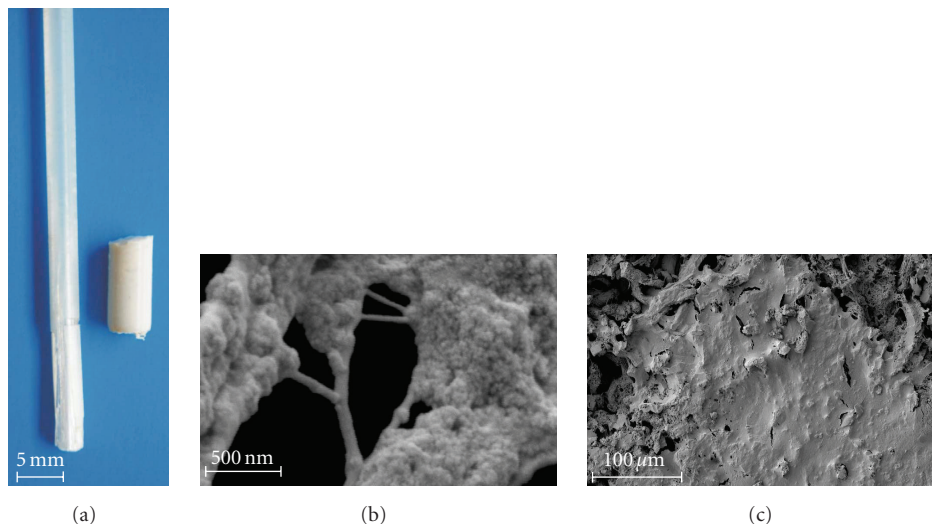


FIGURE 6: Rod-like collagen-silica-based biomaterial derived *in vitro* (a) shows morphological similarity to *M. chuni* basal spicule (a, left). SEM image (b): nanoparticles of amorphous silica deposited *in vitro* from silicic acid solution on sponge collagen fibrils replicate the nanostructure of glass sponge spicules (Figure 2(e)). SEM micrograph (c) of the surface of silica-collagen hybrid material after 14 days of cultivation of human mesenchymal stem cells, which shows high biocompatibility on this substrate.

Contrary to the postulate that silicateins, as the major biosilica-forming enzymes present in demosponges [34], are responsible for the formation of silica-based structures in all sponges, we suggested that silicateins are associated with collagen [21]. From our point of view, silicateins resemble cathepsins, which are known to be collagenolytic and capable of attacking the triple helix of fibrillar collagens. Therefore, it is not unreasonable to hypothesize that silicateins are proteins responsible for the reconstruction of collagen to form templates necessary for the subsequent silica formation. According to a dynamic model proposed by Müller and his team [5], collagen guides the silicatein(-related) protein/lectin associates concentrically along the spicules of *M. chuni*. On the basis of the results presented in this paper, we propose a model for the structure of the spicules of *Monorhaphis* sponges, including micro- and nanoaspects, which can be seen in Figure 5.

Recently, we confirmed that silicification of sponge collagen *in vitro* occurs via self-assembling, nonenzymatic mechanisms [15, 21]. To verify whether the collagenous matrix shapes the morphology of the spicules, we carried out *in vitro* experiments in which we exposed collagen to silicic acid solution ($\text{Si}(\text{OH})_4$). We obtained rod-like structures of several mm in diameter and demonstrated their similarity to the sponge spicules (Figure 6(a)). The ultrastructural analysis of these self-assembled, collagen-silica composites demonstrates that amorphous silica is deposited on the surface of collagen fibrils in the form of nanoparticle necklets (Figure 6(b)), closely resembling the nanoparticulate structure of natural *M. chuni* spicules (Figures 2(e) and 3(a)).

Bridging the nano- and microlevel, we used different techniques to create a wide spectrum of macroscopic silica-collagen-based hybrid materials. These are highly biocompatible, as demonstrated by the successful cultivation and os-

teogenic differentiation of human mesenchymal stem cells on our materials (Figure 6(c)), and potentially useful for technical and biomedical applications. On the basis of the results reported above, we also developed an advanced procedure for the biomimetically inspired production of monolithic silica-collagen hybrid xerogels [16]. The disc-like samples showed convincing homogeneity and mechanical stability, enabling cell culture experiments for the first time on such materials.

4. CONCLUSION

Recently, interest in biomaterial properties of silica-containing structures made by living sponges has grown. In order to exploit the mechanisms for the synthesis of advanced materials and devices, an investigation of the nanoscopic structure of the three-dimensional networks of these remarkable biomaterials needs to be performed [35–38]. Understanding the composition, hierarchical structure, and resulting properties of glass sponge spicules gives impetus for the development of equivalents designed *in vitro*. We showed for the first time that the silica skeletons of hexactinellids represent examples of biological materials in which a collagenous or chitinous organic matrix serves as a scaffold for the deposition of a reinforcing mineral phase in the form of silica. These findings allow us to discard different speculations about materials, which have previously been defined as organic structures (layers, filaments, surfaces) of unknown nature, and open the way for detailed studies on sponge skeletons and spicules as collagen- and/or chitin-based nanostructured biocomposites with high potential for practical applications.

ACKNOWLEDGMENTS

This work was partially supported by a joint Russian-German program “DAAD–Mikhail Lomonosov.” We thank Professor H. Lichte for the possibility to use the facilities at the Special Electron Microscopy Laboratory for high-resolution and holography at Triebenberg, TU Dresden, Germany. The authors are deeply grateful to Patrice Waridel and Andrei Shevchenko (Max Planck Institute of Molecular Cell Biology and Genetics, Dresden) for the identification of collagen in the composition of spicules, and also to Timothy Douglas, Heike Meissner, Gert Richter, Axel Mensch, and Ortrud Trommer for helpful technical assistance.

REFERENCES

- [1] J. Aizenberg, J. C. Weaver, M. S. Thanawala, V. C. Sundar, D. E. Morse, and P. Fratzl, “Skeleton of *Euplectella* sp.: structural hierarchy from the nanoscale to the macroscale,” *Science*, vol. 309, no. 5732, pp. 275–278, 2005.
- [2] G. Mayer, “Rigid biological systems as models for synthetic composites,” *Science*, vol. 310, no. 5751, pp. 1144–1147, 2005.
- [3] J. C. Weaver, J. Aizenberg, G. E. Fantner, et al., “Hierarchical assembly of the siliceous skeletal lattice of the hexactinellid sponge *Euplectella aspergillum*,” *Journal of Structural Biology*, vol. 158, no. 1, pp. 93–106, 2007.
- [4] C. Lévi, J. L. Barton, C. Guillemet, E. Le Bras, and P. Lehuède, “A remarkably strong natural glassy rod: the anchoring spicule of the *Monorhaphis* sponge,” *Journal of Materials Science Letters*, vol. 8, no. 3, pp. 337–339, 1989.
- [5] W. E. G. Müller, C. Eckert, K. Kropf, et al., “Formation of giant spicules in the deep-sea hexactinellid *Monorhaphis chuni* (Schulze 1904): electron-microscopic and biochemical studies,” *Cell and Tissue Research*, vol. 329, no. 2, pp. 363–378, 2007.
- [6] A. Woesz, J. C. Weaver, M. Kazanci, et al., “Micromechanical properties of biological silica in skeletons of deep-sea sponges,” *Journal of Materials Research*, vol. 21, no. 8, pp. 2068–2078, 2006.
- [7] H. Ehrlich and H. Worch, “Sponges as natural composites: from biomimetic potential to development of new biomaterials,” in *Porifera Research: Biodiversity, Innovation & Sustainability*, M. R. Custodio, G. Lobo-Hajdu, E. Hajdu, and G. Muricy, Eds., Museu Nacional, Rio de Janeiro, Brasil, 2007.
- [8] J. Aizenberg, V. C. Sundar, A. D. Yablon, J. C. Weaver, and G. Chen, “Biological glass fibers: correlation between optical and structural properties,” *Proceedings of the National Academy of Sciences of the United States of America*, vol. 101, no. 10, pp. 3358–3363, 2004.
- [9] H. Ehrlich, T. Hanke, P. Simon, et al., “Demineralization of natural silica based biomaterials: new strategy for the isolation of organic frameworks,” *BIOmaterialien*, vol. 6, no. 4, pp. 297–302, 2005.
- [10] H. Ehrlich, T. Hanke, H. Meissner, et al., “Nanoimagery and the biomimetic potential of marine glass sponge *Hyalonema sieboldi* (Porifera),” *VDI Berichte*, vol. 1920, pp. 163–166, 2005.
- [11] H. Ehrlich, A. V. Ereskovskii, A. L. Drozdov, et al., “A modern approach to demineralization of spicules in glass sponges (Porifera: Hexactinellida) for the purpose of extraction and examination of the protein matrix,” *Russian Journal of Marine Biology*, vol. 32, no. 3, pp. 186–193, 2006.
- [12] H. Ehrlich, M. Krautter, T. Hanke, et al., “First evidence of the presence of chitin in skeletons of marine sponges. Part II. Glass sponges (Hexactinellida: Porifera),” *Journal of Experimental Zoology Part B*, vol. 308, no. 4, pp. 473–483, 2007.
- [13] S. Kimura and M. L. Tanzer, “Nereis cuticle collagen. Isolation and properties of a large fragment resistant to proteolysis by bacterial collagenase,” *Journal of Biological Chemistry*, vol. 252, no. 22, pp. 8018–8022, 1977.
- [14] A. Shevchenko, M. Wilm, O. Vorm, and M. Mann, “Mass spectrometric sequencing of proteins from silver-stained polyacrylamide gels,” *Analytical Chemistry*, vol. 68, no. 5, pp. 850–858, 1996.
- [15] S. Heinemann, H. Ehrlich, C. Knieb, and T. Hanke, “Biomimetically inspired hybrid materials based on silicified collagen,” *International Journal of Materials Research*, vol. 98, no. 7, pp. 603–608, 2007.
- [16] S. Heinemann, C. Knieb, H. Ehrlich, et al., “A novel biomimetic hybrid material made of silicified collagen: perspectives for bone replacement,” *Advanced Engineering Materials*, vol. 9, no. 12, pp. 1061–1068, 2007.
- [17] J. C. Weaver and D. E. Morse, “Molecular biology of demosponge axial filaments and their roles in biosilicification,” *Microscopy Research and Technique*, vol. 62, no. 4, pp. 356–367, 2003.
- [18] M.-J. Uriz, X. Turon, M. A. Becerro, and G. Agell, “Siliceous spicules and skeleton frameworks in sponges: origin, diversity, ultrastructural patterns, and biological functions,” *Microscopy Research and Technique*, vol. 62, no. 4, pp. 279–299, 2003.
- [19] O. Bütschli, “Einige beobachtungen über die kiesel- und kalknadeln von spongien,” *Zeitschrift für Wissenschaftliche Zoologie*, vol. 59, no. 2, pp. 235–286, 1901.
- [20] G. Croce, A. Frache, M. Milanese, et al., “Fiber diffraction study of spicules from marine sponges,” *Microscopy Research and Technique*, vol. 62, no. 4, pp. 378–381, 2003.
- [21] H. Ehrlich and H. Worch, “Collagen, a huge matrix in glass-sponge flexible spicules of the meter-long *Hyalonema sieboldi*,” in *Handbook of Biomineralization. Vol. 1. The Biology of Biominerals Structure Formation*, E. Bäuerlein, Ed., Wiley VCH, Weinheim, Germany, 2007.
- [22] M. Schultze, *Die Hyalonemen. Ein Beitrag zur Naturgeschichte der Spongien*, Adolph Marcus, Bonn, Germany, 1860.
- [23] T. Kondo, M. Nojiri, Y. Hishikawa, E. Togawa, D. Romanovicz, and R. M. Brown Jr., “Biodirected epitaxial nanodeposition of polymers on oriented macromolecular templates,” *Proceedings of the National Academy of Sciences of the United States of America*, vol. 99, no. 22, pp. 14008–14013, 2002.
- [24] J. N. Cha, K. Shimizu, Y. Zhou, et al., “Silicatein filaments and subunits from a marine sponge direct the polymerization of silica and silicones in vitro,” *Proceedings of the National Academy of Sciences of the United States of America*, vol. 96, no. 2, pp. 361–365, 1999.
- [25] M. M. Murr and D. E. Morse, “Fractal intermediates in the self-assembly of silicatein filaments,” *Proceedings of the National Academy of Sciences of the United States of America*, vol. 102, no. 33, pp. 11657–11662, 2005.
- [26] X.-H. Wang, J.-H. Li, L. Qiao, et al., “Structure and characteristics of giant spicules of the deep sea hexactinellid sponges of the genus *Monorhaphis* (Hexactinellida: Amphidiscosida: Monorhaphididae),” *Acta Zoologica Sinica*, vol. 53, no. 3, pp. 557–569, 2007.
- [27] “Sequence Database Setup: MSDB,” Imperial College London, <http://www.matrixscience.com>.

- [28] S. Heinemann, H. Ehrlich, T. Douglas, et al., "Ultrastructural studies on the collagen of the marine sponge *Chondrosia reniformis nardo*," *Biomacromolecules*, vol. 8, no. 11, pp. 3452–3457, 2007.
- [29] S. Hattori, E. Adachi, T. Ebihara, T. Shirai, I. Someki, and S. Irie, "Alkali-treated collagen retained the triple helical conformation and the ligand activity for the cell adhesion via $\alpha 2\beta 1$ integrin," *Journal of Biochemistry*, vol. 125, no. 4, pp. 676–684, 1999.
- [30] M. M. Giraud-Guille, "Twisted plywood architecture of collagen fibrils in human compact bone osteons," *Calcified Tissue International*, vol. 42, no. 3, pp. 167–180, 1988.
- [31] M. M. Giraud-Guille, G. Mosser, C. Helary, and D. Eglin, "Bone matrix like assemblies of collagen: from liquid crystals to gels and biomimetic materials," *Micron*, vol. 36, no. 7-8, pp. 602–608, 2005.
- [32] W. Wagermaier, H. S. Gupta, A. Gourrier, et al., "Spiral twisting of fiber orientation inside bone lamellae," *Biointerphases*, vol. 1, no. 1, pp. 1–5, 2006.
- [33] B. Pokroy and E. Zolotoyabko, "Microstructure of natural plywood-like ceramics: a study by high-resolution electron microscopy and energy-variable X-ray diffraction," *Journal of Materials Chemistry*, vol. 13, no. 4, pp. 682–688, 2003.
- [34] H. C. Schröder, D. Brandt, U. Schloßmacher, et al., "Enzymatic production of biosilica glass using enzymes from sponges: basic aspects and application in nanobiotechnology (material sciences and medicine)," *Naturwissenschaften*, vol. 94, no. 5, pp. 339–359, 2007.
- [35] C. W. P. Foo, J. Huang, and D. L. Kaplan, "Lessons from seashells: silica mineralization via protein templating," *Trends in Biotechnology*, vol. 22, no. 11, pp. 577–585, 2004.
- [36] C. Sanchez, H. Arribart, and M. M. Giraud-Guille, "Biomimetism and bioinspiration as tools for the design of innovative materials and systems," *Nature Materials*, vol. 4, no. 4, pp. 277–288, 2005.
- [37] E. Pouget, E. Dujardin, A. Cavalier, et al., "Hierarchical architectures by synergy between dynamical template self-assembly and biomineralization," *Nature Materials*, vol. 6, no. 6, pp. 434–439, 2007.
- [38] P. Fratzl, "Biomimetic materials research: what can we really learn from nature's structural materials?" *Journal of the Royal Society Interface*, vol. 4, no. 15, pp. 637–642, 2007.

Research Article

On the Complexity of Electrostatic Suspension Stabilization of Functionalized Silica Nanoparticles for Biotargeting and Imaging Applications

Lotta Bergman,¹ Jessica Rosenholm,¹ Anna-Brita Öst,² Alain Duchanoy,¹ Pasi Kankaanpää,² Jyrki Heino,² and Mika Lindén¹

¹Center for Functional Materials, Department of Physical Chemistry, Abo Akademi University, Porthansgatan 3-5, FIN-20500 Turku, Finland

²Department of Biochemistry and Food Chemistry, University of Turku, FIN-20014 Turku, Finland

Correspondence should be addressed to Mika Lindén, mlinden@abo.fi

Received 17 October 2007; Accepted 11 January 2008

Recommended by Donglu Shi

Different means of attaching streptavidin to surface functionalized silica particles with a diameter of 240 nm were investigated with special focus on suspension stability for electrostatically stabilized suspensions. The influence of two different fluorescent dyes covalently linked to the streptavidin on suspension stability was also studied. The results clearly show that the stability of the suspensions is crucially dependent on all functional groups present on the surface. The surface functions may either directly affect the effective surface charge if the functions contain charged groups, or indirectly by affecting the relative concentration of charged groups on the particle surface. Poly(ethylene imine)-functionalized silica particles, where the polymer is grown by surface hyperbranching polymerization, are shown to be promising candidates for bioapplications, as the zeta-potential can remain strongly positive even under biologically relevant conditions.

Copyright © 2008 Lotta Bergman et al. This is an open access article distributed under the Creative Commons Attribution License, which permits unrestricted use, distribution, and reproduction in any medium, provided the original work is properly cited.

1. INTRODUCTION

Nanoparticles have been used in diverse biological applications such as fluorescent markers in vitro and in vivo, clinical diagnosis, and drug delivery [1–3]. Nanoparticles have a comparable size to natural carriers and other biomolecules, which gives them the ability to cross physiological barriers and access different tissues followed by an efficient cellular uptake and intracellular internalization [2]. It has been shown that latex particles are endocytosed by nonphagocytic eukaryotic cells for particle sizes up to 500 nm, but the efficiency of cellular uptake decreased with increasing particle size [4, 5]. The highest uptake was observed for particles having diameters of 100–200 nm or smaller, whereas the uptake of particles with diameters of 1 μ m or larger was negligible [5, 6]. Furthermore, it would be beneficial if the particles carry a positive surface charge, as the cell membrane is normally negatively charged [7]. Targeting specific cells and receptor-mediated endocytosis, however, requires surface functionalization of the particles with suitable ligands,

such as antibodies, for which cells do express specific receptors [2]. The linking chemistry is often relying on peptide (amide) bond formation between carboxylic acids and amines and thus the presence of amine or carboxyl groups on the outer particle surface is of special interest.

Silica submicron- or nanoparticles are emerging as a promising and versatile alternative to polymer-based counterparts, as they can easily be produced with a tunable particle size and pore structure. Furthermore, silica is biocompatible and chemically inert under a wide range of conditions [8, 9]. According to several studies, silica nanoparticles are efficiently endocytosed by mammalian cells [1, 10, 11]. Functionalization of the silica surface is relatively straightforward using well-documented methods, which allows the surface chemistry of the particles to be tailored, and also facilitates further attachment of targeting functions. Pristine silica is negatively charged over the pH range of biological interest, as the isoelectric point (IEP) of silica is in the range 2–3. Functionalization of the silica surface can naturally be used to alter the effective surface charge of silica, to an extent which is

controlled by the nature of the introduced functional groups and their surface concentration. The surface charge is important not only from a biological activity point of view, but also for preventing particle agglomeration in suspensions that are electrostatically stabilized. This is especially important under physiological conditions where the electrolyte concentration is high, which decreases the electrostatic repulsion between the particles. Electrostatic stabilization of a nanoparticulate suspension typically requires an absolute zeta potential value of 30 mV or higher. Introduction of additional surface functions onto the pristine or already surface-functionalized particles will typically also influence the effective surface charge of the particles. This could potentially lead to pronounced particle agglomeration even if the original particle suspensions were stable toward agglomeration. The aim of the present study was therefore to evaluate suspension stability for silica nanoparticles with various surface functionalities relevant to biological applications. As model system, nonporous, monodisperse silica nanoparticles with an average size of 240 nm (SEM) were prepared by the Stöber process [12]. The silica particles were first modified by hyperbranching surface polymerization of polyethyleneimine (PEI) using aziridine as precursor. The highly cationic PEI has in itself been used as a polymer film on cell adhesion substrates (instead of poly-L-lysine) [13], and as a versatile nonviral vector alternative for gene delivery [14–17]. Amino-functionalized silica particles have also been successfully employed as DNA carriers for gene delivery [18–20]. The surface concentration of amino groups is notably higher for PEI-functionalized silica, as compared to corresponding particles functionalized by silanization [21]. This is important, as it has recently been shown that silica particles with amino surface functions introduced by silanization actually strongly aggregate under neutral pH conditions [22]. Furthermore, carboxylic acid groups were introduced to the PEI layer in a second step by reaction with succinic anhydride. The surface-functionalized silica particles were further conjugated to the protein streptavidin, either native or labeled with a fluorophore, following three different routes. This opens up the possibility of later using biotin-antibody complexes for targeting cell receptors of interest, as streptavidin has an exceptionally high affinity to biotin. The surface-bound streptavidin retains its activity upon conjugation, as demonstrated by labeling the conjugated particles with Protein A gold using biotinylated alpha 2 integrin antibodies. The particle size and charge were characterized using dynamic light scattering (DLS) measurements and electrokinetic titrations. Imaging of the particles was performed by confocal fluorescence microscopy as well as SEM and TEM. The results are discussed with special emphasis on the stability of the suspension towards aggregation under different conditions.

2. EXPERIMENTAL

2.1. Synthesis of silica Stöber particles

The Stöber synthesis [12] was employed to prepare silica nanoparticles with diameters of about 240 nm with a narrow particle size distribution. In this particular synthesis,

2.6 g tetraethyl orthosilicate (TEOS, 98% Fluka) was added to a solution containing 31.6 g ethanol (99.5%, Altia Oyj), 5.0 g deionized water, and 0.88 g NH₄OH (33%, J.T. Baker), which was stirred at 450 rpm for 20 hours at room temperature. The resultant molar composition was 14.04 : 2.6 : 0.35 : 6.45: 6.45 EtOH: TEOS: NH₃: H₂O. The silica particles were separated by centrifugation (4500 rpm, 5 minutes), washed with ethanol and water, and dried in air at room temperature for one day.

2.2. Surface polymerization of polyethyleneimine

The silica particles were surface modified by surface hyperbranching polymerization of polyethyleneimine (PEI) using aziridine as the precursor. Aziridine was synthesized from aminoethylsulphuric acid (Sigma-Aldrich, Miss, USA) according to the procedure described by Allen et al. [23]. The polymerization was performed in one step under argon atmosphere with toluene as solvent, in which 0.4 g vacuum-dried silica particles were suspended. Catalytic amounts of acetic acid were added under stirring, after which 100 μL aziridine was added to the suspension. The suspension was refluxed under stirring overnight at 348 K, filtered, washed with toluene, and dried in vacuo at 323 K.

2.3. Succinylation of PEI

Succinic acid groups were formed on the PEI-modified surface by the following procedure according to Schiestel et al. [9]. A suspension of 25 mg well-dried PEI-functionalized nanoparticles, 1.5 mL tetrahydrofuran (≥99, 9+%, Sigma-Aldrich), and 25 mg succinic anhydride (97%, Sigma-Aldrich) was shaken for 16 hours at RT. A long reaction time was chosen to maximize the conversion of amine groups. Finally, the particles were filtered, washed with THF, and dried in vacuo at 323 K.

2.4. Binding of glutaraldehyde to PEI

Glutaraldehyde was bound to the amino groups of PEI according to the procedure described by Ashtari et al. [24]. A suspension containing 10 mg PEI-modified silica particles and 5 wt-% glutaraldehyde in 5 mL MeOH was shaken for 2 hours at RT. The particles were subsequently washed twice with phosphate-buffered saline (PBS) (pH 7.4), and separated by centrifugation (2 minutes, 4500 rpm).

3. STREPTAVIDIN CONJUGATION

3.1. Linking streptavidin utilizing carbodiimide chemistry

Carboxylic acid group activation by 1-Ethyl-3-(3-(dimethylamino)propyl)-carbodiimide (EDC) was used to directly conjugate labeled streptavidin (Streptavidin Alexa Fluor 555 conjugate, Invitrogen Molecular Probes) to the amino groups in the PEI layer and to carboxyl acid groups of surface succinic acid groups. The used fluorophore, Alexa555, is a monoreactive, single-isomer succinimidyl ester dye with

an excitation/emission maxima of 555/565 nm and a molar mass of approximately 1250 g/mol. The powder is magenta in color, which facilitates the dye binding recognition visually. In all cases, the particles were intensely pink after the reactions. When indicated, streptavidin conjugated with the DyLight 549 fluorophore (Pierce Biotechnology, Rockford, Ill, USA) was used. The fluorophore DyLight is a photostable orange dye with similar spectra and brightness to Alexa Fluor 555, but with excitation/emission maxima of 550/568 nm in PBS and a molar mass of 982 g/mol.

EDC was used as carboxyl group activating compound to induce the formation of an amide bond between streptavidin and the particle surface. For the particles containing succinic acid groups, EDC was used to form an amide bond between the carboxyl group of succinic acid and streptavidin amino groups. For native PEI-functionalized silica particles, the surface amide bond was formed between PEI-surface amino groups and carboxyl groups of streptavidin (see Scheme 1).

A mixture of 10 mg particles, 5 mL MES ($\geq 99\%$, Sigma-Aldrich)-buffer (0.1 M, pH 5.7), 8.9 μL EDC ($\geq 97\%$, Fluka), and 30 μg labeled streptavidin was prepared. When indicated, unlabeled streptavidin (Streptavidin from *Streptomyces avidii*, Sigma-Aldrich) was used in an otherwise identical mixture. The mixture was stirred for 24 hours at 277 K, in order to retain the activity of the protein. Particles were separated by centrifugation (3 minutes, 4500 rpm) and washed once with MES and twice with PBS.

3.2. Streptavidin conjugation to glutaraldehyde linker

PEI particles with a glutaraldehyde linker were conjugated with streptavidin by preparing a suspension of the following composition: 2 mL PBS, 30 μg streptavidin, and 10 mg particles. When indicated, unlabeled streptavidin (Streptavidin from *Streptomyces avidii*, Sigma-Aldrich) was used in an otherwise identical mixture. The mixture was stirred for 24 hours at 277 K. Streptavidin modified particles were separated by centrifugation (3 minutes, 4500 rpm).

4. CHARACTERIZATION METHODS

4.1. Dynamic light scattering measurements

Dynamic light scattering (DLS) measurements were performed at 298 K using a zetasizer equipment (Model Nano ZS, Malvern, Worcestershire, UK) equipped with a red laser operating at 632.8 nm and the detector positioned at 173° (noninvasive back scattering technology). The data was analyzed using the Malvern Dispersion Technology Software v. 4.20.

4.2. Electrokinetic titrations

The electrokinetic titrations were performed using a Malvern ZetaSizer Nano-ZS coupled with an MPT-2 Titrator unit. The zeta potential was measured as a function of pH by titrating with 0.1 or 0.5 M HCl and NaOH at 298 K. The samples were suspended in deionized water or a saline solution with

the same ionic strength ($\text{NaCl} + \text{KCl} = 150 + 4.2 \text{ mM}$) as PBS-buffer and dispersed by sonication.

4.3. Confocal fluorescence microscopy

Laser scanning confocal microscopy (Carl Zeiss Axiovert 200 M LSM 510 META, Jena, Germany) was performed using a 63x objective, excitation wavelength 543 nm, detection wavelength range $\leq 560 \text{ nm}$, and digital resolution optimized for optical resolution. The images were processed with the BioImageXD software [25]. The measurements were performed on particle suspensions with a concentration of 0.01–0.02 mg/mL in water, which were sonicated before imaging.

4.4. Scanning electron microscopy

SEM images were recorded with a JEOL JSM 6335F, Jeol Ltd, Japan (10 kV) microscope.

4.5. Transmission electron microscopy

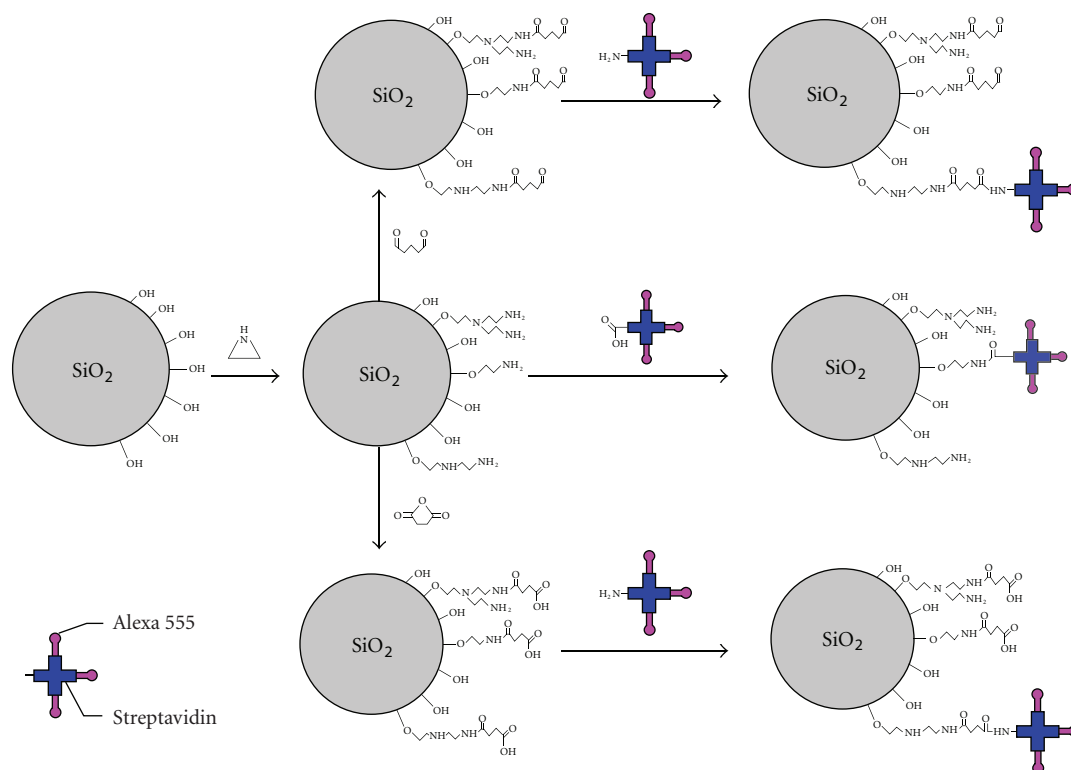
A drop of particle-water suspension of concentration 0.5 mg/mL was pipetted onto a copper grid (460 High Trans + coal crimped Formwar-coated grids, 0.3%), whereafter the solvent was allowed to evaporate and the samples were detected by STEM (JEOL JEM-1200 EX Electron Microscope).

4.6. Biotinylation of antibodies

The alpha 2 integrin antibody (MCA-2025, Serotec) was buffered with 91 mM NaHCO_3 . Biotin N-hydroxysuccinimide Ester (Calbiochem) in DMSO was added to the buffered solution to a final concentration of 0.09 mg/mL. The solution was incubated for 18 hours at 277 K (under gentle agitation). Dialysis was performed in a Slide-A-Lyzer Dialysis Cassette 10 K (Pierce Biotechnology) according to the manufacturers' instructions.

4.7. Gold labeling of streptavidin

Labeling of streptavidin-conjugated particles for TEM was prepared as follows. The 0.5 mg/mL particle suspension was added with biotinylated MCA-2025 alpha 2 integrin antibody to a final concentration of 10 $\mu\text{g}/\text{mL}$ and the mixture was incubated 2.5 hours on a shaker. The particles were washed twice with ion-exchanged H_2O with centrifugation in between the washes (fast spinning down, 14.1 rcf, 4 minutes), centrifuged once more and diluted in H_2O to an approximate concentration of 0.5 mg/mL. The particles were then incubated with 1:100 diluted Protein A gold (diameter: 10 nm) for 13 hours on a shaker at 277 K. The protein A gold reagent, provided as a kind gift from Dr. Varpu Marjomäki, University of Jyväskylä, was prepared according to the procedure described by Slot and Geuze [26] and the OD_{520} of the 1:100 dilution of the reagent was 0.19. Finally, the particles were washed twice with H_2O with centrifugation in between the washes (fast spinning down, 14.1 rcf, 4 minutes), centrifuged once more, and diluted in H_2O to an approximate concentration of 0.5 mg/mL.



SCHEME 1: Modification pathways for conjugation of the labeled streptavidin to the particle surface.

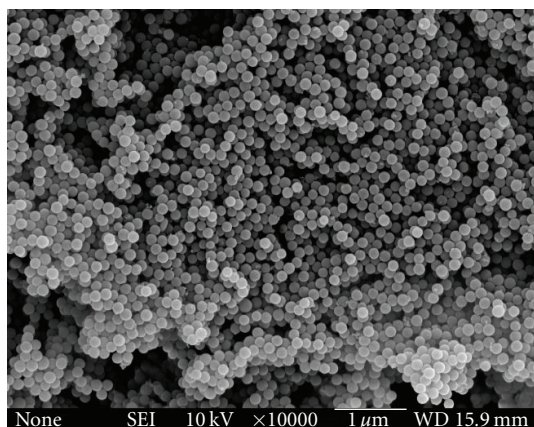


FIGURE 1: SEM image of polyethyleneimine modified silica nanoparticles.

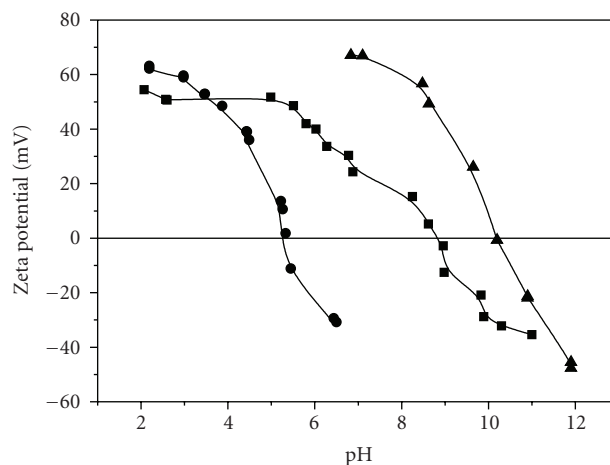


FIGURE 2: Electrokinetic titration curves for functionalized particles in water. PEI-SiO₂ (▲) IEP 10.3, GA-PEI-SiO₂ (■), IEP 9.0, and Succinic acid-PEI-SiO₂ (●), IEP 5.4.

5. RESULTS

5.1. Prefunctionalization of silica particles

An SEM image of the PEI-functionalized particles is shown in Figure 1, demonstrating that all particles are spherical with uniform size. The total PEI content was 7.7 wt% as estimated from thermogravimetric measurements, corresponding to 1.8 mmol amino groups per gram of silica. The concentration of accessible amine groups was estimated based

on the imine method described by Moon et al. [27] and yielded a primary amine concentration of 0.9 mmol per gram of particles. We note that 50% of the amino groups would be primary amino groups in a fully-branched PEI structure with several generations. The electrokinetic titration curve measured in water for the PEI-functionalized silica particles is shown in Figure 2. The isoelectric point (IEP) of the PEI-functionalized silica was 10.3, which can be

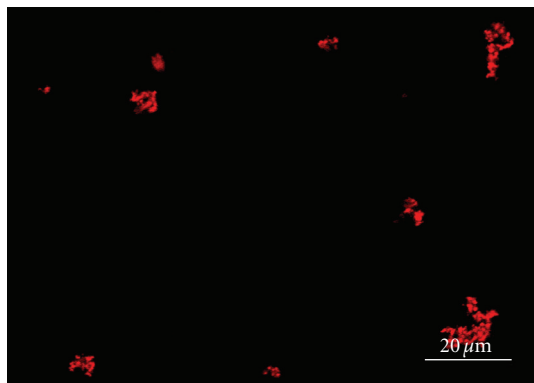


FIGURE 3: PEI-GA-STV(Alexa555) particles (0.01 mg/mL) in water. The scale bar corresponds to 20 μm .

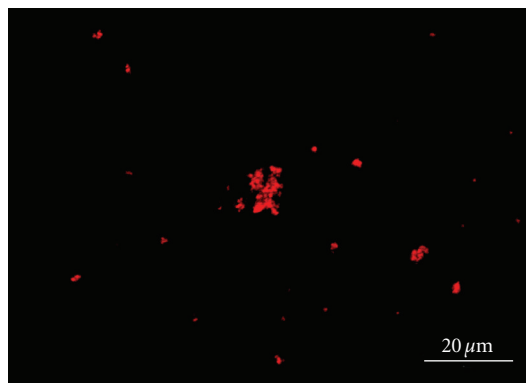


FIGURE 4: PEI-Succinic Acid-STV(Alexa555) in water (0.01 mg/mL). The scale bar corresponds to 20 μm .

compared with the corresponding value of about 2 for the non-functionalized silica particles. The much higher value obtained for the PEI-functionalized particles originates from the presence of amino groups on the surface, which are virtually fully protonated at pH values below 9 as the intrinsic pK_a -value of PEI is 10.6. However, the fact that the PEI-functionalized particles do exhibit an IEP provides evidence for the presence of remaining surface silanols on the particle surface [21]. PEI provides a highly positive charge over a wide pH-range, with a zeta potential of roughly +60 mV in water at neutral pH, which makes the PEI-functionalized silica particles easily dispersible.

As methanol was used as solvent for the reaction of glutaraldehyde (GA) and the PEI-functionalized particles, the functionalization step was performed separately from the streptavidin conjugation step. The isoelectric point decreased from 10.3 to 9.0 after the glutaraldehyde modification (see Figure 2), indicating successful attachment of glutaraldehyde to a fraction of the amine groups. Since the aldehyde group is not a dissociable group, it will not intrinsically contribute to the surface charge density and hence zeta potential, but its effect can be ascribed to the decrease in the effective amino group content of PEI upon glutaraldehyde linking, leading to an increase in the relative concentration of negatively charged silanol groups as compared to positively charged amino groups on the particle surface.

The zeta potential versus pH curve measured for the succinylated PEI-silica particles is shown in Figure 2. The IEP dropped markedly from 10.3 to 5.35 after succinylation, as expected for a successful introduction of carboxylic acid groups. However, the IEP of 5.35 is higher than that expected for a quantitative conversion of amino groups upon succinylation, as the intrinsic pK_a of succinic acid is 4.16. An IEP of 3 has been reported for succinylated amino-functionalized silica particles where the amino groups were introduced by silanization [9]. The higher IEP for the PEI-functionalized particles suggests that some amine groups still remain in the PEI layer after succinylation shifting the IEP towards higher values. The high absolute zeta potential at lower pH also provides evidence for the presence of amino groups remaining from the PEI function.

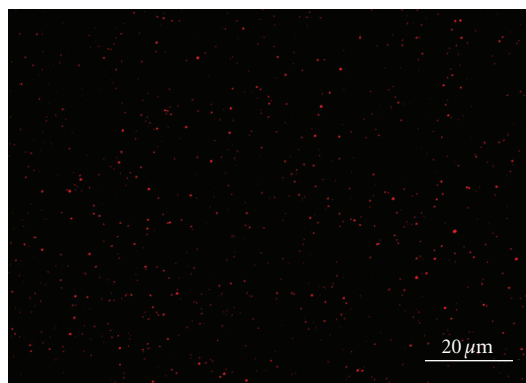


FIGURE 5: PEI-STV(Alexa555) (0.02 mg/mL) in water. The scale bar corresponds to 20 μm .

6. BIOCONJUGATION OF STREPTAVIDIN TO SURFACE-FUNCTIONALIZED SILICA PARTICLES

Electrokinetic titrations were carried out for all streptavidin conjugated particles in both water and a saline solution (0.154 M NaCl + KCl), and the results are summarized in Table 1. We will first focus on the pure water suspensions before returning to discuss the results obtained under saline conditions. When Alexa555-labeled streptavidin was linked to either GA-PEI-SiO₂ or PEI-SiO₂, a clear decrease in the IEPs from 9.0 to 6.1 and from 10.3 to 9.3 was observed, respectively. The decrease in IEP can be understood, as streptavidin has an IEP of 5-6, which is lower than that of the original particles. Furthermore, the linking of the streptavidin to PEI-functionalized particles consumes amino groups, while amino groups in the streptavidin are consumed when linking streptavidin to glutaraldehyde functionalized particles [28, 29]. This could also have an influence on the zeta potential, as could the pH-dependent charging of the Alexa555 fluorophore. For the Alexa555-streptavidin-PEI-SiO₂ particles, the zeta potential value exceeded +40 mV at pH values below about 8 in water, which suggests that these particles are electrostatically stabilized in suspension, while the IEP value

TABLE 1: IEP values for protein-conjugated particles as determined from electrokinetic titrations in water or in saline solution (SS) with the same ionic strength as used in biological media (0.154 M).

	Glutaraldehyde	Succinic acid	PEI
Stv-Alexa555, in water	6.1	5.9	9.3
Stv-Alexa555, in SS	7.1	6.2	8.2
Stv 30 μ g (unlabeled) in SS	8.5	6.2	10.2
Stv-DyLight549, in water	—	—	7.9
Stv-DyLight549, in SS	—	—	6.8

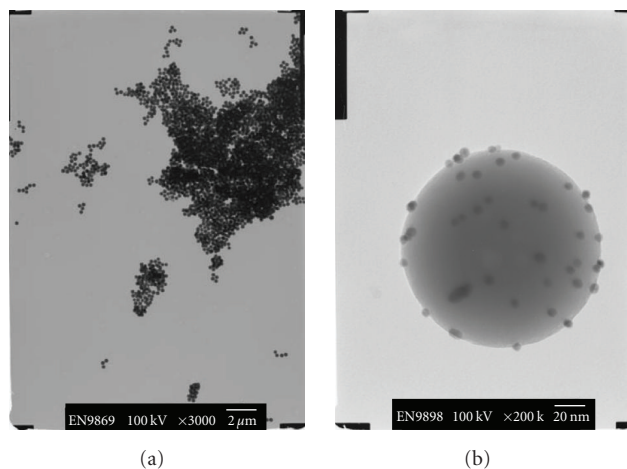


FIGURE 6: PEI-GA-STV(Alexa555) particles, 0.5 mg/mL in water: (a) 3×1000 magnified image and (b) 200×1000 magnified particles where streptavidin is labeled with biotinylated alpha 2 integrin antibody and protein A gold.

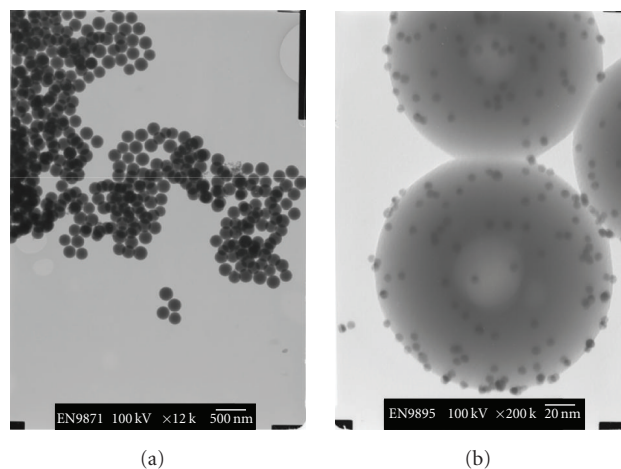


FIGURE 7: PEI-Succinic Acid-STV(Alexa555), 0.5 mg/mL in water: (a) magnified image and (b) 200×1000 magnified image of particles where streptavidin is labeled with protein A gold by using biotinylated alpha 2 integrin antibody.

for the Alexa555-streptavidin-GA-PEI-SiO₂ particles is close to 6, and these particles should therefore not form stable suspensions in water. For succinylated particles, a slight increase in the IEP from 5.35 to 5.9 was observed upon linking fluorescently labeled streptavidin to the particles, hence the net effect of the linking of the streptavidin-Alexa555 complex to the succinylated particles results in an increase in the IEP. Again, the IEP of these particles is very close to the pH of water, so flocculation should be observed in water if the suspensions are electrostatically stabilized.

Confocal fluorescence microscopy was used to study the flocculation behavior of the different fluorescently labeled streptavidin particles in water. The corresponding images are shown in Figures 3–5. All particle types are seen to fluoresce under the conditions applied for microscopic imaging, also indicating a successful conjugation of the labeled streptavidin. For the Alexa555-streptavidin-PEI-SiO₂ suspensions, virtually no flocculation was observed, in agreement with the highly positive zeta potential at a pH of 6 for this system (see Figure 5). For the other two sets of particle suspensions, strong agglomeration was observed (see Figures 3 and 4), in agreement with their low absolute values of the zeta potential. However, in addition to a direct charge-related flocculation effect, also linking of different particles via self-conjugation between outer carboxylic acid and remaining

amino groups (for succinylated particles) or between amino groups (for glutaraldehyde-linked particles), or between proteins during the EDC-mediated coupling reaction, can be expected for both the glutaraldehyde and the succinylation-based systems. The conditions during the EDC-coupling (pH = 5.7) are close to the IEP of the succinylated particles, where the spatial proximity due to particle flocculation might further facilitate possible self-conjugation reactions.

The different extents of particle aggregation can also be observed by TEM, where the samples were prepared by placing a drop of the suspension on a carbon grid followed by evaporation of the water (see Figures 6(a), 7(a), and 8(a)). While the PEI-SiO₂-based particles remain nonaggregated, strong particle agglomeration is seen for the other two systems.

The presence of covalently attached streptavidin on the particle surface and the preservation of the streptavidin activity was ensured in all systems by labeling the streptavidin-conjugated silica particles by biotinylated antibodies in combination with Protein A linked gold particles. The corresponding TEM images of the gold-labeled particles are shown in Figures 6(b), 7(b), and 8(b), where gold particles can be observed on the particle surfaces for the Alexa555-streptavidin functionalized silica particles, regardless of the applied linking chemistry.

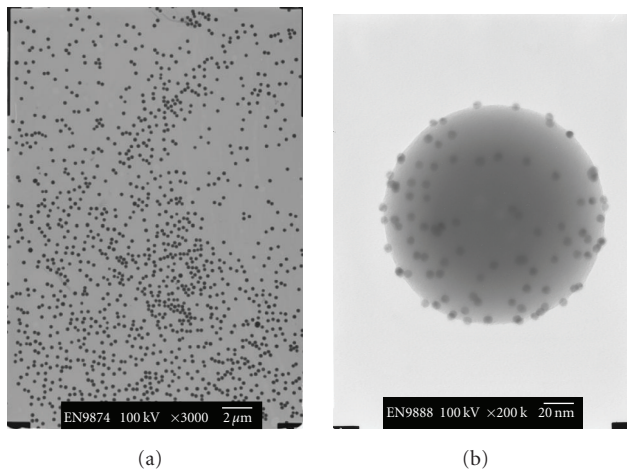


FIGURE 8: PEI-STV(Alexa555), 0.5 mg/mL in water: (a) 3×1000 magnified image and (b) 200×1000 magnified picture of particles where streptavidin is labeled with Protein A gold by using biotinylated alpha 2 integrin antibody.

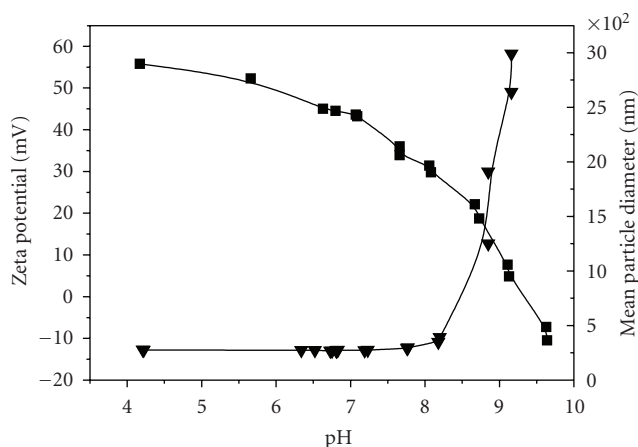


FIGURE 9: Simultaneous electrokinetic titration (■) and particle size determination (▼) (DLS) of SiO₂-PEI-STV(Alexa555) particles in water, IEP 9.3.

In order to study the influence of the fluorophore on the pH-dependent charging of the particles, and thus also on the suspension stability, another set of PEI-SiO₂ functionalized particles was conjugated with streptavidin, but now using a DyLight 549 labeled streptavidin. The zeta potential curves measured in water for DyLight549-PEI-SiO₂ and Alexa555-PEI-SiO₂ are shown in Figures 9 and 10, together with the mean particle size measured simultaneously by dynamic light scattering. While the Alexa555-PEI-SiO₂ suspension remains fully stable up to a pH of about 8, in good agreement with the highly positive zeta potential of +30 mV or higher in this pH range, the DyLight549-PEI-SiO₂ particles have an IEP value of about 7.9, and agglomerate strongly at pHs higher than about 6.5. This is also clearly seen by fluorescence microscopy (see Figure 11). DyLight fluorophores are synthesized through sulfonate addition, which makes DyLight dyes negatively charged and hydrophilic. DyLight dyes are commercially available as succinimidyl esters, which is also the

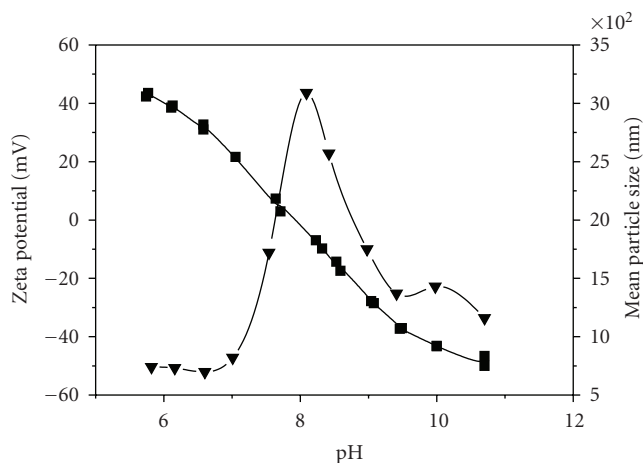


FIGURE 10: Simultaneous electrokinetic titration (■) and particle size determination (▼) (DLS) of SiO₂-PEI-STV(DyLight549) particles in water, IEP 7.9.

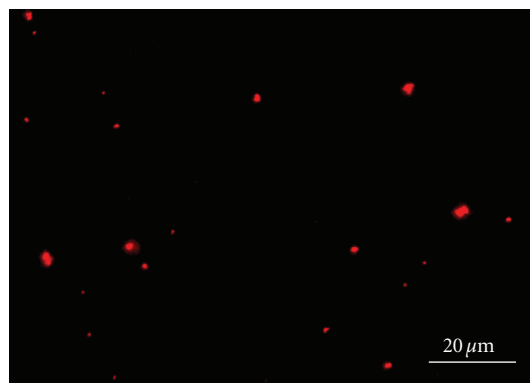


FIGURE 11: PEI-STV(DyLight549) (0.01 mg/mL), in water. The scale bar corresponds to 20 μm .

case for Alexa555. Both fluorophores are hence amine reactive dyes, and are conjugated to free amine groups of the streptavidin tetramer, so the conjugation chemistry of the two fluorophores to the protein molecules is similar. These results indicate that also the charging of the fluorophore has a strong influence on suspension stability.

7. EFFECT OF THE CONJUGATED STREPTAVIDIN

To investigate the effect under conditions relevant to bio-applications, electrokinetic measurements were carried out in saline (0.154 M NaCl + KCl) solutions for both the labeled protein-particle complexes as well as nonlabeled streptavidin-particle complexes at a concentration of 3 μg streptavidin per mg of particles. The results are summarized in Table 1 with the corresponding titration curves in Figure 12. The IEP values for the different Alexa555-streptavidin labeled SiO₂ particles are close to, but slightly

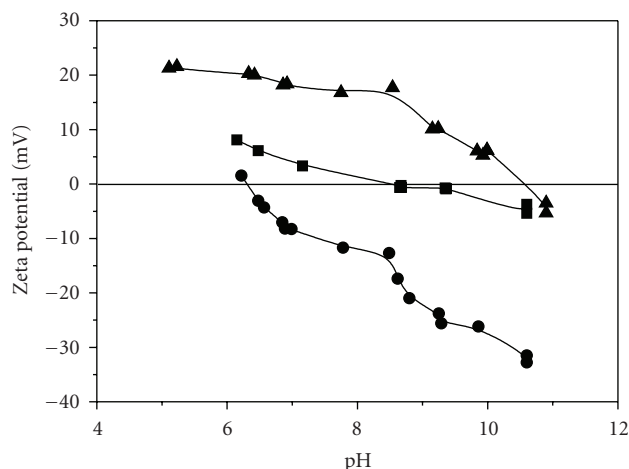


FIGURE 12: Electrokinetic titration curves for unlabeled streptavidin-conjugated particles in salt solution. STV-PEI-SiO₂ (▲) IEP 10.2, STV-GA-PEI-SiO₂ (●), IEP 8.5, and STV-Succinic acid-PEI-SiO₂ (■), IEP 6.2.

different from, the values obtained in pure water, which can be ascribed to electrolyte effects on the effective pK_a values of the different ionizable groups present in the different systems. More importantly, the absolute values of the zeta potential are well below 30 mV in all cases at pH = 7.4, which means that the suspensions would be agglomerated under these conditions. Interestingly, the IEP of the PEI-SiO₂ labeled with native streptavidin is very high, 10.2, and the effective zeta potential at a pH of 7.4 is about 20 mV, which suggests that this system could be fairly stable even under high ionic strength conditions. The strong influence of the Alexa555 fluorophore on the zeta potential is connected to the fact that it is conjugated to the free amine groups of the streptavidin tetramer, which decreases the number of positively charged groups in the system.

8. SUMMARY AND OUTLOOK

Suspension stability is important in many bioapplications, including drug delivery and targeting of cells. As shown above, the suspension stability in a given electrostatically stabilized nanoparticulate system is affected by the linker chemistry applied for surface functionalization related to targeting and imaging, by the surface charge behavior of the biological molecules, and by any additional function introduced, in our case a fluorescent dye. PEI-functionalized silica particles are shown to be very promising candidates for biological applications due to their high positive effective surface charge even under conditions of high ionic strength, provided that the introduced additional surface functions do not decrease the IEP of the particles to values close to neutral. Furthermore, as it should be possible to control the thickness of the PEI layer by variation of the aziridine to silica ratio used in the surface functionalization step, it should be possible to extend the stabilization from electrostatic to electrosteric stabilization without changing the functionalization chemistry.

Such studies are underway in our laboratory. Thus, it should be possible to develop completely stable nanoparticulate suspensions that can be used for targeting and imaging in biological systems based on PEI-functionalized SiO₂.

ACKNOWLEDGMENTS

We would like to thank the personnel of the Laboratory of Electron Microscopy, University of Turku, and the personnel of the Cell Imaging Core at Turku Centre for Biotechnology, University of Turku, and Åbo Akademi University, for kind assistance in microscopy.

REFERENCES

- [1] Y.-S. Lin, C.-P. Tsai, H.-Y. Huang, et al., "Well-ordered mesoporous silica nanoparticles as cell markers," *Chemistry of Materials*, vol. 17, no. 18, pp. 4570–4573, 2005.
- [2] J. K. Vasir, M. K. Reddy, and V. D. Labhasetwar, "Nanosystems in drug targeting: opportunities and challenges," *Current Nanoscience*, vol. 1, no. 1, pp. 47–64, 2005.
- [3] P. Sharma, S. Brown, G. Walter, S. Santra, and B. Moudgil, "Nanoparticles for bioimaging," *Advances in Colloid and Interface Science*, vol. 123–126, pp. 471–485, 2006.
- [4] J. Rejman, V. Oberle, I. S. Zuhorn, and D. Hoekstra, "Size-dependent internalization of particles via the pathways of clathrin- and caveolae-mediated endocytosis," *Biochemical Journal*, vol. 377, pp. 159–169, 2004.
- [5] M. M. Amiji, "Nanotechnology—improving targeted delivery," in *Drug Delivery*, pp. 53–56, Touch Briefings, London, UK, 2007.
- [6] I. I. Slowing, B. G. Trewyn, S. Giri, and V. S.-Y. Lin, "Mesoporous silica nanoparticles for drug delivery and biosensing applications," *Advanced Functional Materials*, vol. 17, no. 8, pp. 1225–1236, 2007.
- [7] Z. P. Xu, Q. H. Zeng, G. Q. Lu, and A. B. Yu, "Inorganic nanoparticles as carriers for efficient cellular delivery," *Chemical Engineering Science*, vol. 61, no. 3, pp. 1027–1040, 2006.
- [8] C. Barbé, J. Bartlett, L. Kong, et al., "Silica particles: a novel drug-delivery system," *Advanced Materials*, vol. 16, no. 21, pp. 1959–1966, 2004.
- [9] T. Schiestel, H. Brunner, and G. E. M. Tovar, "Controlled surface functionalization of silica nanospheres by covalent conjugation reactions and preparation of high density streptavidin nanoparticles," *Journal of Nanoscience and Nanotechnology*, vol. 4, no. 5, pp. 504–511, 2004.
- [10] D. R. Radu, C.-Y. Lai, K. Jeftinija, E. W. Rowe, S. Jeftinija, and V. S.-Y. Lin, "A polyamidoamine dendrimer-capped mesoporous silica nanosphere-based gene transfection reagent," *Journal of the American Chemical Society*, vol. 126, no. 41, pp. 13216–13217, 2004.
- [11] I. I. Slowing, B. G. Trewyn, and V. S.-Y. Lin, "Effect of surface functionalization of MCM-41-type mesoporous silica nanoparticles on the endocytosis by human cancer cells," *Journal of the American Chemical Society*, vol. 128, no. 46, pp. 14792–14793, 2006.
- [12] W. Stöber, A. Fink, and E. Bohn, "Controlled growth of monodisperse silica spheres in the micron size range," *Journal of Colloid and Interface Science*, vol. 26, no. 1, pp. 62–69, 1968.
- [13] S. Lakard, G. Herlem, A. Propper, et al., "Adhesion and proliferation of cells on new polymers modified biomaterials," *Bioelectrochemistry*, vol. 62, no. 1, pp. 19–27, 2004.

- [14] O. Boussif, F. Lezoualc'h, M. A. Zanta, et al., "A versatile vector for gene and oligonucleotide transfer into cells in culture and in vivo: polyethylenimine," *Proceedings of the National Academy of Sciences of the United States of America*, vol. 92, no. 16, pp. 7297–7301, 1995.
- [15] W. T. Godbey, K. K. Wu, and A. G. Mikos, "Poly(ethylenimine) and its role in gene delivery," *Journal of Controlled Release*, vol. 60, no. 2-3, pp. 149–160, 1999.
- [16] A. von Harpe, H. Petersen, Y. Li, and T. Kissel, "Characterization of commercially available and synthesized polyethylenimines for gene delivery," *Journal of Controlled Release*, vol. 69, no. 2, pp. 309–322, 2000.
- [17] K. Kunath, A. von Harpe, D. Fischer, et al., "Low-molecular-weight polyethylenimine as a non-viral vector for DNA delivery: comparison of physicochemical properties, transfection efficiency and in vivo distribution with high-molecular-weight polyethylenimine," *Journal of Controlled Release*, vol. 89, no. 1, pp. 113–125, 2003.
- [18] Z. Csögör, M. Nacken, M. Sameti, C.-M. Lehr, and H. Schmidt, "Modified silica particles for gene delivery," *Materials Science and Engineering C*, vol. 23, no. 1-2, pp. 93–97, 2003.
- [19] C. Kneuer, M. Sameti, E. G. Haltner, et al., "Silica nanoparticles modified with aminosilanes as carriers for plasmid DNA," *International Journal of Pharmaceutics*, vol. 196, no. 2, pp. 257–261, 2000.
- [20] M. N. V. Ravi Kumar, M. Sameti, S. S. Mohapatra, et al., "Cationic silica nanoparticles as gene carriers: synthesis, characterization and transfection efficiency in vitro and in vivo," *Journal of Nanoscience and Nanotechnology*, vol. 4, no. 7, pp. 876–881, 2004.
- [21] J. Rosenholm and M. Lindén, "Wet-chemical analysis of surface concentration of accessible groups on different amino-functionalized mesoporous SBA-15 silicas," *Chemistry of Materials*, vol. 19, no. 20, pp. 5023–5034, 2007.
- [22] R. P. Bagwe, L. R. Hilliard, and W. Tan, "Surface modification of silica nanoparticles to reduce aggregation and nonspecific binding," *Langmuir*, vol. 22, no. 9, pp. 4357–4362, 2006.
- [23] C. F. H. Allen, F. W. Spangler, and E. R. Webster, "Ethyleneimine," in *Organic Syntheses*, N. Rabjohn, Ed., vol. 4, pp. 433–435, John Wiley & Sons, New York, NY, USA, 1963.
- [24] P. Ashtari, X. He, K. Wang, and P. Gong, "An efficient method for recovery of target ssDNA based on amino-modified silica-coated magnetic nanoparticles," *Talanta*, vol. 67, no. 3, pp. 548–554, 2005.
- [25] P. Kankaanpää, K. Pahajoki, V. Marjomäki, J. Heino, and D. White, "BioImageXD — New open source free software for the processing, analysis and visualization of multidimensional microscopic images," *Microscopy Today*, vol. 14, no. 3, pp. 12–16, 2006.
- [26] J. W. Slot and H. J. Geuze, "A new method of preparing gold probes for multiple-labeling cytochemistry," *European Journal of Cell Biology*, vol. 38, no. 1, pp. 87–93, 1985.
- [27] J. H. Moon, J. W. Shin, S. Y. Kim, and J. W. Park, "Formation of uniform aminosilane thin layers: an imine formation to measure relative surface density of the amine group," *Langmuir*, vol. 12, no. 20, pp. 4621–4624, 1996.
- [28] S. O. Molin, H. Nygren, and L. Dolonius, "A new method for the study of glutaraldehyde-induced crosslinking properties in proteins with special reference to the reaction with amino groups," *Journal of Histochemistry & Cytochemistry*, vol. 26, no. 5, pp. 412–414, 1978.
- [29] A. F. S. Habeeb and R. Hiramoto, "Reaction of proteins with glutaraldehyde," *Archives of Biochemistry and Biophysics*, vol. 126, no. 1, pp. 16–26, 1968.

Review Article

Atomic Layer Thermopile Materials: Physics and Application

P. X. Zhang^{1,2} and H.-U. Habermeier^{1,2}

¹ Institute of Advanced Materials for Photoelectrons, Kunming University of Science and Technology, Kunming 650051, China

² Max-Planck-Institut für Festkörperforschung, D-70569 Stuttgart, Germany

Correspondence should be addressed to P. X. Zhang, pxzhang@fkf.mpg.de

Received 20 August 2007; Accepted 16 May 2008

Recommended by Donglu Shi

New types of thermoelectric materials characterized by highly anisotropic Fermi surfaces and thus anisotropic Seebeck coefficients are reviewed. Early studies revealed that there is an induced voltage in high T_C oxide superconductors when the surface of the films is exposed to short light pulses. Subsequent investigations proved that the effect is due to anisotropic components of the Seebeck tensor, and the type of materials is referred to atomic layer thermopile (ALT). Our recent studies indicate that multilayer thin films at the nanoscale demonstrate enhanced ALT properties. This is in agreement with the prediction in seeking the larger figure of merit (ZT) thermoelectric materials in nanostructures. The study of ALT materials provides both deep insight of anisotropic transport property of these materials and at the same time potential materials for applications, such as light detector and microcooler. By measuring the ALT properties under various perturbations, it is found that the information on anisotropic transport properties can be provided. The information sometimes is not easily obtained by other tools due to the nanoscale phase coexistence in these materials. Also, some remained open questions and future development in this research direction have been well discussed.

Copyright © 2008 P. X. Zhang and H.-U. Habermeier. This is an open access article distributed under the Creative Commons Attribution License, which permits unrestricted use, distribution, and reproduction in any medium, provided the original work is properly cited.

1. INTRODUCTION

The experiment of laser-induced voltage (LIV) effect, in which the $\text{YBa}_2\text{Cu}_3\text{O}_{7-\delta}$ (YBCO) thin films were used as a photosensor, was performed firstly by Chang et al. [1]. It was found that there is an induced voltage when pulsed laser light on the surface of YBCO thin films. It is proved that this LIV signal is induced by a thermoelectric anisotropy in the high T_C superconductor (HTSC) oxides [2–5]. These films absorb incident laser radiation, the top surface of thin film is heated rapidly, and an instant temperature difference between the top and bottom parts of the films is generated. This temperature gradient produces an electric voltage through the difference between components of the Seebeck tensor. This anisotropy in thermoelectricity originates from the anisotropic shape of the Fermi surface, causing the different properties of atomic layers in the HTSC oxides with low and high conductivity.

They behave like the two metals of a thermocouple. Therefore, these materials are called atomic layer thermopile (ALT). LIV signals become even larger if the films are grown on vicinal cut substrates because the vicinal cut structure offers more atomic layer junctions upon the

interface. Figure 1 shows the typical time response of an induced voltage with incident pulsed laser of duration of 20 nanoseconds. The first quantitative description of this phenomenon was due to Lengfellner et al. [3], subsequently these signals observed in the ALT materials were defined as laser induced thermoelectric voltages (LITVs). Since then several high T_C superconductor oxides such as doped YBCO, $\text{Bi}_2\text{Sr}_2\text{CaCu}_2\text{O}_8$, $\text{Tl}_2\text{Ba}_2\text{CaCu}_2\text{O}_8$, and so forth have been studied and all of them have shown a similar effect [6–8]. Based on these studies, light detection devices have been designed [9–13], this demonstrates some superior characteristics over traditional bolometer and photon counting devices. Most obvious advantages are that the device can function over a broad spectral range at room temperature, has a fast time response and no applied bias is required.

In 1998, Habermeier et al. observed a similar effect in thin films of the quasicubic $\text{La}_{0.67}\text{Ca}_{0.33}\text{MnO}_3$ grown on vicinal cut substrates [14, 15]. This discovery showed that the ALT property is not confined to HTSC oxide materials, but subsists in other materials. On the other hand, Lanthanum manganites, which are interesting for their colossal magnetoresistance (CMR) properties, have attracted a lot of attention both from the viewpoint of

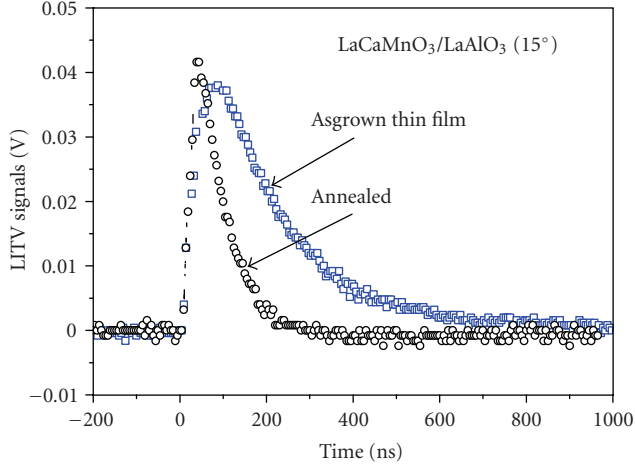


FIGURE 1: Typical laser induced voltage responses from the as-grown and annealed LaCaMnO_3 thin films grown on 15° tilted LaAlO_3 substrates, respectively.

basic physics as well as potential applications. The discovery extends the field of application and also provides new insight for the understanding the discipline of “strong-correlated electrons.”

The LITV signal observed in ALT materials may be a general effect, and it has been well conscious of that the effect can be applied on several devices. However, there is no detailed relation between correlative macroscopic parameters of the used materials and the device performances. We derived a new formula based on a plane heat source and a thermal diffusion model [12]. This new formula does not only correlate the used material parameters with the device performances, but also facilitate the interpretation of physical mechanism of ALT materials.

Recently, several new ALT materials were reported, which belong to members of Ruddlesden-Popper family [15, 16]. Due to their different physical properties, they are suited to function at different spectral ranges or time responses. A new experiment shows that the superlattice like multilayer thin films grown on vicinal cut substrates demonstrate enhanced LITV signals. We will discuss these new ALT materials in detail in Section 3.

The first application of ALT materials is in light detection with advantages of fast time and broad spectral response, operating at room temperature, with no bias required. Based on the reverse effect, the Peltier effect, one can design microcooler. Examples and device design consideration will be given in Section 4.

The LITV measurements of HTSC and CMR thin films provide some important microscopic information on these materials. The direct information obtained is the anisotropy of the Seebeck coefficients, which are valuable for studying the transport property. In strongly correlated electronic system, like HTSC and CMR, currently the discussion has the focus on the nature of the phase coexistence. The measured LITV signals from HTSC and CMR are very sensitive to the doping, strain, oxygen content, charge- and orbital ordering,

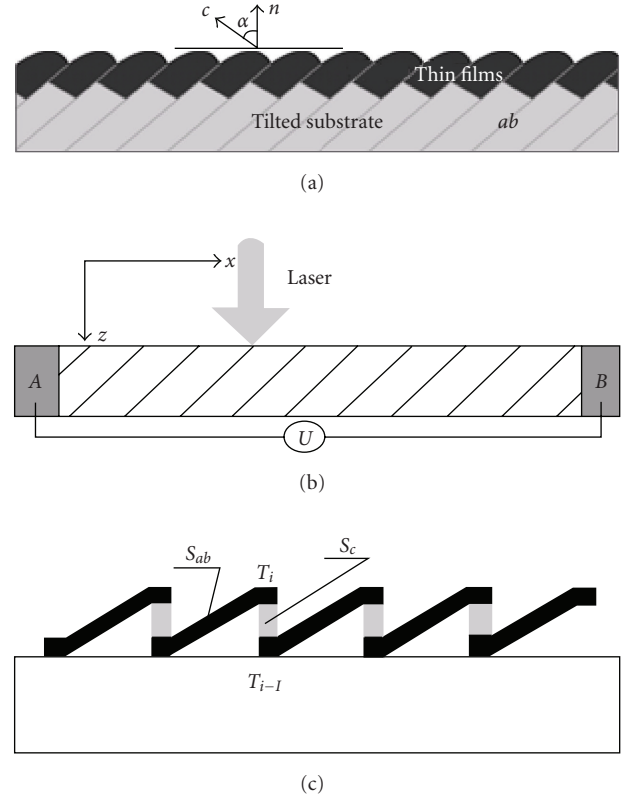


FIGURE 2: (a) The atomic layer thermopile thin film structure and the related coordinators. (b) The configuration of the samples used in the LITV measurements. (c) The schematic atomic layer thermopile model.

as well as the external perturbations such as the temperature, the applied magnetic field, and pressure. The information on anisotropic transport in these materials is regarded as being very important and hard to obtain through other experimental methods.

Although the ALT model and the transport mechanism of CMR materials have been well established, a number of questions in these studies are still needed to be answered, for example, why do CMR thin films exhibit anisotropic Seebeck effect even they are mostly cubic and in a paramagnetic phase, are there other materials which contain even larger ALT property? These open questions will be summarized at the end of this paper.

2. BASIC PRINCIPLES

A thermoelectric field E in a crystal can be induced by a temperature gradient ΔT :

$$E = S \cdot \Delta T, \quad (1)$$

where S is Seebeck tensor. For a thin film grown on vicinal cut substrate (See Figure 2(a)), illuminated by a laser pulse on the surface, a temperature gradient ΔT in z -direction is generated causing an induced voltage signal along the x -direction (U_x) due to the nonvanishing off-diagonal components of the Seebeck tensor. Based on the

experimental observations in $\text{YBa}_2\text{Cu}_3\text{O}_{7-\delta}$, Lengfellner et al. derived a formula according to (1) [3] as follows:

$$Ux = \frac{1}{2d} (S_{ab} - S_c) \sin(2\alpha) \bar{\nabla}_z T, \quad (2)$$

where $S_{ab} - S_c$ is the difference of the Seebeck coefficients in the ab plane and c direction of YBCO, respectively. l and d are the illuminated length and thickness of the film, α is the angle between the surface normal and c -axis of the substrate, ΔT the temperature difference between the top and bottom part of the film. With this formula, one can explain most of the observed experimental facts, and also identify the nature of a laser-induced thermoelectric voltage from other photoinduced effect experimentally. According to this formula, the key factor is $S_{ab} - S_c$, that is, the anisotropy of Seebeck coefficient. Large transport anisotropy implies large induced voltage. It is well known that the properties of atomic layers in $\text{YBa}_2\text{Cu}_3\text{O}_7$ are very different: the CuO_2 layer is highly conductive, while the $\text{Y}(\text{Ba})\text{-O}$ layer has a low conductivity, as well as the Seebeck coefficients. Each two atomic layers form a junction like the thermocouple. If the thin films are grown on vicinal cut substrate, numerous of junction structures, which seem as the series thermocouples, form spontaneously on the surface, as shown in Figure 2(c). With a pulsed light irradiating on the film surface, the top surface is heated fleetly due to the light absorption, and a temperature gradient is developed, thus a thermoelectric voltage is produced in each junction. Due to the large number of junctions, the total induced voltage is very high, and the time response is very short since the distance for the carriers to move is very short.

Figure 3 shows tilting angle dependence of the LITV peak values measured in the YBCO films grown on the SrTiO_3 (STO) substrate. The results indicate clearly that $\sin(2\alpha)$ relation between the peak value of induced voltage and the tilting angle of the substrate is followed. Due to the difficulty in growing high-quality YBCO film on the substrate with high tilting angle, the exception of the sample grown on 20° tilted substrate does not increase with the increase tilting angle any more. ΔT depends on the incident photon fluency and the absorption of the film for the corresponding photon energy. High absorption and small penetration of the light in films lead to large ΔT and thus large induced voltage. The longer the illuminated film length l , the larger the induced voltage, that is, the more atomic scale thermocouples contributes to the thermoelectric signals. The thinner the film thickness (smaller d), the larger the induced voltage, this is correct when the films are relatively thick. However, the description in (2) is proved to be unreasonable at very thin films. Figure 4(a) shows the LITV peak values versus different thickness in YBCO films grown on STO [5]. The increase of the peak value with reducing thickness is followed above 250 nm, but the peak value undergoes a reduction below 250 nm, this dependence cannot be simply ascribed to the loss of the perfection of the thermopile arrangement. To explain this abnormal behavior, an improved model has been derived to describe the LITV mechanism. We would like to discuss this in the following.

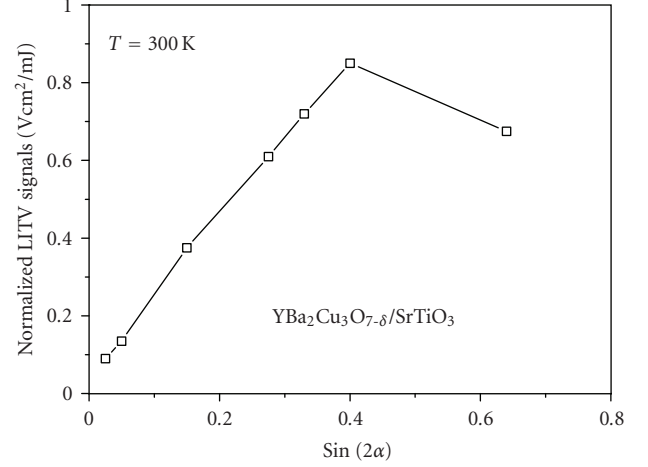


FIGURE 3: Measured LITV signals versus tilting angle of the substrate on which films are grown. The deviation from linear relation of last point is due to the poor film quality grown on the larger lattice mismatched substrate.

In order to correlate the material parameters to the induced voltage and the device performance, a new equation has been derived based on a plane heat source and cascade power net model [12]:

$$U(t) = \frac{\alpha_0 E l \sin(2\alpha)}{4d\rho c_0 \sqrt{\pi D t}} (S_{ab} - S_c) (e^{-\delta^2/4Dt} - e^{-d^2/4Dt}), \quad (3)$$

where $U(t)$ is time-dependent LITV signal, α_0 , ρ , δ , c_0 , and D are the absorption coefficient, density, light penetration depth, specific heat, and thermal diffusivity of the film material, respectively. E is the energy of the incident pulsed laser integrated over the pulse duration, and all other parameters share the same definition with that. This formula provides three important results. Firstly, the peak of LITV signal is no more monotonic variation with the thickness d , in fact, an optimum thickness d_m which is corresponding to a maximum peak of the induced signal does exist. Secondly, to achieve a fast time response, materials with small thermal diffusivity D should be selected. This is totally reasonable within the frame of this new mechanism, and the response time now can be calculated quantitatively based on this formula. Thirdly, the LITV signal is affected by the light absorption of the film materials. Large absorption of the materials implies larger induced voltage. If a small penetration depth δ for the incident light is fulfilled, then both large voltage and fast time response can be achieved at the same time. On the other hand, Wang et al. has deduced the function of deciding the optimum thickness of film materials by using their differential equation of (3) and some suitable boundary conditions [17]. With inputting the material parameters of YBCO film, one can obtain the calculated peak value U_p as a function of d , as shown in Figure 4(b). It is found that the optimum thickness of YBCO film for producing the maximum U_p is about 215 nm. The calculations agree with the LITV experiments very well. As a result, based on (3) and its derivative equations, it

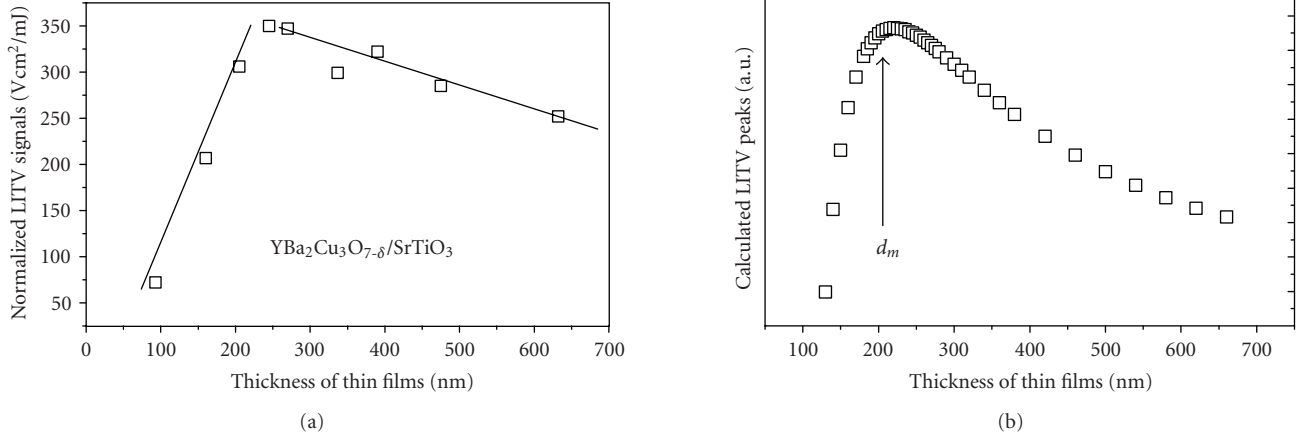


FIGURE 4: (a) The measured and (b) calculated LITV signals from YBCO thin films of different thicknesses are compared. The solid lines in (a) are only used to guild eyes. Both the results show there is an optimum thickness for producing the largest LITV signal.

TABLE 1: The parameters of materials obtained by fitting the measured LITV curves using (3).

Parameter	$S_{ab} - S_c (\mu V/K)$	$D (m^2/s)$	$\Delta (nm)$	$d_m (nm)$
YBCO	10	7×10^{-7}	96.8	215
LCMO	0.22	7.8×10^{-9}	116.2	196

becomes easier for one to select suitable materials to design a light detector in a specified spectral range with desired time response and sensitivity [16–20].

According to the LITV experiments under different perturbations, one can obtain some thin film properties, which may not be easily measured from the bulk value. Figure 5 shows the experimental and calculated LITV signals of the YBCO thin films. The film parameters of YBCO and LaCaMnO₃ obtained from the fitting process are listed in Table 1.

According to Mott’s band theory for non- or weakly interacting electrons, the Seebeck coefficient is expressed as [21]

$$S = -\left(\frac{\pi^2}{3}\right)\left(\frac{K_B^2 T}{e}\right)\left\{\frac{\sigma'(E_F)}{\sigma(E_F)}\right\}, \quad (4)$$

where $\sigma(E_F)$ is the conductivity at Fermi level, and $\sigma'(E_F) = (\partial\sigma/\partial E)|_{E_F}$, K_B and e are Boltzmann’s constant and the elementary charge, respectively. As an approximation, (4) in most of metallic and insulating system can be expressed as $\Delta S/S \sim \Delta\rho/\rho$. It suggests that there is a close relation between the Seebeck coefficient and the resistivity: the larger the resistivity, the larger the Seebeck coefficients. Equation (4) provides the basic relation between the LITV effect and the physical properties of the strong corrected electronic materials, especially the anisotropic transport property, which is valuable information for studying the mechanism of HTSC and CMR materials. On the other hand, it also offers the important hints to seek the more effective ATL materials, since high anisotropy in conductivity links with high Seebeck anisotropy.

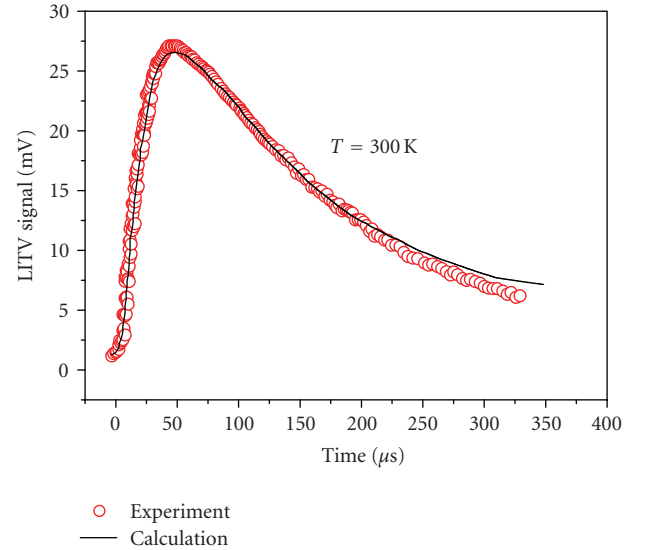


FIGURE 5: The measured and calculated time response curve from YBCO thin films, which demonstrate the new formula is reasonable good in describing the time dependence of the induced voltage. The obtained parameters from the fitting are listed in Table 2.

3. ALT MATERIALS

The ALT behavior is firstly observed in high T_C superconductor oxide YBCO [1]. Later, other HTSC materials, such as doped YBCO, Bi₂Sr₂CaCu₂O₈, Tl₂Ba₂CaCu₂O₈, and so forth, are studied and all of them demonstrate ALT property, only the amplitude and time response of these induced voltages are discrepant in different materials. These oxides are known as highly anisotropic due to the special layer structure. However, they are not stable in normal environment. Therefore, it is very interesting to search more practical materials.

The experimental procedures for investigating ALT materials are composed of two steps: the film preparation and the LITV measurements. The films are grown on vicinal cut

TABLE 2: A recapitulative comparison among the different types of photodetectors.

Parameter	Photon counting (Semiconductors)	Bolometers	ALT devices (LITV signal)
Spectral range	Narrow	Broad	Broad
Response time	Fast (ps)	Slow (ms)	Fast (sub-ps to ns)
Sensitivity	high	high	good
Bias	need	need	Do not need
Working temperature	≤ 300 K	45–110 K	≥ 280 K

substrates by pulsed laser deposition (PLD). Targets used are synthesized by solid-state reaction or coprecipitation, and can be characterized using X-ray diffraction, and other methods. The selection of substrates depends on the lattice parameter of the films to be grown on them. The most frequently used substrates are single crystal SrTiO₃ (STO), LaAlO₃ (LAO), Si, LaSrGaO₄, and MgO, and so forth. The selected films have been characterized by using X-ray, Raman, TEM, and other techniques to ensure that they are single phase grown on substrates. High-quality films are patterned using typical photolithography technique, and after the application of electrodes, one can directly measure the LITV signals. Two LITV measurement methods can be used according to the light source: pulsed laser or continuous-wave light sources [10, 20]. We first report the results of CMR thin film with ABO₃ structure, and then that of other new materials.

3.1. ABO₃-type thin films

At the beginning, it was a surprise to observe the LITV signal in La_{0.67}Ca_{0.33}MnO₃ thin film grown on vicinal cut STO substrates, since no transport anisotropy is expected in such manganites due to their cubic structure and showing paramagnetic phase above T_C . However, the signal is robust and also observed at several other doping levels. We prepared the films on substrates cut at different tilting angles to check whether these signals were induced by thermoelectric effect. Figure 6 shows the LITV obtained from Ag-doped LaCaMnO₃ thin films grown on LAO. It is clear that $\sin(2\alpha)$ relation is followed the large tilting angle of substrate, the larger peak of LITV signal. Therefore, the physics origin of these signals can be assigned to anisotropic Seebeck effect, and the signals were thermoelectric voltages. These experiments have demonstrated that these CMR thin films are a new type of ALT material other than high T_C superconductors. Two arisen questions then have to be answered. Firstly, whether do other manganite films with different compositions or doping levels possess strong LITV signal, so that one can apply these new materials. Secondly, why do these thin films show anisotropic transport properties. Inspired by the discovery, systematic experiments were performed, including that on different doping levels and dopant types.

In the doping experiment of La_{1-x}Ca_xMnO₃ system, it is revealed that the decrease in the doping level of Ca leads to a large induced voltage. According to the phase diagram, it is found that the crystal structure change from cubic to orthorhombic with the reduction of doping level x .

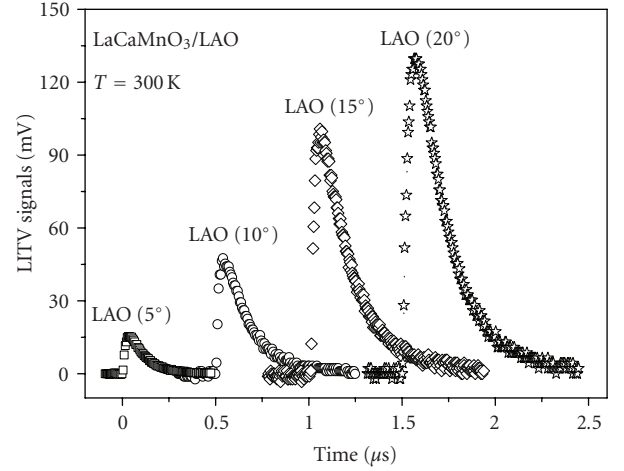


FIGURE 6: The LITV signals of Ag-doped LaCaMnO₃ thin films grown on different tilting angle LaAlO₃ substrates, which demonstrate that the induced voltages are due to thermoelectric anisotropy.

Therefore, a large structural anisotropy can be expected. On the other hand, less doping also changes the magnetic order from ferromagnetic to A-type antiferromagnetic, this process may facilitate the anisotropic transport of electrons at the same time. Another interesting experimental result arises from films grown on different types of substrates. Figure 7 shows the LITV signals from LaCaMnO₃ thin films grown on STO and LAO substrates with the same tilting angle and prepared using identical PLD conditions. The result reveals that the strains due to the mismatch between the lattice parameters of the substrate and the films grown on it have strong influence on the induced thermoelectric voltage.

Except for the La_{1-x}Ca_xMnO₃ thin films, several other doped manganites CMR thin films have been tested and all show similar effect, such as LaSrMnO₃, LaCaSrMnO₃, LaPbMnO₃ (LPMO), and LaBaMnO₃ [22–25]. We also synthesized cobaltite and other transition metal oxides with perovskite structure, which also demonstrate ALT properties. One typical example is the La_{0.5}Sr_{0.5}CoO₃ grown on vicinal cut LAO substrates. La_{0.5}Sr_{0.5}CoO₃ is a conductive perovskite oxide and used as electrode in fuel cell and buffer layer to grown lead-zirconate-titanate (PZT) thin films on Si substrate. We found that the time response of La_{0.5}Sr_{0.5}CoO₃ thin films is extremely fast [18]. The half width of the response curve is almost the same as the duration of the incident-pulsed laser, as shown in Figure 8(b). Considering

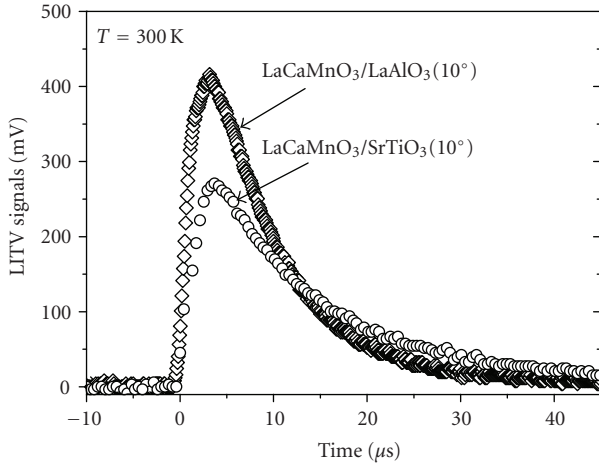


FIGURE 7: The influence of different substrate (LaAlO₃ versus SrTiO₃) on the LITV signals. The LaCaMnO₃ thin films as the samples are used in the measurements.

the limitation of the measuring method, the real time response should be in the order of picoseconds.

The fast time response of LITV in La_{0.5}Sr_{0.5}CoO₃ results apparently from the high-thermal diffusivity, as described in (3). In case of requirement of fast time response applications, La_{0.5}Sr_{0.5}CoO₃ would be a good candidate.

3.2. Ruddlesden-Popper family

Most of the ABO₃-type CMR thin films belongs to the so-called infinite layer or 113 member of Ruddlesden-Popper family, in which the anisotropy is relatively small due to their cubic structure. Therefore, it would be interesting to test other member of Ruddlesden-Popper family. One of the examples is La_{2-x}Sr_xNiO₄ (214 structure) grown on vicinal cut substrates [24]. Large LITV signals have been measured. The first observation of LITV from this compound further enlarges the range for seeking the more effective ALT materials. Comparing with 113 configuration, the 214 structure demonstrates large anisotropic conductivity. Hence large LITV signals can be expected. On the other hand, besides the cuprates, manganites, and cobaltite, La_{2-x}Sr_xNiO₄ is the first nickelate material which exhibits LITV effect. Other members of Ruddlesden-Popper family of HTSC oxides have been measured, and all the materials show high LITV signals [6–8].

3.3. Multilayer thin films

It is well known that man-made superlattices show strong anisotropy in conductivity. Is there the similar anisotropy in Seebeck tensors according to (4)? Following this question, multilayer thin films were prepared by PLD. The samples were composed with different periods (n) YBa₂Cu₃O_{7- δ} and LaPbMnO₃ (YBCO/LPMO) combination. The thickness of each YBCO and LPMO layer was kept at 9 and 6 nm in these multilayer samples, respectively.

The first group multilayer thin films is grown on vicinal cut LAO substrates with the tilting angle of 0°, 5°, 10°, 15°, and 20° between the surface normal and c -axis by pulsed laser deposition technique. Details of the deposition process can be found in our publication [25]. As shown in Figure 9(a), the experiments results demonstrate clearly that the larger the tilting angles the higher the induced voltages. Accordingly, our expectation has been confirmed in this experiment that the observed effect originates from Seebeck effect. Furthermore, the LITV signals are much larger than that of the individual single layer samples with identically total thickness. The YBCO/LPMO superlattices in the second group were deposited on LAO substrates with same tilting angle (10°), but with different number of period as 7, 10, 15, and 20, respectively. The LITV signals of these multilayer thin films with different periods have been presented in Figure 9(b). In order to make a comparison, the LITV signals of YBCO and LPMO single layer films with identical preparation process and measuring condition are also shown in Figure 10. It is evident that the peak value from multilayer YBCO/LPMO sample (20 periods) is about 7 and 34 times larger than that of YBCO and LPMO single-layer films, respectively.

It is known from (2) that the key factor for influencing the induced voltages is the anisotropy of Seebeck tensor ($S_{ab} - S_c$). In the superlattice or multilayer film systems, it is difficult to predict the laser absorption, penetration depth, and specific heat which also directly affect the LITV signal, due to the large variation of these parameters in these special systems. Therefore, one has to focus on the possibility of the enhancement from the discrepancy of Seebeck tensor ($S_{ab} - S_c$). For the multilayer structure, it is obvious that the carrier transportation exhibits high anisotropy. In the layer plane, the conductivity is rather high; while in the perpendicular direction, that is relative smaller. With the increase of the period number, the probability of carrier scattering enhances due to the increase of the defects from the interface. As mentioned in (4), large resistivity leads to large Seebeck coefficient, therefore, the large ($S_{ab} - S_c$). Another key influencing factor is the thermal conductivity. There are numbers of discussion on the thermal conductivity of some manganites with layered structures [26, 27]. Simkin and Mahan have calculated the phonon contribution to thermal conductivity (D) in superlattices. It has been concluded that D is closely related to the number of superlattice periods (n) and the phonon mean-free path. The heat conduction in perpendicular direction of the layer plane is highest for the samples with small n , and rapidly decreases with n increases, after reaching a minimum within the range of $n = 7-15$, increases again. The smaller the mean-free path of phonon implies the smaller the n , at which the minimum thermal conductivity is achieved. In superlattice materials, the electrons are confined for certain situation, and the phonons are scattered at the interfaces. Therefore, the high-thermoelectric figure of merit (ZT) is expected, and indeed the ZT as high as 2 to 3 have been measured in several experiments [28–30].

The possible enhancement of ($S_{ab} - S_c$) may originate from the stressed lattices. According to X-ray diffraction,

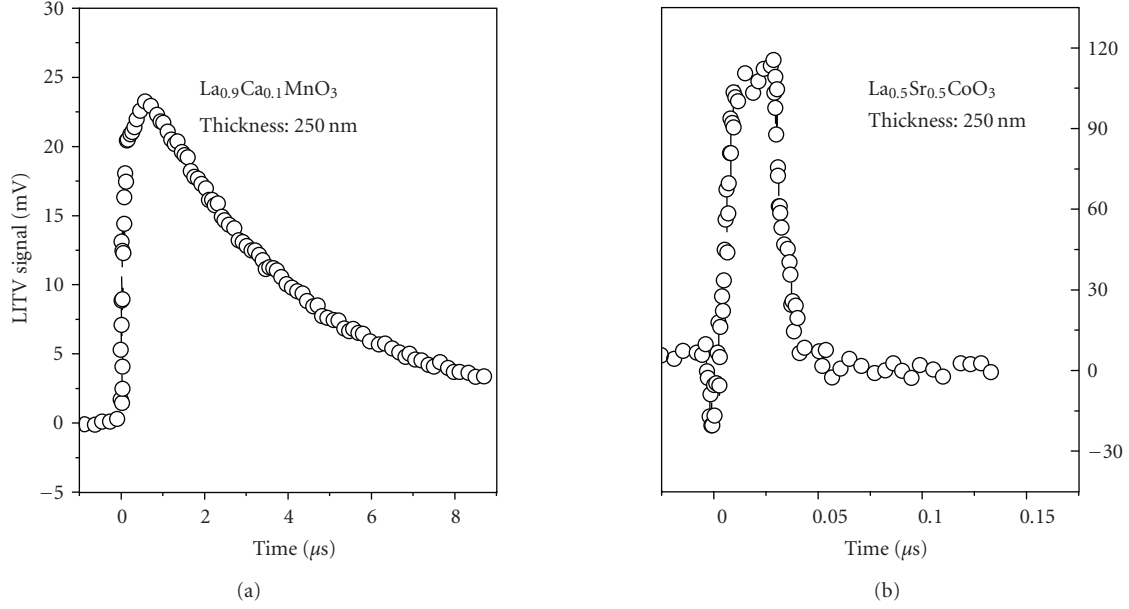


FIGURE 8: (a) The LITV time response curves from LaCaMnO₃ and (b) LaSrCoO₃ thin films. It is shown that the time response of LaSrCoO₃ is very fast (ps-ns) due to its high conductivity.

both YBCO and LPMO films are compressively stressed in *ab* plane due to the smaller lattice parameter of LAO substrate. Therefore, the lattice parameters in *c*-direction were enlarged assuming preservation of the volume of the unit cell. The large mismatch and the sandwiched structure can keep this strain in the whole sample. This leads to the variation of intrinsic properties of each component films. Due to the strain effects, the stressed YBCO and LPMO films must show different transport properties, this has been verified by several experiments [16–19, 31].

In a word, there is a huge variety of strong correlated electronic materials which are not yet studied from the viewpoint of their ALT properties. According to our limited research so far, it is clear that most of the materials with layered structure demonstrate ALT properties. For the first time, an enhanced LITV signal from multilayer oxide thin films with a superlattice-like structure is observed. Compared with single-layer film of YBCO or LPMO, the LITV signals of the multilayer sample (the YBCO/LPMO structure with 7 periods) have been enhanced for several times than those obtained in YBCO and LPMO single films. This new observation is interesting for studying the transport properties in superlattice-like multilayer thin films. The unusual enhancement of the light-induced voltages in these multilayer films is possibly related to the large Seebeck anisotropy and the reduction of thermal conductivity in superlattice-like structures. The investigation of these materials and thin films provides candidates for different applications, such as light detection at different wavelengths or time responses. On the other hand, the measured LITV signals from the superlattices-like structures provide information on the anisotropic transport property, which are hard to obtain by other experiments.

4. APPLICATION

Two practical applications have been put forward and tested with the ALT materials. One is light and heat detection, and the other is local cooling based on the reverse of the Seebeck effect, the Peltier effect.

The thermoelectric response of an ALT material has a linear dependence on absorbed radiation power. Therefore, a radiation detector was designed and tested [14, 18–20]. To compare the ALT detectors with those fabricated by other materials, Table 2 lists the main parameters for three types of detectors. Due to the broad absorption of the black surfaces of most of the ALT materials, the LITV detectors can work in broad spectrum range. The experiment shows that these detectors can response from ultraviolet to middle infrared. According to (3), the time response depends on the thermal diffusivity D and the penetration depth δ . By proper selecting the materials responded at special wavelength, response time from micro- to picoseconds is easy to be realized. Other advantages of this type of detectors consist in that they show good performance at room temperature without any biases.

Considering that the importance for fabricating the devices with fast time response and high sensitivity, one can define a device figure of merit (F_m) to describe the performance of the LITV detector [18]:

$$F_m = \frac{U_P}{\tau}, \quad (5)$$

where U_P and τ are the peak value of induced voltage and the full width at half maximum of the response curve of the induced voltages. Therefore, synthesizing and searching for materials with high LITV sensitivity and fast time response at the same time, namely, higher F_m is interesting.

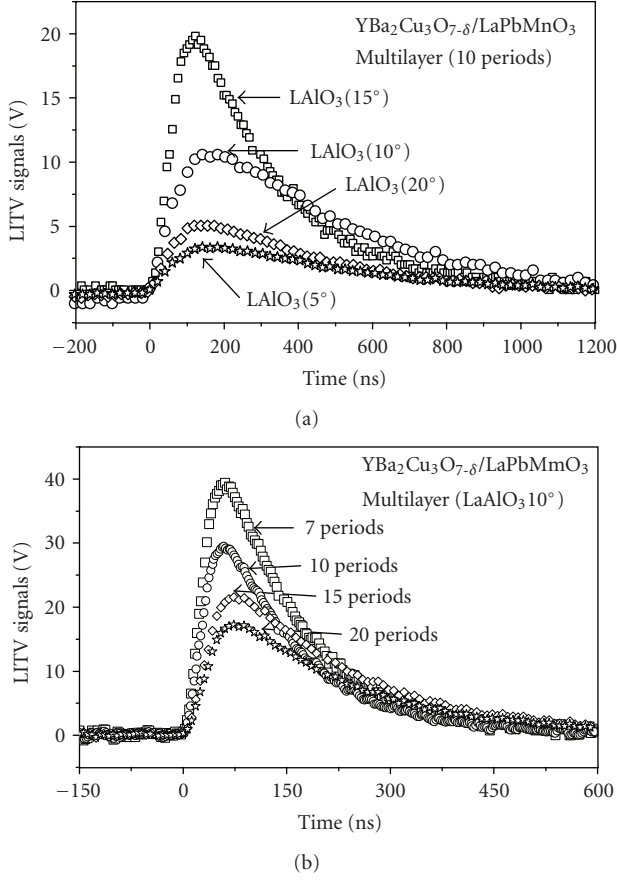


FIGURE 9: (a) The LITV signals from the multilayer YBCO/LPMO thin films with 10 periods grown on different vicinal cut substrates. From these curves, it has been confirmed that the LITV signals originate from thermoelectric anisotropy. (b) The multilayer thin films with different period number n grown on vicinal cut LaAlO_3 (10°) substrates.

TABLE 3: The measured conductivity δ , peak values of LITV signals U_p , time response τ , and the calculated figure of merit for different Ag-doped $\text{La}_{0.6}\text{Pb}_{0.4}\text{MnO}_3$ films grown on LaAlO_3 substrates with 15° angle cut.

Ag-doping level (wt%)	δ (S/cm)	U_p (mV)	τ (ns)	F_m
0	313.8	25	140	0.18
2	567.7	35	106	0.33
4	1302.1	43	80	0.53
6	2125.9	38	65	0.58
8	901.9	48	100	0.48
10	749.4	20	126	0.16

We have prepared Ag-doped $\text{La}_{0.6}\text{Pb}_{0.4}\text{MnO}_3$ (Ag-LPMO) thin films by means of PLD, and investigated the doping level effect on the LITV amplitude. By optimizing the doping level of Ag, it is found that the F_m of the LITV device is improved substantially.

The LITV signals of Ag-LPMO films with different Ag doping levels are shown in Figure 11. The U_p value firstly increases with the increase of Ag doping level, then reaches

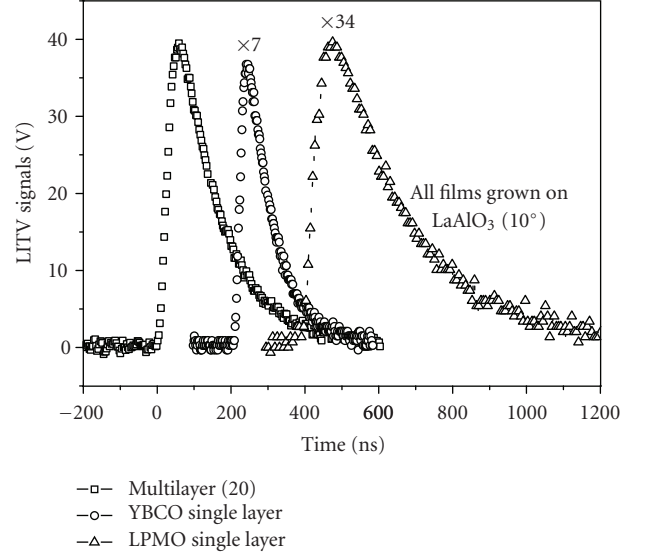


FIGURE 10: The LITV signals of the YBCO/LPMO multilayer film with 20 periods, the 400 nm thick $\text{YBa}_2\text{Cu}_3\text{O}_{7-\delta}$ thin film, and the 400 nm thick LaPbMnO_3 films, respectively. The samples are fabricated and measured at the identical experimental conditions.

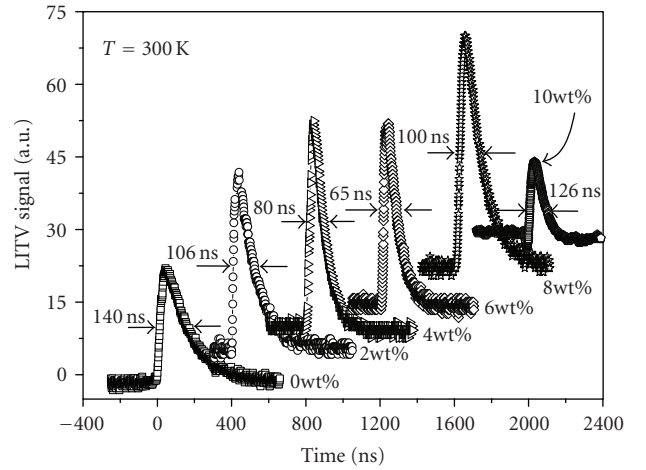


FIGURE 11: Time dependent laser induced voltage curves obtained from different Ag-doped $\text{La}_{0.6}\text{Pb}_{0.4}\text{MnO}_3$ films grown on vicinal cut LaAlO_3 (15°) substrates. These samples are also fabricated and measured at the same experimental conditions. It is shown that the figure of merit of the LITV device can be greatly improved with proper doping level.

a maximum at doping level of 4–6 wt%, finally decreases. At the same time, the time response τ varies with an opposite way, reduce first and then increase. According to (5), one can calculate the F_m values of these devices. Table 3 lists the measured U_p , τ , and the calculated F_m at different Ag-doping levels. It is evident that F_m value can be enhanced to several times by optimizing doping level of Ag.

There are lots of discussion on the enhancement of the ZT of thermoelectric materials, and several new concepts to obtain materials with ZT higher than 1 have been reported

[28–30]. To form materials with “phonon glass and electron crystal” behavior become the central issue to realize large ZT, namely, high-electronic conductivity and low-thermal conductivity. Doping with monovalent ions, such as Ag, either in the lattice or at grain boundary, always enhances electronic conductivity. At the same time, the inhomogeneity is induced by doping Ag because the Ag ions form the centers of phonon scattering. Therefore, doping with Ag in the LaPbMnO₃ films can enhance the ZT, and this may be an effective method for other material system as well.

The reverse effect of Seebeck is Peltier effect, in which a thermoelectric cooling can be realized by simply applying electric current. In an anisotropic material, an applied electrical current density J_e can produce a Peltier heat flow J_h , which is described by

$$J_h = P \cdot J_e, \quad (6)$$

where P is the Peltier tensor, related to Seebeck tensor S , defined as $P = S \cdot T$. The largest temperature difference ΔT_m realized in this effect depends on the thermoelectric figure of merit ZT and is expressed as

$$\Delta T_m = \frac{(ZT)^2}{2}. \quad (7)$$

The cooling effect of ALT materials was firstly observed in YBCO bulk [32]. Recently, more effective cooling effect was realized in a Pb-Bi₂Te₃ multilayer structure [33]. By applying a current in film plane, temperature difference up to 22 K has been observed between top and bottom sides of the sample. The cooling experiments on ALT materials are just launched. However, the renewed interests in microcooling for various applications are pushing the related investigations. The advantages of the type of cooling are easy to realize, without moving parts, matching well with plane technology, and so on.

5. PHYSICAL MECHANISMS AND OPEN QUESTIONS

All crystalline solid materials are composed of atomic layers, therefore, they should have ALT behavior and can be the candidates for the application and LITV measurements. So far, only few have been studied. Large unreached area remains to be explored. The studies of HTSC and CMR thin films have put forward several questions which should be answered, for example, why there is anisotropy in CMR thin films with cubic or quasicubic crystal structure? Even more interesting is that the LITV signals are recorded at temperature above T_C , the films are in paramagnetic phase. What information can be followed by analyzing the LITV signals at different applied perturbations? Clear answer of these questions involves in the mechanisms of charge and phonon transport in the strongly correlated electronic systems, which are also the hot points of condensed matter physics.

We now discuss the origin of LITV signals from CMR thin films and try to answer the origin of the anisotropy in these films. In fact, the existence of LITV signals is closely linked with the mixed phases of the complicated system.

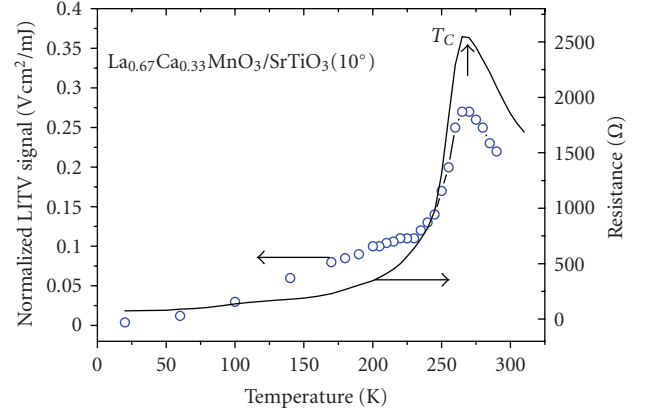


FIGURE 12: Temperature dependence of LITV signals (separated dots) and resistance (solid line) of LaCaMnO₃ thin film. It shows that the amplitude of LITV signals is relative strong around T_C .

Assuming that there are two competing phases near T_C in CMR materials [34–36], the ferromagnetic metallic (FMM) and charge-ordered antiferromagnetic (COAF) insulating phase, the total induced voltage based on (2) is composed of the contribution of the two:

$$U_P = A[S_{an}^1(1 - C) + S_{an}^2 \cdot C], \quad (8)$$

where U_P is the peak value of induced voltages. S_{an}^1 and S_{an}^2 are defined as $(S_{ab} - S_c)$ in COAF and FMM phases, respectively. C is the concentration of FMM phase, which can be evaluated from the measured temperature or applied magnetic fields dependence of magnetization (M) and expressed as $C(H, T) = M(H, T)/M_{sat}$ [37]. A is a constant related to the geometric dimension of the sample and the temperature gradient in the materials produced by the pulsed laser, which is temperature independent in the first approximation. Considering no other phase transition and only the two phases playing important role, two extreme cases can be discussed. At the temperature range of $T \gg T_C$, the FMM phase disappears, C approaches to zero correspondingly. Based on (8), one can evaluate high-temperature Seebeck anisotropy of COAF phase: $S_{an}^1(hT) = U_P(hT)/A$. While in the case of $T \ll T_C$ the contribution of COAF phase is negligible, small one can obtain Seebeck anisotropy of FMM phase at low temperature $S_{an}^2(IT) = U_P(IT)/A$. Figure 12 shows the LITV signals obtained from La_{0.67}Ca_{0.33}MnO₃ thin films grown on STO substrates [14]. According to the above analysis and estimation, the Seebeck anisotropy of COAF phase at high temperature is $S_{an}^1(hT) = 0.2/A$, for FMM phase at low temperature is $S_{an}^2(IT) = 0.01/A$, and a ratio $S_{an}^1(hT)/S_{an}^2(IT) = 20$ was obtained.

These results are reasonable. For the FMM phase, the structure of La_{0.67}Ca_{0.33}MnO₃ is cubic, and the anisotropy is small, while the COAF phase is possibly noncubic [34], this implies that a large anisotropy can be expected. In fact, it is well known that the Seebeck coefficient is closely related to the conductivity. According to (4), the larger the resistivity the larger the Seebeck coefficients. For the two coexistent phases near and above T_C , the FMM phase

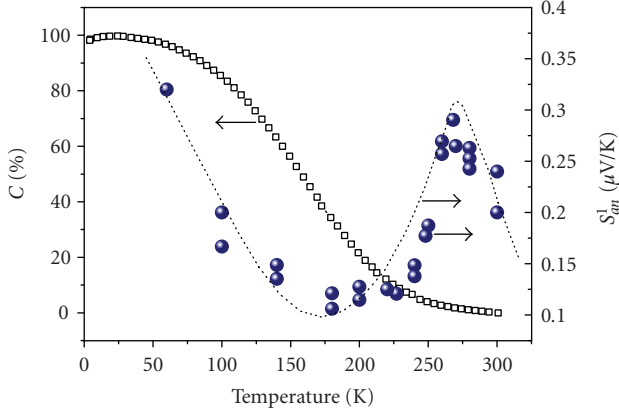


FIGURE 13: Temperature dependence of Seebeck coefficient anisotropy ($S_{an}^1 = S_{ab} - S_c$), deduced from measured LITV signal based on two phases model. The dot line is only used to guide eyes.

is the one with higher conductivity and lower resistivity, therefore the Seebeck coefficients are relative smaller. In addition, due to the cubic structure, the anisotropy should be further suppressed at the same time. On the contrary, the COAF phase is insulating (large resistivity), then a large Seebeck coefficient is expected, and even a large structural anisotropy occurs. With this argument and also considering the evaluated values and the ratio $S_{an}^1(hT)/S_{an}^2(lT) = 20$, one can further simplify (8) as $U_p = AS_{an}^1(1 - c)$. This approximation is valid at temperature near and above T_C . Since C can be evaluated from magnetization measurements accordingly, and based on the measured LITV temperature dependence [8], the temperature dependence of S_{an}^1 is easily estimated. Figure 13 shows the obtained $S_{an}^1 - T$ dependence from experiments, together with the used $M(T)$ curve. Based on these results, the concentration of FMM phase can be easily estimated. With the decrease of temperature, it is shown that the difference of the Seebeck coefficients $S_{an}^1 = (S_{ab} - S_c)$ or the anisotropy of the resistivity in COAF phase increases firstly. After it reach a maximum at around T_C , then the S_{an}^1 decreases again. Since there are significant LITV signals measured above T_C , we would like to emphasize that the anisotropic Seebeck coefficients are robust. Therefore, an anisotropic transport behavior can be definitely observed above T_C in paramagnetic phase of $\text{La}_{0.67}\text{Ca}_{0.33}\text{MnO}_3$ thin films. This is unexpected, since the sample is cubic or quasicubic in terms of its structure, and magnetically is in paramagnetic phase, both factors should not lead to anisotropic transport properties. In fact, the temperature-dependent Seebeck coefficient has been measured at temperature near and above T_C in $\text{La}_{0.67}\text{Ca}_{0.33}\text{MnO}_3$ bulk by Jaime et al. [37], which is an isotropic value, and demonstrated qualitatively the same temperature behavior as the deduced S_{an}^1 from LITV measurements. This means that the difference of $S_{ab} - S_c$ is roughly proportional to the absolute value of S as a function of temperature. The interesting point is that the obtained anisotropic components should be correlated to the structural anisotropy as well as the conductivity anisotropy of a possible COAF phases. Recently, there were a number

of experiments which reported the measurement of Seebeck coefficients from $\text{Pr}_{0.67}\text{D}_{0.33}\text{MnO}_3$ ($D = \text{Ca}, \text{Sr}, \text{Pb}, \text{and Ba}$) by Venkataiah et al. [38, 39], $\text{La}_{0.7}\text{Sr}_{0.3-x}\text{Ag}_x\text{MnO}_3$ by Battabyal and Dey [40], these results demonstrated similar temperature behavior as the one observed in [37]. However, all of the results of their samples are obtained in the bulk materials, and less information on the anisotropy of the thermoelectric effects is given. Furthermore, there is no discussion on the contribution of the competing phase in these materials. Therefore, it is hard to tell which phase is responsible to the anisotropy.

There are several possible phases coexistent with the FMM phase above T_C [41–43]. Figure 14 shows the spin structure in A, C, and G types of antiferromagnetic phases, together with a ferromagnetic (F) and newly proposed CE, E, and C_xE_{1-x} types of charge-ordered antiferromagnetic phases. The parent compounds of doped $\text{La}_{0.67}\text{Ca}_{0.33}\text{MnO}_3$ are LaMnO_3 and CaMnO_3 . The undoped LaMnO_3 is orthorhombic (space group $Pnma$), with magnetic ground state of A-type antiferromagnetic structure. In $a-c$ plane, the alignment of spins is parallel, it indicates the configuration of two-dimensional ferromagnetism. While in the successive plane of b direction, the orientations of the spins are antiparallel. Therefore, the transport anisotropy has been built accordingly, that is, the electrons can move easily in the $a-c$ plane, but difficultly in the b direction due to the antiparallel spin orientation. The other doping end is CaMnO_3 , which is cubic in structure (space group $Pm\bar{3}m$) and with magnetic ground state of G-type antiferromagnetic structure. In this phase, there is no anisotropy originated from crystal and magnetic structure. With different doping levels, the COAF phases could be a mixture of all these phases at temperature near and above T_C . The CE phase is most likely the candidate, which is responsible for an anisotropic transport property. The zigzag conductive chains are in ab planes, while the conductivity in c direction is very poor because the hopping of spin is forbidden. The E-type of COAF phase is similar to CE-type. However, the zigzag chains are composed of two parallel oriented spins. Therefore, there is also anisotropic transport property. The carrier transport may be easier in the zigzag chains than that in CE phase. Up to now, it is hard to directly correlate which phase is responsible for the measured Seebeck anisotropy. More theoretical and structural studies are required to make the question be clearer.

In summary, a new experimental method, laser induced thermoelectric voltage effect from CMR thin films, was used for the first time to reveal the transport anisotropy at temperature near and above T_C in $\text{La}_{0.67}\text{Ca}_{0.33}\text{MnO}_3$ thin film. By neglecting the contribution of FMM phase, the temperature dependence of $S_{ab} - S_c$ in COAF phase was evaluated, this dependence provides clear evidence for the existence of noncubic, highly anisotropic phase above T_C .

The results show that the Seebeck coefficients difference $S_{ab} - S_c$ in COAF phase increases firstly with the lowering temperature, and then reaches a maximum at around T_C , finally decreases again. This information is unique, and may offer great help in correlating COAF phase type as well as the mechanisms of the complicated phase competition

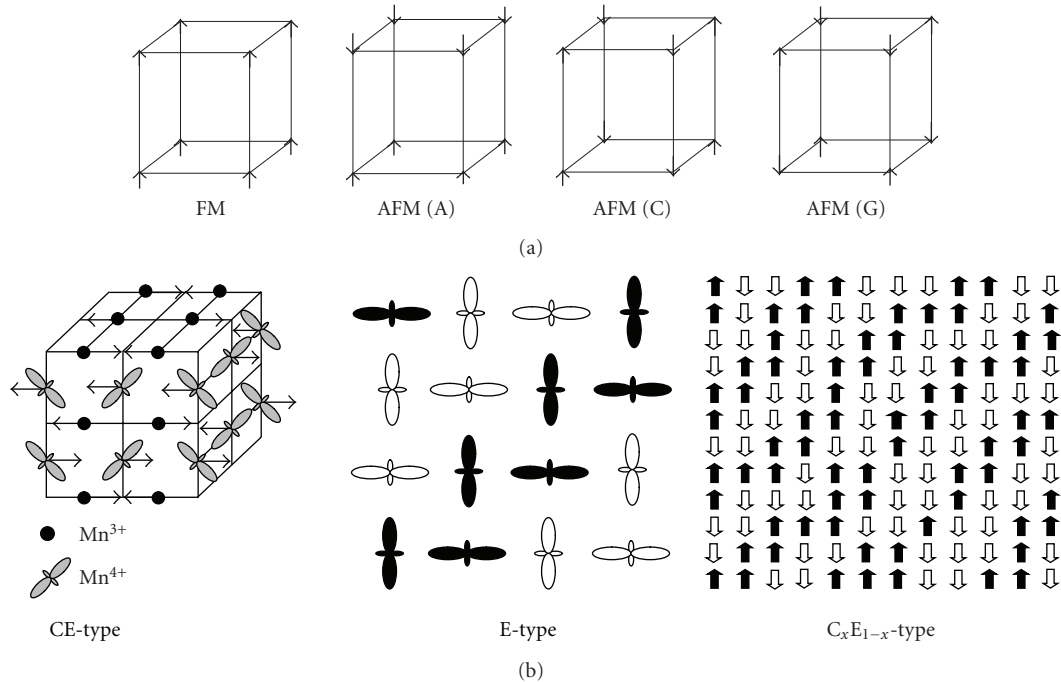


FIGURE 14: The possible antiferromagnetic phases in mixed phases of CMR materials around T_C .

and coexistence in CMR materials. In fact, similar situation is also in high T_C superconductor materials, where a T^* is defined, and little is known on the region between T^* and T_C . Therefore, LITV measurements may contribute valuable information on the anisotropic transport, and hence the physical understanding of strongly correlated electronic systems.

6. CONCLUSION

Atomic layer thermopile (ALT) materials are a new type of materials, which demonstrate novel thermoelectric property. The basic principle originates from the different transport properties in different atomic layers, this induces the anisotropic Seebeck effect. This effect can be used in light or heat detection, and local cooling based on its inverse effect. There are large amounts of materials which may exhibit ALT property, but not yet well studied. The investigations of LITV in different ALT materials provide unique information on transport properties at temperatures especially important for study the mechanism of high T_C superconductor and CMR effect.

ACKNOWLEDGMENTS

P.X. Zhang would like to thank Professor C. Wang (Yunnan University) for the fruitful discussion and technical assistance. Both authors would like to thank X.-H. Li, W.K. Lee, B. Leibold, G. Cristiani, G. Y. Zhang, H. Zhang, and L. Yu for their contributions covering various aspects of this work. The financial supports are from science foundation of China (10274026, 1999E0003Z).

REFERENCES

- [1] C. L. Chang, A. Kleinhammes, W. G. Moulton, and L. R. Testardi, "Symmetry-forbidden laser-induced voltages in $YBa_2Cu_3O_7$," *Physical Review B*, vol. 41, no. 16, pp. 11564–11567, 1990.
- [2] H. S. Kwok, J. P. Zheng, Q. Y. Ying, and R. Rao, "Nonthermal optical response of Y-Ba-Cu-O thin films," *Applied Physics Letters*, vol. 54, no. 24, pp. 2473–2475, 1989.
- [3] H. Lengfellner, G. Kremb, A. Schnellbögl, J. Betz, K. F. Renk, and W. Prettl, "Giant voltages upon surface heating in normal $YBa_2Cu_3O_{7-\delta}$ films suggesting an atomic layer thermopile," *Applied Physics Letters*, vol. 60, no. 4, pp. 501–503, 1992.
- [4] Th. Zahner, R. Schreiner, R. Stierstorfer, et al., "Off-diagonal Seebeck effect and anisotropic thermopower in $Bi_2Sr_2CaCu_2O_8$ thin films," *Europhysics Letters*, vol. 40, no. 6, pp. 673–678, 1997.
- [5] P. X. Zhang, U. Sticher, B. Leibold, and H.-U. Habermeier, "Thickness dependence of the thermoelectric voltages in $YBaCuO_{7-\delta}$ thin films on tilted substrate of $SrTiO_3$," *Physica C*, vol. 282–287, part 4, pp. 2551–2552, 1997.
- [6] L. R. Testardi, "Anomalous laser-induced voltages in $YBa_2Cu_3O_x$ and "off-diagonal" thermoelectricity," *Applied Physics Letters*, vol. 64, no. 18, pp. 2347–2349, 1994.
- [7] Th. Zahner, R. Förg, and H. Lengfellner, "Transverse thermoelectric response of a tilted metallic multilayer structure," *Applied Physics Letters*, vol. 73, no. 10, pp. 1364–1366, 1998.
- [8] X. H. Li, *Strongly correlated oxide thin films and laser induced voltage effect*, doctoral thesis, Institute of Physics, ChineseAcademic Sciences, Beijing, China, 2001.
- [9] S. Zeuner, W. Prettl, and H. Lengfellner, "Fast thermoelectric response of normal state $YBa_2Cu_3O_{7-\delta}$ films," *Applied Physics Letters*, vol. 66, no. 14, pp. 1833–1835, 1995.
- [10] P. X. Zhang, G. Z. Li, X. M. Wen, Y. Zhang, and H.-U. Habermeier, "Room temperature light-thermo-detector made

- of high-T-c superconductor,” *Acta Physica Sinica*, vol. 7, no. 11, pp. 810–816, 1998.
- [11] K. Fischer, C. Stoiber, A. Kyarad, and H. Lengfellner, “Anisotropic thermopower in tilted metallic multilayer structures,” *Applied Physics A*, vol. 78, no. 3, pp. 323–326, 2004.
- [12] P. X. Zhang, W. K. Lee, and G. Y. Zhang, “Time dependence of laser-induced thermoelectric voltages in $\text{La}_{1-x}\text{Ca}_x\text{MnO}_3$ and $\text{YBa}_2\text{Cu}_3\text{O}_{7-\delta}$ thin films,” *Applied Physics Letters*, vol. 81, no. 21, pp. 4026–4028, 2002.
- [13] P. X. Zhang, C. Wang, G. Y. Zhang, L. Yu, W. K. Lee, and H.-U. Habermeier, “ LaCaMnO_3 thin film laser energy/power meter,” *Optics and Laser Technology*, vol. 36, no. 4, pp. 341–343, 2004.
- [14] Th. Zahner, R. Stierstorfer, S. Reindl, T. Schauer, A. Penzkofer, and H. Lengfellner, “Picosecond thermoelectric response of thin $\text{YBa}_2\text{Cu}_3\text{O}_{7-\delta}$ films,” *Physica C*, vol. 313, no. 1-2, pp. 37–40, 1999.
- [15] H.-U. Habermeier, X. H. Li, P. X. Zhang, and B. Leibold, “Anisotropy of thermoelectric properties in $\text{La}_{2/3}\text{Ca}_{1/3}\text{MnO}_3$ thin films studied by laser-induced transient voltages,” *Solid State Communications*, vol. 110, no. 9, pp. 473–478, 1999.
- [16] X. H. Li, H.-U. Habermeier, and P. X. Zhang, “Laser-induced off-diagonal thermoelectric voltage in $\text{La}_{1-x}\text{Ca}_x\text{MnO}_3$ thin films,” *Journal of Magnetism and Magnetic Materials*, vol. 211, no. 1, pp. 232–237, 2000.
- [17] C. Wang, P. X. Zhang, and G. Y. Zhang, “Optimum thickness for laser induced thermoelectric voltage effect in high T-c superconductor and CMR thin film,” *Acta Physica Sinica*, vol. 53, no. 6, pp. 1727–1730, 2004.
- [18] P. X. Zhang, G. Y. Zhang, H. J. Wu, et al., “Time constant of laser-induced thermoelectric voltage device made by LaCaMnO_3 , $\text{YBa}_2\text{Cu}_3\text{O}_{7-\sigma}$ and LaSrCoO_3 thin films,” *Transactions of the Materials Research Society of Japan*, vol. 29, no. 4, pp. 1423–1426, 2004.
- [19] G.-Y. Zhang, P. X. Zhang, H. Zhang, and W. K. Lee, “Figure of merit for detectors based on laser-induced thermoelectric voltages in $\text{La}_{1-x}\text{Ca}_x\text{MnO}_3$ and $\text{YBa}_2\text{Cu}_3\text{O}_{7-\delta}$ thin films,” *Chinese Physics Letters*, vol. 22, no. 9, pp. 2379–2381, 2005.
- [20] W.-D. Cui, H. Zhang, G.-Y. Zhang, J.-T. Hu, Y.-N. Dai, and P.-X. Zhang, “Laser induced thermoelectric voltage of atomic layer thermopile materials,” *Chinese Journal of Lasers*, vol. 34, no. 1, pp. 130–134, 2007.
- [21] N. F. Mott and E. A. Davis, *Electronic Processes in Non-crystalline Materials*, Oxford University Press, Oxford, UK, 1979.
- [22] Y. L. Yang, *Preparation and LITV effect of LaSrCaMnO_3 thin films*, M.S. thesis, Kunming Institute of Science and Technology, Kunming, China, 2005.
- [23] J. L. Wang, *Conductive LaSrCoO_3 thin film and laser induced voltage properties*, M.S. thesis, Kunming Institute of Science and Technology, Kunming, China, 2005.
- [24] Y. Yuan, H. Zhang, T. S. Tan, and P.X. Zhang, “Growth and laser induced thermoelectric voltage effect of the c-axis oriented $\text{Ca}_3\text{Co}_4\text{O}_9$ thin film on sapphire substrates,” *Chinese Journal of Lasers*, vol. 35, p. 921, 2008.
- [25] L. L. Xie, H. Zhang, and P. X. Zhang, “Preparation and LITV effect in $\text{YBaCuO}_{7-\delta}\text{LaPbMnO}_3$ Multilayer,” *Journal of Low Temperature Physics*, vol. 29, p. 109, 2007.
- [26] M. V. Simkin and G. D. Mahan, “Minimum thermal conductivity of superlattices,” *Physical Review Letters*, vol. 84, no. 5, pp. 927–930, 2000.
- [27] R. Venkatasubramanian, E. Siivola, T. Colpitts, and B. O’Quinn, “Thin-film thermoelectric devices with high room-temperature figures of merit,” *Nature*, vol. 413, no. 6856, pp. 597–602, 2001.
- [28] T. C. Harman, P. J. Taylor, M. P. Walsh, and B. E. LaForge, “Quantum dot superlattice thermoelectric materials and devices,” *Science*, vol. 297, no. 5590, pp. 2229–2232, 2002.
- [29] R. Venkatasubramanian, “Lattice thermal conductivity reduction and phonon localizationlike behavior in superlattice structures,” *Physical Review B*, vol. 61, no. 4, pp. 3091–3097, 2000.
- [30] L. D. Hicks and M. S. Dresselhaus, “Effect of quantum-well structures on the thermoelectric figure of merit,” *Physical Review B*, vol. 47, no. 19, pp. 12727–12731, 1993.
- [31] M. Matsukawa, M. Narita, T. Nishimura, et al., “Anisotropic phonon conduction and lattice distortions in colossal-magnetoresistance bilayer manganite $(\text{La}_{1-z}\text{Pr}_z)_{1.2}\text{Sr}_{1.8}\text{Mn}_2\text{O}_7$ ($z = 0, 0.2, 0.4, \text{ and } 0.6$) single crystals,” *Physical Review B*, vol. 67, no. 10, Article ID 104433, 6 pages, 2003.
- [32] Z. H. He, Z. G. Ma, Q. Y. Li, et al., “Investigation of transverse Peltier effect on top-seeded melt texture $\text{YBa}_2\text{Cu}_3\text{O}_{7-\delta}$,” *Applied Physics Letters*, vol. 69, no. 23, pp. 3587–3589, 1996.
- [33] A. Kyarad and H. Lengfellner, “Transverse Peltier effect in tilted $\text{Pb-Bi}_2\text{Te}_3$ multilayer structures,” *Applied Physics Letters*, vol. 89, no. 19, Article ID 192103, 3 pages, 2006.
- [34] K. H. Ahn, T. Lookman, and A. R. Bishop, “Strain-induced metal-insulator phase coexistence in perovskite manganites,” *Nature*, vol. 428, no. 6981, pp. 401–404, 2004.
- [35] A. J. Millis, “Lattice effects in magnetoresistive manganese perovskites,” *Nature*, vol. 392, no. 6672, pp. 147–150, 1998.
- [36] Z.-H. Wang, G. Cristiani, and H.-U. Habermeier, “Uniaxial magnetic anisotropy and magnetic switching in $\text{La}_{0.67}\text{Sr}_{0.33}\text{MnO}_3$ thin films grown on vicinal $\text{SrTiO}_3(100)$,” *Applied Physics Letters*, vol. 82, no. 21, pp. 3731–3733, 2003.
- [37] M. Jaime, P. Lin, S. H. Chun, M. B. Salamon, P. Dorsey, and M. Rubinstein, “Coexistence of localized and itinerant carriers near T_C in calcium-doped manganites,” *Physical Review B*, vol. 60, no. 2, pp. 1028–1032, 1999.
- [38] S. Uhlenbruck, B. Büchner, R. Gross, A. Freimuth, A. Maria de Leon Guevara, and A. Revcolevschi, “Thermopower and anomalous heat transport in $\text{La}_{0.85}\text{Sr}_{0.15}\text{MnO}_3$,” *Physical Review B*, vol. 57, no. 10, pp. R5571–R5574, 1998.
- [39] G. Venkataiah, Y. K. Lakshmi, and P. V. Reddy, “Thermopower studies of $\text{Pr}_{0.67}\text{D}_{0.33}\text{MnO}_3$ manganite system,” *Journal of Physics D*, vol. 40, no. 3, pp. 721–729, 2007.
- [40] M. Battabyal and T. K. Dey, “Seebeck coefficient in polycrystalline $\text{La}_{0.7}\text{Sr}_{0.3-x}\text{Ag}_x\text{MnO}_3$ pellets: analysis in terms of a phase separation model,” *Journal of Physics: Condensed Matter*, vol. 18, no. 2, pp. 493–505, 2006.
- [41] E. Dagotto, “Open questions in CMR manganites, relevance of clustered states and analogies with other compounds including the cuprates,” *New Journal of Physics*, vol. 7, no. 1, pp. 67–95, 2005.
- [42] Y. Tomioka and Y. Tokura, “Global phase diagram of perovskite manganites in the plane of quenched disorder versus one-electron bandwidth,” *Physical Review B*, vol. 70, no. 1, Article ID 014432, 5 pages, 2004.
- [43] Ch. Renner, G. Aeppli, B.-G. Kim, Y.-A. Soh, and S.-W. Cheong, “Atomic-scale images of charge ordering in a mixed-valence manganite,” *Nature*, vol. 416, no. 6880, pp. 518–521, 2002.

Research Article

The Role of Filler-Matrix Interaction on Viscoelastic Response of Biomimetic Nanocomposite Hydrogels

Alireza S. Sarvestani, Xuezhong He, and Esmail Jabbari

Biomimetic Materials and Tissue Engineering Laboratories, Department of Chemical Engineering, University of South Carolina, Columbia, SC 29208, USA

Correspondence should be addressed to Esmail Jabbari, jabbari@engr.sc.edu

Received 19 September 2007; Accepted 2 May 2008

Recommended by Hongchen Gu

The effect of a glutamic acid (negatively charged) peptide (Glu6), which mimics the terminal region of the osteonectin glycoprotein of bone on the shear modulus of a synthetic hydrogel/apatite nanocomposite, was investigated. One end of the synthesized peptide was functionalized with an acrylate group (Ac-Glu6) to covalently attach the peptide to the hydrogel phase of the composite matrix. The addition of Ac-Glu6 to hydroxyapatite (HA) nanoparticles (50 nm in size) resulted in significant reinforcement of the shear modulus of the nanocomposite (~100% increase in elastic shear modulus). The reinforcement effect of the Glu6 peptide, a sequence in the terminal region of osteonectin, was modulated by the size of the apatite crystals. A molecular model is also proposed to demonstrate the role of polymer-apatite interaction in improving the viscoelastic behavior of the bone mimetic composite. The predictions of the model were compared with the measured dynamic shear modulus of the PLEOF hydrogel reinforced with HA nanoparticles. This predictive model provides a quantitative framework to optimize the properties of reinforced polymer nanocomposites as scaffolds for applications in tissue regeneration.

Copyright © 2008 Alireza S. Sarvestani et al. This is an open access article distributed under the Creative Commons Attribution License, which permits unrestricted use, distribution, and reproduction in any medium, provided the original work is properly cited.

1. INTRODUCTION

Synthetic degradable and biomimetic polymer nanocomposites are an ideal replacement material for orthopedics and dental applications because of minimum risk of disease transfer, reduced stress shielding and particulate wear, and the ability to couple polymer degradation with tissue regeneration. In particular, injectable hydrogels seeded with cells and growth factors and coupled with minimally invasive arthroscopic techniques are an attractive alternative for treating irregularly shaped degenerated hard tissues. Marrow stromal cells, isolated from the bone marrow, and growth factors can be placed in a supportive hydrogel and injected into an osteochondral defect by a minimally invasive arthroscopic procedure [1–5].

After injection, the composite mixture hardens in situ, guiding the development of the seeded cells into the desired tissue. Furthermore, the composite matrix provides dimensional stability and mechanical strength, similar to that of the host tissue, during regeneration. A variety of

multifunctional composite materials have been developed to mimic the organized nanostructure of the bone, which consists of the collagenous matrix and mineralized apatite nanocrystals [6–8]. In addition, the gelatinous bone matrix contains noncollagenous proteins (NCPs), which play a central role in regulation of mineralization and the extent of mineral-collagen interactions [9, 10]. One of the NCPs with bone specific functions is osteonectin which has a strong affinity for both collagen and hydroxyapatite (HA), and it is speculated to be a bone-specific nucleator of mineralization [11, 12]. It is believed that the first seventeen NH₂-terminal amino acids of osteonectin are responsible for binding to the bone collagen network [13], while a glutamic acid-rich sequence binds to the bone HA nanoparticles, due to its high ionic affinity for calcium ions [12].

In this work, we describe the synthesis and rheological characterization of a multifunctional bone mimetic nanocomposite with a matrix-apatite adhesion mechanism similar to that of the natural bone. We have synthesized a glutamic acid-rich peptide (a sequence of 6 glutamic acids)

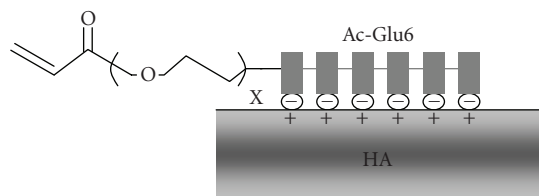


FIGURE 1: Schematic structure of the Ac-Glu6 peptide used for surface treating of HA nanoparticle. Terminal acrylate group of the Ac-Glu6 provides an unsaturated group for covalent cross-linking of the apatite particles to the PLEOF matrix.

derived from osteonectin, functionalized with an acrylate group for covalent attachment to the matrix, using solid-phase Fmoc chemistry [14]. The biodegradable in situ cross-linkable poly (lactide-co-ethylene oxide fumarate) (PLEOF) hydrogel and HA crystals were used to mimic the gelatinous matrix and mineral phases of the bone, respectively. PLEOF is a degradable macromer consisting of ultra-low-molecular-weight poly (L-lactide) (ULMW PLA) and poly (ethylene glycol) (PEG) blocks linked by fumaric acid. HA particles were treated with the synthesized glutamic acid peptide with acrylate group at one chain-end (Figure 1), hereafter designated as Ac-Glu6, and the nanoparticles were dispersed in the aqueous PLEOF mixture by sonication. The polymerizing mixture was cross-linked with a neutral redox initiation system and the gelation process was monitored by monitoring the viscoelastic response in situ as a function of gelation time with a rheometer. The measured rheological and viscoelastic characteristics can be used to control the injectability in the in situ hardening phase and to predict mechanical properties in the postgelation phase.

The rheometry results show that the Ac-Glu6 peptide can significantly enhance the viscoelastic properties of the hydrogel/HA nanocomposite. A molecular model is also proposed to demonstrate the role of polymer-apatite interaction in improving the viscoelastic behavior of the synthesized bone mimetic hydrogel. The scaling law of de Gennes for equilibrium reversible polymer adsorption in good solvent conditions [15] is used to predict the equilibrium configuration of the adsorbed polymer layer on the surface of HA particles. The relaxation and diffusion of the adsorbed segments, and consequently their flow characteristics, are predicted using a Maxwell type kinetic model. Predictions of the model are compared with the measured dynamic shear modulus of the PLEOF hydrogel reinforced with HA nanoparticles. This predictive model can provide a quantitative framework to design and optimize the properties of reinforced polymer composites as scaffolds for applications in tissue regeneration.

2. EXPERIMENTAL METHODS

2.1. Synthesis of PLEOF

PLEOF was synthesized by condensation polymerization of ULMW PLA [16] and PEG with fumaryl chloride (FuCl), as shown in Figure 2. The procedure for synthesis is described

in a previous publication [16]. The weight ratio of PLA to PEG was 30/70 to produce a hydrophilic PLEOF macromer. The structure of the macromer was characterized by $^1\text{H-NMR}$ and GPC. The synthesized PLEOF had M_n and PI values of 10.5 kDa and 1.7, respectively, as determined by GPC.

2.2. Synthesis of Ac-Glu6 peptide

The functionalized Ac-Glu6 peptide, a negatively charged Glu-Glu-Glu-Glu-Glu-Glu peptide sequence with an acrylate group at one chain-end (Figure 1), was synthesized manually in the solid phase on the Rink Amide NovaGel resin [14]. Briefly, the Fmoc-protected amino acids were coupled to the resin in N,N -dimethylformamide using N,N' -diisopropylcarbodiimide and N,N -dimethylaminopyridine as the coupling agents. After coupling the last amino acid, the Fmoc-protecting group of the last glutamine residue was selectively deprotected with piperidine. One end was acrylated directly on the peptidyl resin by coupling acrylic acid to the amine group of the last glutamine residue in the peptide sequence. The resin was treated with 95% TFA/2.5% TIPS/2.5% water for 2 hours to cleave the peptide from the resin. The solution was precipitated in ether, the solid was purified by preparative HPLC (Waters, Milford, Mass, USA), and the product was freeze-dried. The product was characterized by mass spectrometry with a Finnigan 4500 spectrometer [14]. A similar procedure was used to synthesize the neutral Gly-Gly-Gly-Gly-Gly-Gly (Gly6) peptide and positively-charged Lys-Lys-Lys-Lys-Lys-Lys (Lys6) peptide sequences with an acrylate group at one chain-end (Ac-Gly6 and Ac-Lys6, resp.).

2.3. Preparation of the hydrogel nanocomposite

100 mg Ac-Glu6 peptide ($M_n = 900$ Da) was dissolved in 0.825 mL of distilled deionized (DDI) water by vortexing and heating the mixture to 50°C . HA filler (Berkeley Advanced Biomaterials, Berkeley, Calif, USA) with average size of 50 nm (measured by TEM), with volume fraction ranging from 3 to 9% ($\rho_{\text{HA}} = 3.16 \text{ g/cm}^3$) was added to the PLEOF polymerizing mixture and the resulting dispersion was sonicated for 5 minutes. Larger spherical particles, with average diameter of $5 \mu\text{m}$, were also used to investigate the effect of particle size. The composite mixture was prepared by dispersing the HA/Ac-Glu6 in PLEOF macromer (0.04 M) and methylene bisacrylamide cross-linker (0.25 M). The neutral redox initiation system with equimolar concentrations (0.03 M) of ammonium persulfate and tetramethylethylenediamine was used to maintain the pH of the polymerizing mixture constant at 7.4.

2.4. Rheological measurements

The composite mixture was injected on the Peltier plate of the rheometer for rheological and gelation measurements. The dynamic storage modulus (G') was measured at 37°C by a TA instrument AR2000 rheometer equipped with a parallel plate geometry (diameter = 20 mm). A sinusoidal

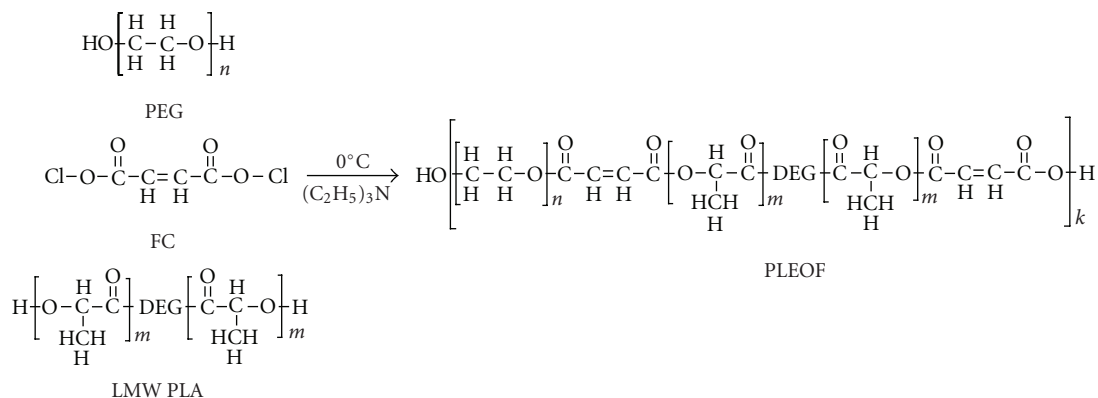


FIGURE 2: Schematic structure of the PLEOF macromer. DEG in the structure of PLEOF is diethylene glycol used as initiator in the synthesis of ULMW PLA by ring-opening polymerization of L-lactide monomer.

shear strain profile was exerted on the sample via the upper plate. The time sweep oscillatory shear measurements were done at constant frequency of 1 Hz and deformation amplitude equal to 1% for 3 hours. Each measurement was immediately followed by an amplitude sweep in the range increasing from 0.1% to 10% strain at frequency of 1 Hz. To reduce the effect of particle aggregates disruption on the high strain nonlinear response of the composite, each amplitude sweep measurement was repeated with 30 minutes relaxation between the two runs and the results of the second run are reported here. Measurement for the third time revealed no difference between the last two measurements.

3. EXPERIMENTAL RESULTS

Figure 3 shows the variation of the normalized storage modulus of the hydrogel composites (recorded at the end of time sweep measurements) as a function of particle concentration for different particle size and surface treatment. Nanoapatite composites (treated and untreated) displayed far larger stiffness compared with microcomposites, at the same volume fraction. Shear modulus of the nanocomposites with Ac-Glu6 linker was higher than those without the apatite linker. The modulus of the composites with micron size particles did not appreciably change with the addition of Ac-Glu6. The contribution of hydrodynamic effect to the modulus of the composites can be predicted by Guth-Smallwood equation [17], $G'_0(\Phi) = G'_0(0)(1 + 2.5\Phi)$, where $G'_0(0)$ and $G'_0(\Phi)$ are the storage modulus of the gel and composite, respectively, and Φ is the filler volume fraction. The storage modulus of the composites prepared with micron size particles can be reasonably predicted by Guth-Smallwood equation, as shown in Figure 3. However, the large difference between the experimental results and prediction of Guth-Smallwood equation for composites prepared with nanosize HA implies that the reinforcement cannot be explained solely by hydrodynamic effects in nanoparticulate systems.

To provide further evidence for energetic affinity between the Ac-Glu6 peptide and HA and its effect on the shear modulus of the nanocomposites, similar measurements were

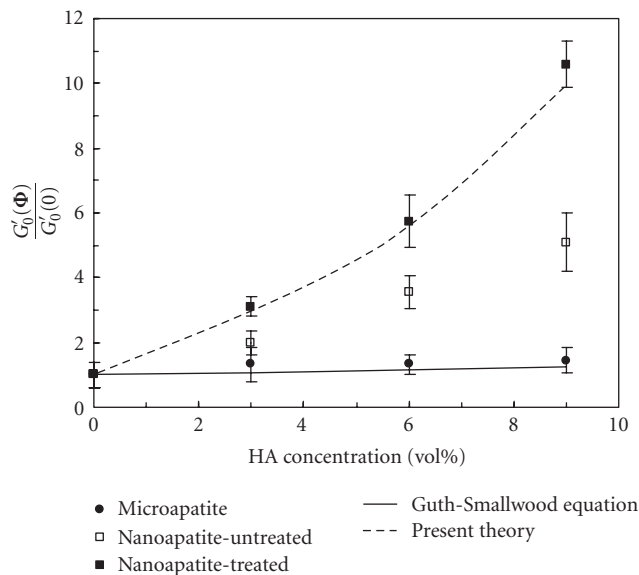


FIGURE 3: Dependence of the shear modulus of PLEOF/HA hydrogel composites on the size of the dispersed apatite particles. The normalized low-amplitude shear modulus predicted by the presented theory (dashed line) and Guth-Smallwood equation (solid line) are also compared with experimental data.

performed on the PLEOF/HA composites treated with equal molar concentrations of Ac-Gly6 and Ac-Lys6 in place of Ac-Glu6. Contrary to Glu6 peptide, Gly6 and Lys6 are neutral and positively charged, respectively. HA/Ac-Gly6 and HA/Ac-Lys6 nanocomposites with 9 vol% apatite did not show a significant change in storage shear modulus compared to that without HA surface treatment, as shown in Figure 4. The Ac-Lys6 is a positively charged sequence and it is expected to interact with the phosphate groups on the apatite surface in the same way that the negatively charged Ac-Glu6 sequence interacts with calcium ions, but the results in Figure 4 do not support this expectation. The charge ratio of Ca^{2+} to PO_4^{3-} groups in the HA crystal, with atomic composition $[\text{Ca}_{10}(\text{PO}_4)_6(\text{OH})_2]$, is greater than one and

to meet the requirement for electroneutrality, the negatively charged OH^- groups compensate for the imbalance [18]. Electronic structure and interatomic potential-based calculations show that the OH^- groups, in the bulk as well as the HA surface, are easily replaced by negatively charged fluoride ions [18]. Furthermore, phosphate and fluoride ions have been demonstrated to alter the mineral-organic interactions and influence the mechanical properties of the bone [19]. It is well established that certain small anionic molecules and polymers like poly (vinyl phosphonic acid) [20] and poly (acrylamide-*co*-acrylic acid) [21] displace negatively-charged hydroxyl groups (and in some cases phosphate groups) to interact and bond with calcium ions on the apatite surface. Based on these previous results, we believe that the Ac-Glu6 sequence ionically interacts with the apatite crystals by replacing the weakly bound hydroxyl groups (and perhaps the surface bound phosphate groups) from the surface but the same mode of interaction is not energetically favorable for Ac-Lys6, that is, Ac-Lys6 cannot replace the positively-charged surface calcium ions to interact with the apatite crystals. These results demonstrate that the increase in adsorption energy and its effect on the overall viscoelastic response of the nanocomposite are specific to the Ac-Glu6 peptide. The reinforcement is amplified as the size of the nanoparticles is reduced from $5\ \mu\text{m}$ to $50\ \text{nm}$, due to the higher surface area for ionic interactions provided by nanoapatite fillers. A molecular model is developed for the viscoelastic behavior of filled hydrogels which accounts for the effect of polymer/filler interaction energy. The model is used to predict the viscoelastic response of PLEOF/HA hydrogel nanocomposite.

4. THEORETICAL MODEL

The model is based on the theory of reversible adsorption from a dilute polymer solution [15, 22]. Adsorption of the polymer chains from solution on the solid surface takes place when the chains energetically prefer the surface over the solvent. The average residence time of each monomer on the solid surface is determined by the binding energy between the monomer and particle surface. It has been shown that when the contact energy per monomer is less than the thermal energy, $k_B T$, the adsorption process is reversible, that is, the adsorbed polymer chain detaches from the surface after a finite residence time and the bonding site are replaced with another polymer chain [22]. When the binding energy is somewhat larger than $k_B T$, the adsorption becomes irreversible, and the adsorbed chains flatten and freeze on the interactive surface [23].

4.1. Filler-gel interfacial structure

The equilibrium configuration of a chain segment (between two consecutive cross-link points), near the filler surface with radius, R_f , is schematically shown in Figure 5. The segment can reversibly adsorb on the colloidal surface and form a polydisperse succession of loops, tails, and sequences of bound monomers (trains). Each segment with

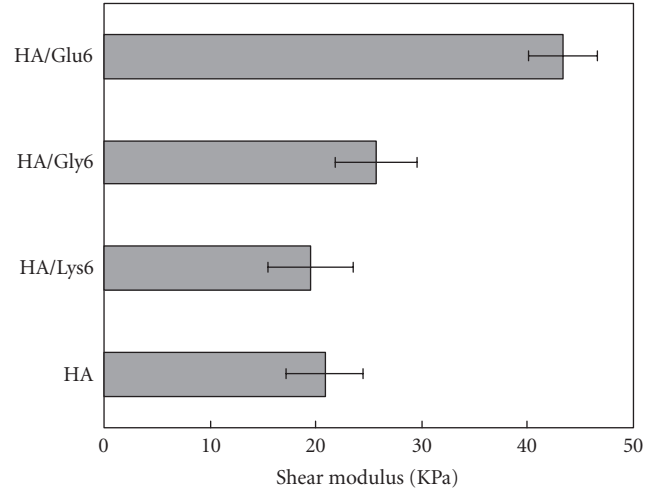


FIGURE 4: Comparison of the shear modulus of PLEOF/HA composites with 9 vol% untreated nanoparticles with nanoparticles treated with Ac-Glu6, Ac-Gly6, and Ac-Lys6.

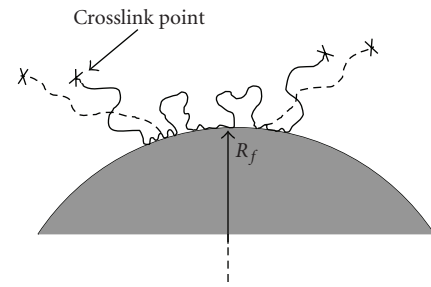


FIGURE 5: Schematic diagram of the equilibrium configuration of an adsorbed polymer segment (solid line) between two cross-link points on the filler surface. The adsorbed chain consists of loops, tails, and sequences of bonded monomers. The adsorbed segment can detach from the surface at a number of points after the application of deformation (dashed line).

N monomers of size a occupies a spherical volume with a radius comparable with the Flory radius, $R_F = a N^{3/5}$.

In order to describe the structure of the adsorbed and fully-equilibrated polymer layer on the filler surface, we used a modified version of de Gennes scaling theory [24] for reversible adsorption from dilute solutions under good solvent conditions. The chain configuration in an adsorbed layer is determined by the competition between excluded volume, surface energy, and chain entropic effects. Assuming that the loops are extended to an average thickness D from the surface, the fraction of monomers in direct contact with the particle surface can be approximated by $f \cong a/D$. Assuming that the conformational entropy and energetic affinity with the surface are the only factors that determine the configuration of the adsorbed layer, the free energy per segment, Ψ , can be written as [25]

$$\Psi \cong k_B T \left(\frac{R_F}{D} \right)^{5/3} - f N \Delta E_{\text{ad}}. \quad (1)$$

Minimizing the free energy with respect to D yields

$$f \cong \left(\frac{\Delta E_{\text{ad}}}{k_B T} \right)^{3/2}. \quad (2)$$

4.2. Dynamics of the adsorbed layer

The gel-particle energetic attraction is modeled as a frictional interaction between the adsorbed monomers and particle surface, in addition to the regular monomer-solvent and/or monomer-monomer frictions. Therefore, the total friction coefficient due to the hydrodynamic force acting on the i th monomer is [26]

$$\begin{aligned} (\xi)_i &= \xi_1, & i\text{th monomer is adsorbed,} \\ (\xi)_i &= \xi_0, & i\text{th monomer is not adsorbed,} \end{aligned} \quad (3)$$

where ξ_1 is the friction coefficient due to monomer-particle interaction and ξ_0 is the friction coefficient corresponding to the self-diffusion of a single monomer and it accounts for its friction with the solvent molecules and/or other non-adsorbed monomers. Using an Arrhenius-type activation model for a monomer of size a , the friction coefficient is approximated by $\xi_0 \cong k_B T \tau_0 / a^2$, with time constant τ_0 defined by

$$\tau_0 = \tau^* \exp\left(\frac{E_0}{k_B T}\right), \quad (4)$$

where τ^* is a constant. A similar activation model can be used to estimate $\xi_1 \cong k_B T \tau_1 / a^2$, where τ_1 is defined as

$$\tau_1 = \tau^* \exp\left(\frac{E_1}{k_B T}\right). \quad (5)$$

Here, $E_1 = \Delta E_{\text{ad}} + E_0$ is the energy required to detach the adsorbed monomer from the particle surface.

Since a fraction f of the monomers in an adsorbed segment is in contact with the particle surface, the total friction coefficient of the entire adsorbed segment is given by

$$\xi_a = N(f \xi_1 + (1-f)\xi_0), \quad (6)$$

where by using (4) and (5),

$$\xi_1 = \xi_0 \exp\left(\frac{\Delta E_{\text{ad}}}{k_B T}\right). \quad (7)$$

For weakly attractive surfaces, segments are partially adsorbed to the surface and exhibit their 3D Rouse dynamics [27]. Hence, the relaxation time of the adsorbed segment is

$$\tau_a \cong R_F^2 \frac{\xi_a}{k_B T} = \tau_f \left(f \exp\left(\frac{\Delta E_{\text{ad}}}{k_B T}\right) + (1-f) \right), \quad (8)$$

where $\tau_f \cong R_F^2 (\xi_f / k_B T)$ is the relaxation time of a free segment.

The self-similar grid structure [22] describes the adsorbed layer as a semi-dilute solution of the polymer with continuously varying local concentration of the monomers,

such that at any distance r from the surface, the local blob size is equal to r . Therefore, the equilibrium thickness of the layer is on the order of R_F . In a cross-linked system, due to the fixed-end constraint, segments cannot diffuse independently like linear chains. Hence, the adsorption-desorption process takes place between those segments which are located within the interphase region with thickness R_F around the fillers and with total population density equal to $N_f^p + N_a$. Here, N_a is the number density of the adsorbed segments and N_f^p represents the number density of free segments within the interphase zone, which are able to participate in the adsorption-desorption process. The rate of attachment can be shown by the following kinetic equation:

$$\frac{dN_a}{dt} = N_f^p (\tau_{\text{ads}})^{-1} - N_a (\tau_{\text{des}})^{-1}, \quad (9)$$

where τ_{ads} and τ_{des} are the characteristic times of adsorption and desorption of the segments, respectively.

The energy required for detachment of an adsorbed segment is equal to $fN\Delta E_{\text{ad}}$. In the presence of an applied macrodeformation, the tails of each segment move with the bulk material (Figure 5). The detachment process is thus favored by the resultant entropic tension exerted by the segment. Considering this effect, the time constants associated with the attachment and detachment of the segments follow the relation defined by

$$\tau_{\text{des}} = \tau_{\text{ads}} \exp\left[\frac{fN\Delta E_{\text{ad}} - \delta F_a}{k_B T}\right], \quad (10)$$

where F_a is the entropic force in the segment and δ is an activation length on the order of the displacement required to detach the bound segment from the particle surface. The desorption of a bound monomer with weak and short range interaction with the adsorbing surface can be considered as a local process. It takes place when the monomer diffuses a distance on the order of the equilibrium size of the first blob in contact with the wall [28]. According to the self-similar grid structure theory [22], the size of the first blob in contact with the particle surface is on the order of the size of a monomer. Therefore, δ , the total displacement required to separate the entire segment with f fraction of adsorbed monomers, is $a \leq \delta \leq R_F$.

4.3. Macroscopic properties

The classical Maxwell model [29] is used to describe the viscoelasticity of the matrix. It is assumed that the deformations are relatively small such that geometric nonlinearities can be neglected and only the thixotropic nonlinearities, due to polymer-filler interactions, are considered. At any instant in time, a representative segment is either adsorbed to the surface of the particle or it is free. Assuming that the configurations of free and adsorbed segments evolve independently, the total stress in the composite is therefore the sum of the stresses by the adsorbed (σ_a) and free (σ_f) segments, that is,

$$\sigma = \sigma_a + \sigma_f. \quad (11)$$

The contribution of the segments to the stress tensor is given by Kramers expression:

$$\begin{aligned}\sigma_a &= 3G_a \frac{\langle \mathbf{R}_a \mathbf{R}_a \rangle}{R_F^2}, \\ \sigma_f &= 3G_f \frac{\langle \mathbf{R}_f \mathbf{R}_f \rangle}{R_F^2},\end{aligned}\quad (12)$$

where G_a and G_f represent the stiffness of the adsorbed segments and free segments (located out of the interphase zone), respectively. \mathbf{R}_i ($i = a, f$) is the segment end-to-end vector and $\langle \cdot \cdot \cdot \rangle$ shows the ensemble average. According to the classical theory of rubber elasticity [30], a linear dependency is introduced between the modulus and number density of the chains at constant temperature, that is, $G_i \propto N_i$ ($i = a, f$). Therefore, at steady-state conditions, we have

$$G_a = G_f^p \exp \left[\frac{fN\Delta E_{ad} - \delta F_a}{k_B T} \right], \quad (13)$$

where G_f^p shows the stiffness of the free segments within the interphase zone.

The mechanical response of the network can be decoupled into two parts: a rate independent response and a time dependent deviation from the equilibrium [31], that is,

$$\sigma_i = \sigma_i^e + \sigma_i^v, \quad i = a, f, \quad (14)$$

where σ_i^e and σ_i^v stand for the rate independent and rate dependent components of the stress, respectively. Using (12), the time independent component of stress can be expressed by

$$\sigma_i^e = G_i \mathbf{F} \cdot \mathbf{F}^T, \quad i = a, f, \quad (15)$$

where \mathbf{F} is the deformation gradient tensor.

In their simplest form, the constitutive relations for the evolution of the rate dependent stresses produced by the segments can be expressed by the Maxwell (upper-convected) equations [29]:

$$\begin{aligned}\tau_a \hat{\sigma}_a^v + \sigma_a^v - G_a \mathbf{I} &= 0, \\ \tau_f \hat{\sigma}_f^v + \sigma_f^v - G_f \mathbf{I} &= 0,\end{aligned}\quad (16)$$

where \mathbf{I} is the identity tensor. Here, $\hat{\sigma}$ designates the upper-convected derivative of the stress tensor given by $\hat{\sigma} = \partial \sigma / \partial t - \sigma \cdot \mathbf{L}_{ef} - \mathbf{L}_{ef}^T \cdot \sigma$, where $\mathbf{L}_{ef} = h(\phi) \nabla \mathbf{v}$ is the effective velocity gradient tensor and \mathbf{v} is the velocity field. Here, $h(\phi)$ accounts for the hydrodynamic interaction between the particles with volume fraction ϕ . This is based on a phenomenological consideration that the effective velocity gradient experienced by the polymer matrix is higher than the externally-applied velocity gradient, due to the rigidity of the filler particles. The contribution of the hydrodynamic effect is determined by the shape and volume fraction of the particles [32]. At low filler concentrations, it is represented by

$$h(\phi) = 1 + \zeta \phi, \quad (17)$$

where the prefactor parameter ζ accounts for the particle geometry.

4.4. Model predictions

The model is used to predict the effect of HA surface adsorption energy on the overall steady-state shear modulus of the PLEOF hydrogel composites. Assuming the material is under oscillatory shear strain with frequency ω , the dynamic strain can be stated as

$$\lambda(t) = \lambda_0 \sin \omega t. \quad (18)$$

For simplicity, only the affine (time independent) part of the deformation is considered for evaluation of the entropic force in (13). For oscillatory shear loading with small strain λ_0 , the deformation gradient can be written as

$$\mathbf{F} = \begin{pmatrix} 1 & \lambda_0 \sin \omega t & 0 \\ 0 & 1 & 0 \\ 0 & 0 & 1 \end{pmatrix}. \quad (19)$$

The average end-to-end vector of an adsorbed segment during a period of oscillation can be obtained by

$$\bar{\mathbf{R}}_a = \bar{\mathbf{F}} \cdot \mathbf{R}_F, \quad (20)$$

where the components of $\bar{\mathbf{F}}$ are the average of the absolute values of the corresponding components in \mathbf{F} over one period of oscillation. The mean square end-to-end distance, given by (20), was used in $F_a = (3 k_B T / R_F^2) \bar{R}_a (1 - \bar{R}_a^2 / R_{a,\max}^2)^{-1}$ the Warner approximation for the entropic force, to calculate the average entropic tension in an adsorbed segment.

$R_{a,\max} / R_F$, $c = \Delta E_{ad} / k_B T$, and δ / R_F are the model parameters which represent the characteristic length of the polymer segments near the particle surface and the interaction energy between the PLEOF segments and HA nanoparticles. These parameters are independent of the filler concentration. G_f^p / G_f is another fitting parameter which is proportional to the volume fraction of interphase zone and number of those free chains, located in the interphase zone, contributing to the adsorption-desorption kinetics. Therefore, this parameter changes with the size and concentration of nanoparticles. The magnitude of the shear modulus in the low strain region is found to be sensitive to the values of c , while the onset of nonlinearity in the viscoelastic response is controlled by δ and $R_{a,\max}$.

The Flory radius of the segments between two consecutive fumarate units in the PLEOF (i.e., potential cross-link points) is estimated to be approximately 10 nm. The hydrodynamic factor ζ is set equal to 2.5 considering the spherical shape of HA nanoparticles. The best fit of the experimental results to the model was obtained with $G_f \cong 4$ kPa and $\tau_f = 0.001$ second for the free segments. Other extracted fitting parameters are listed in Table 1. The value of c for the surface-treated samples was found to be higher than that of untreated samples, due to the stronger average monomer-filler interaction in the presence of Ac-Glu6 peptide.

Figure 3 also represents the predicted values of small strain shear modulus of the Ac-Glu6 treated nanocomposites at different volume fraction of nanoapatite particles. Fitting the model parameters with measured storage modulus of

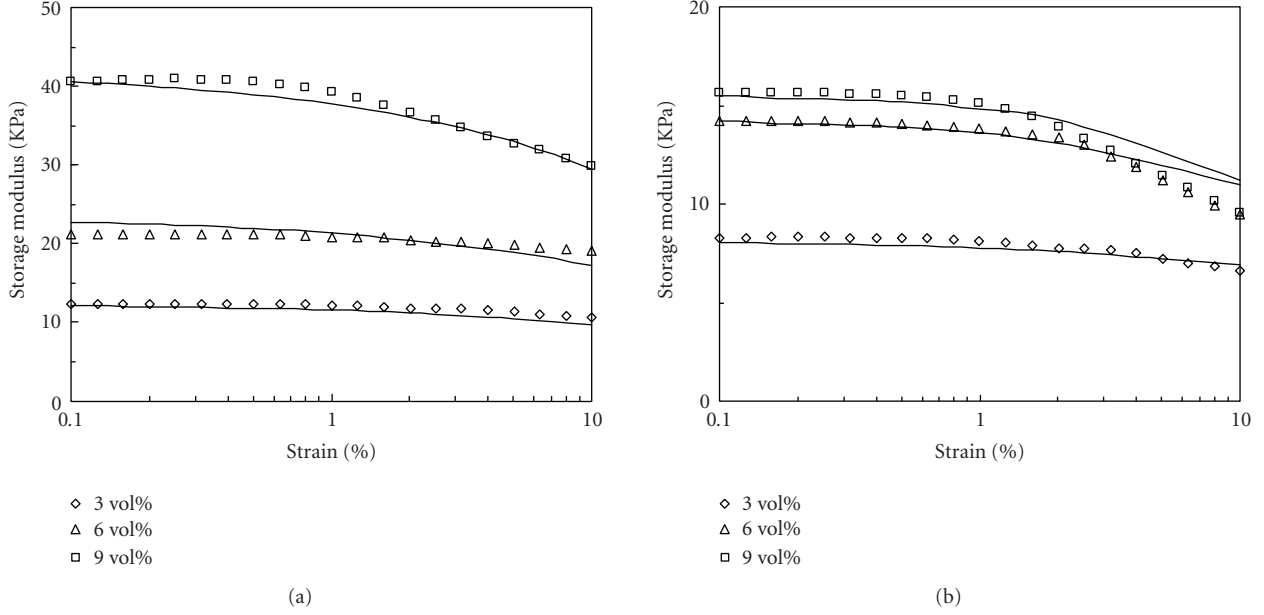


FIGURE 6: Comparison of the experimental results with model predictions (solid lines) for the storage modulus of PLEOF/HA composites, prepared with 3–9 vol% of (a) treated and (b) untreated nanoparticles as a function of strain amplitude (frequency = 1 Hz).

TABLE 1: Fitted parameters of the proposed model for the hydrogel/nanoparticle composites.

Parameters independent from filler concentration		
$\delta/R_F = 0.5, R_{a,max}/R_F = 1.5$	Treated $c = 0.02$	Untreated $c = 0.012$
Parameters variable with filler concentration		
ϕ	Treated G_f^p/G_f	Untreated G_f^p/G_f
3 (vol%)	0.25	0.33
6 (vol%)	0.53	0.75
9 (vol%)	0.93	0.76

microapatite composites results in a negligible value for G_f^p/G_f , and consequently the model prediction is fairly close to $h(\phi) G_f$, that is, the Guth–Smallwood equation. Hence, for large HA particles, relative to the length of the interacting segment, the reinforcement is dominated by hydrodynamic effects. It should be mentioned that due to constant thickness of interphase zone ($\sim R_F$), reduction of the filler size increases the volume fraction of the interphase zone in the matrix. As a result, the values of G_a and G_f^p and consequently the overall shear modulus of the composite increase.

The model results and experimental values for the shear storage modulus of surface treated and untreated composites are shown in Figure 6 as a function of strain amplitude. The model predictions qualitatively follow the trends in the experimentally-measured values; however, there are discrepancies, especially between the model results and experimental data of untreated samples.

The higher adsorption energy between PLEOF segments and HA nanoparticles in Glu6-treated samples (indicated by parameter $c = \Delta E_{ad}/k_B T$ in Table 1) can be attributed to the strong ionic bond with high adsorption energy between the negatively-charged glutamic acid sequences and the calcium ions on the surface of HA particles, compared to the weaker polar interactions in the absence of Ac-Glu6. The exponential dependence of G_a on adsorption energy, as shown by (13), implies that increasing the polymer-surface interaction energy leads to a significant enhancement in linear viscoelastic properties of the polymer composites. On the other hand, lower modulus of the untreated samples indicates weaker polymer-filler interfacial bonds in those samples which may give rise to stronger tendency for HA particles to aggregate, as a result of interparticle electrostatic or van der Waals' interactions [33]. The network of locally aggregated particles follows a different kinetic and relaxation pattern rooted in the stored elastic energy in the strained clusters and the failure properties of filler-filler bonds [34]. This mechanism, which is not accounted in the proposed model, can be considered as the major source of discrepancy between the experimental data of untreated samples and the model predictions.

5. CONCLUSIONS

The viscoelastic properties of a multifunctional bone mimetic nanocomposite with a matrix-apatite adhesion mechanism similar to that of the natural bone were investigated. A glutamic acid-rich peptide (a sequence of 6 glutamic acids), derived from osteonectin, was functionalized with an acrylate group (Ac-Glu) for covalent attachment to the matrix. The biodegradable in situ cross-linkable poly

(lactide-co-ethylene oxide fumarate) (PLEOF) hydrogel and HA crystals were used to mimic the gelatinous matrix and mineral phases of the bone, respectively. HA particles were treated with Ac-Glu6 and dispersed in the aqueous PLEOF mixture. The polymerizing mixture was cross-linked with a neutral redox initiation system and the gelation process was monitored in situ as a function of time with a rheometer. The rheometry results showed that the Ac-Glu6 peptide significantly enhanced the viscoelastic properties of the hydrogel/HA nanocomposite. A molecular model was developed to predict the role of polymer-apatite interaction in improving the viscoelastic behavior of the synthesized bone mimetic hydrogel nanocomposite. The scaling law of de Gennes for equilibrium reversible polymer adsorption in good solvent conditions was used to predict the equilibrium configuration of the adsorbed polymer layer on the surface of HA particles. The relaxation and diffusion of the adsorbed segments were predicted using a Maxwell type kinetic model. Predictions of the model are compared with the measured dynamic shear modulus of the PLEOF hydrogel reinforced with HA nanoparticles. The measured rheological and viscoelastic characteristics and the predictions of the model can be used to control injectability, in the in situ hardening phase, and to predict mechanical properties in the postgelation phase for composite scaffolds used in skeletal tissue regeneration.

ACKNOWLEDGMENT

This work was supported by grants from the Arbeitsgemeinschaft Fur Osteosynthesefragen (AO) Foundation (AORF Project 05-J95) and the Aircast Foundation.

REFERENCES

- [1] N. A. Peppas and R. Langer, "New challenges in biomaterials," *Science*, vol. 263, no. 5154, pp. 1715–1720, 1994.
- [2] D. C. Tancred, B. A. O. McCormack, and A. J. Carr, "A synthetic bone implant macroscopically identical to cancellous bone," *Biomaterials*, vol. 19, no. 24, pp. 2303–2311, 1998.
- [3] L. Hangody, G. Kish, Z. Kárpáti, I. Udvarhelyi, I. Szigeti, and M. Bély, "Mosaicplasty for the treatment of articular cartilage defects: application in clinical practice," *Orthopedics*, vol. 21, no. 7, pp. 751–756, 1998.
- [4] J. S. Temenoff and A. G. Mikos, "Injectable biodegradable materials for orthopaedic tissue engineering," *Biomaterials*, vol. 21, no. 23, pp. 2405–2412, 2000.
- [5] S. S. Liao, F. Z. Cui, W. Zhang, and Q. L. Feng, "Hierarchically biomimetic bone scaffold materials: nano-HA/collagen/PLA composite," *Journal of Biomedical Materials Research. Part B*, vol. 69, no. 2, pp. 158–165, 2004.
- [6] K. E. Tanner, R. N. Downes, and W. Bonfield, "Clinical applications of hydroxyapatite reinforced materials," *British Ceramic Transactions*, vol. 93, no. 3, pp. 104–107, 1994.
- [7] A. L. Boskey, "Will biomimetics provide new answers for old problems of calcified tissues?" *Calcified Tissue International*, vol. 63, no. 3, pp. 179–182, 1998.
- [8] J. E. Zerwekh, S. Kourosh, R. Scheinberg, et al., "Fibrillar collagen-biphasic calcium phosphate composite as a bone graft substitute for spinal fusion," *Journal of Orthopaedic Research*, vol. 10, no. 4, pp. 562–572, 1992.
- [9] J. A. Buckwalter, M. J. Glimcher, R. R. Cooper, and R. Recker, "Bone biology. Part II: formation form, modeling, remodeling, and regulation of cell function," *Journal of Bone and Joint Surgery*, vol. 77, no. 8, pp. 1276–1289, 1995.
- [10] V. I. Sikavitsas, J. S. Temenoff, and A. G. Mikos, "Biomaterials and bone mechanotransduction," *Biomaterials*, vol. 22, no. 19, pp. 2581–2593, 2001.
- [11] M. F. Young, "Bone matrix proteins: their function, regulation, and relationship to osteoporosis," *Osteoporosis International*, vol. 14, supplement 3, pp. S35–S42, 2003.
- [12] R. Fujisawa, Y. Wada, Y. Nodasaka, and Y. Kuboki, "Acidic amino acid-rich sequences as binding sites of osteonectin to hydroxyapatite crystals," *Biochimica et Biophysica Acta*, vol. 1292, no. 1, pp. 53–60, 1996.
- [13] R.-L. Xie and G. L. Long, "Elements within the first 17 amino acids of human osteonectin are responsible for binding to type V collagen," *Journal of Biological Chemistry*, vol. 271, no. 14, pp. 8121–8125, 1996.
- [14] X. He and E. Jabbari, "Solid-phase synthesis of reactive peptide crosslinker by selective deprotection," *Protein and Peptide Letters*, vol. 13, no. 7, pp. 715–718, 2006.
- [15] P. G. de Gennes, "Polymers at an interface: a simplified view," *Advances in Colloid and Interface Science*, vol. 27, no. 3-4, pp. 189–209, 1987.
- [16] A. S. Sarvestani, X. He, and E. Jabbari, "Viscoelastic characterization and modeling of gelation kinetics of injectable in situ cross-linkable poly(lactide-co-ethylene oxide-co-fumarate) hydrogels," *Biomacromolecules*, vol. 8, no. 2, pp. 406–415, 2007.
- [17] E. Guth, "Theory of filler reinforcement," *Journal of Applied Physics*, vol. 16, no. 1, pp. 20–25, 1945.
- [18] N. H. de Leeuw, "A computer modelling study of the uptake and segregation of fluoride ions at the hydrated hydroxyapatite (0001) surface: introducing a $\text{Ca}_{10}(\text{PO}_4)_6(\text{OH})_2$ potential model," *Physical Chemistry Chemical Physics*, vol. 6, no. 8, pp. 1860–1866, 2004.
- [19] W. R. Walsh and N. Guzelsu, "Compressive properties of cortical bone: mineral-organic interfacial bonding," *Biomaterials*, vol. 15, no. 2, pp. 137–145, 1994.
- [20] H. W. Choi, H. J. Lee, K. J. Kim, H.-M. Kim, and S. C. Lee, "Surface modification of hydroxyapatite nanocrystals by grafting polymers containing phosphonic acid groups," *Journal of Colloid and Interface Science*, vol. 304, no. 1, pp. 277–281, 2006.
- [21] E. I. F. Pearce, "Ion displacement following the adsorption of anionic macromolecules on hydroxyapatite," *Calcified Tissue International*, vol. 33, no. 4, pp. 395–402, 1981.
- [22] P. G. de Gennes, "Polymer solutions near an interface. 1. Adsorption and depletion layers," *Macromolecules*, vol. 14, no. 6, pp. 1637–1644, 1981.
- [23] B. O'Shaughnessy and D. Vavylonis, "Non-equilibrium in adsorbed polymer layers," *Journal of Physics: Condensed Matter*, vol. 17, no. 2, pp. R63–R99, 2005.
- [24] P.G. de Gennes, *Scaling Concepts in Polymer Physics*, Cornell University Press, Ithaca, NY, USA, 1985.
- [25] J. Gong and Y. Osada, "Gel friction: a model based on surface repulsion and adsorption," *Journal of Chemical Physics*, vol. 109, no. 18, pp. 8062–8068, 1998.
- [26] A. S. Sarvestani and C. R. Picu, "A frictional molecular model for the viscoelasticity of entangled polymer nanocomposites," *Rheologica Acta*, vol. 45, no. 2, pp. 132–141, 2005.
- [27] A. L. Ponomarev, T. D. Sewell, and C. J. Durning, "Surface diffusion and relaxation of partially adsorbed polymers," *Journal of Polymer Science*, vol. 38, no. 9, pp. 1146–1154, 2000.

-
- [28] J. Wittmer, A. Johner, J. F. Joanny, and K. Binder, "Chain desorption from a semidilute polymer brush: a Monte Carlo simulation," *The Journal of Chemical Physics*, vol. 101, no. 5, pp. 4379–4390, 1994.
- [29] G. Larson, *Constitutive Equations for Polymer Melts and Solutions*, Butterworths, Boston, Mass, USA, 1988.
- [30] J. D. Ferry, *Viscoelastic Properties of Polymers*, John Wiley & Sons, New York, NY, USA, 1980.
- [31] J. S. Bergström and M. C. Boyce, "Large strain time-dependent behavior of filled elastomers," *Mechanics of Materials*, vol. 32, no. 11, pp. 627–644, 2000.
- [32] G. Huber and T. A. Vilgis, "On the mechanism of hydrodynamic reinforcement in elastic composites," *Macromolecules*, vol. 35, no. 24, pp. 9204–9210, 2002.
- [33] A. S. Sarvestani and E. Jabbari, "Modeling and experimental investigation of rheological properties of injectable poly (lactide ethylene oxide fumarate)/hydroxyapatite nanocomposites," *Biomacromolecules*, vol. 7, no. 5, pp. 1573–1580, 2006.
- [34] G. Heinrich and M. Klüppel, "Recent advances in the theory of filler networking in elastomers," *Advances in Polymer Science*, vol. 160, pp. 1–44, 2002.

Research Article

Effect of Carbon Nanofiber-Matrix Adhesion on Polymeric Nanocomposite Properties—Part II

Khalid Lafdi, William Fox, Matthew Matzek, and Emel Yildiz

University of Dayton, 300 College Park, Dayton, OH 45469, USA

Received 22 March 2007; Accepted 5 July 2007

Recommended by Donglu Shi

A successful integration of two independent phases with good adhesion is imperative for effective translation of superior carbon nanofiber filler properties into a physically superior carbon nanocomposite. Carbon nanofibers were subjected to electrochemical oxidation in 0.1 M nitric acid for varying times. The strength of adhesion between the nanofiber and an epoxy matrix was characterized by flexural strength and modulus. The surface functional groups formed and their concentration of nanofibers showed a dependence on the degree of oxidation. The addition of chemical functional groups on the nanofiber surface allows them to physically and chemically adhere to the continuous resin matrix. The chemical interaction with the continuous epoxy matrix results in the creation of an interphase region. The ability to chemically and physically interact with the epoxy region is beneficial to the mechanical properties of a carbon nanocomposite. A tailored degree of surface functionalization was found to increase adhesion to the matrix and increase flexural modulus.

Copyright © 2008 Khalid Lafdi et al. This is an open access article distributed under the Creative Commons Attribution License, which permits unrestricted use, distribution, and reproduction in any medium, provided the original work is properly cited.

1. INTRODUCTION

Research on vapor-grown carbon nanofibers (VGCFs) has been heightened in recent years by the discovery of carbon nanotubes. Such fibers are characterized by an extraordinarily high tensile modulus, tensile strength, and high electrical and thermal conductivity. A decrease in the diameter of a vapor-grown carbon nanofiber causes gradual improvement in mechanical properties. As the fiber diameter reaches the threshold value of $1\ \mu\text{m}$, distinguishing the transition from a fiber to a nanofiber, the improvement in mechanical properties becomes more significant [1]. Vapor-grown carbon nanofibers can be prepared with diameters ranging from 15 nm to 100 nm. These fibers are not continuous and have hollow cores. Their morphology resembles that of carbon nanotubes. Nanofibers can have a number of different internal structures, wherein graphene layers are arranged as concentric cylinders, nested truncated cones, segmented structures, or stacked coins [2]. External morphologies include kinked and branched structures and diameter variation. The percolation threshold for carbon nanofibers is low indicating that only a small amount of nanofiber additive is required for conducting filler applications. The intrinsic stiffness and strength of carbon nanofibers, combined with these superior transport properties, present the opportunity to develop

multifunctional nanofiber composites with tailored physical and mechanical properties.

Experimental results from previously published research efforts indicate that VGCFs are suitable reinforcing agents for polymers. Lozano and Barrera demonstrated a 100% increase in the dynamic mechanical properties with 2 wt% VGCF in a polypropylene matrix [3]. Other work by Kuriger et al. with a higher loading of VGCFs in polypropylene produced over a 50% increase in tensile strength [4]. Patton et al. combined VGCFs with an epoxy and poly (phenylene sulfide) to improve the flexural properties of the matrix materials. They obtained 68 and 91% increases in the flexural strength in epoxy and poly (phenylene sulfide), respectively, with a nominal fiber loading of 20% by volume [5].

Fiber functionalization is considered necessary to improve mechanical properties in nanofiber-reinforced composites by increasing the stress transfer between the nanofiber and the matrix of a nanocomposite structure. Fiber-matrix adhesion is governed by the chemical and physical interactions at the interface. Extensive literature exists on surface treatment of conventional carbon fibers by methods such as oxidation in gas and liquid phases and anodic etching. Poor fiber-matrix adhesion may result in composite failure at the interface, resulting in decreased longitudinal and transverse mechanical properties of the composite.

Surface modification of carbon nanofibers changes the graphitization extent of the fiber and increases its surface area of the fiber. Lim et al. studied “stacked coin”-type nanofibers and the impact of mechanical and chemical treatments on the morphology of the fibers [6]. Heat treatment at 2800 °C induced closed loop ends on the surface of the nanofibers formed by folding of some planar hexagons at their edges. The heat treatment removed C–H bonds and densely stacked hexagonal layers of graphene, forming chemically active sites on the edges. The edges were stabilized by bonding to each other, even though the bonding caused high tension through the formation of a sharp curvature. Acidic oxidation of the nanofibers cuts off the closed looped ends, resulting in improved overall alignment of graphene layers. Both treatments generated many free edges and a high graphitization extent, indicating the possibility of improved interfacial bonding with a polymer matrix.

Toebes et al. [7] examined the effect of liquid phase oxidation of carbon nanofibers in nitric acid and mixtures of nitric and sulfuric acid for times up to two hours. The graphitic structure of the nanofibers was not altered by the treatments, but the texture of the fibers were significantly changed through increase in the specific surface area and pore volume due to the opening of the fiber inner tubes. The total oxygen content and surface oxygen functional groups were affected by the treatment time and acid type. Oxygen groups were also formed in the first 2–3 nm of the subsurface of the fibers.

Bubert et al. [8] investigated the influence of plasma treatment on the surface properties of carbon nanofibers by X-ray photoelectron spectroscopy (XPS) in combination with ion sputtering, acid-base titration, derivatization of carbonyl groups, pyrolysis, and CH analysis. The results indicated that the fiber surface is covered by a monomolecular oxygen-containing layer and that plasma treatment allows complete oxygen functionalization of the uppermost surface layer. XPS provides an average value for the content of functional groups of the first ten to fifteen molecular layers.

A number of results have been reported on the effect of chemical modification of carbon nanotubes on nanocomposite properties. Xu et al. included a nitric acid-oxidized nanofiber/vinyl ester composite in an examination of electrical properties of nanocomposites [9]. The resistivity of the oxidized fiber nanocomposites were much higher than that of those produced with untreated fibers. The oxidation was reported to have increased oxygen percentage by approximately 20% with the addition of anhydride, quinine, ether, and ester functional groups. The oxidized layer could reduce conductivity through percolation pathways. The functional groups should also improve wetting by the polymer matrix. A strong bond between matrix and fiber could encase the fiber and serve as an insulating covering.

Finegan et al. [10] examined the mechanical properties of carbon nanofiber/polypropylene composites in an attempt to optimize carbon nanofiber surface treatment. The fiber-matrix adhesion was qualitatively studied by scanning electron microscopy (SEM), and the strength and stiffness of the composites were evaluated from tensile tests. One sample of nanofibers was oxidized in air at 450 °C and a second sam-

ple was oxidized with carbon dioxide in a tube furnace. Fiber matrix adhesion was improved by moderately oxidizing the fibers in either air or carbon dioxide. The carbon dioxide oxidation was more effective as it increased the external surface area and the surface energy of the fibers. However in the preparation of the nanocomposites, the fibers were either ball milled or force sieved, thereby possibly altering the fiber aspect ratios resulting in decreased mechanical testing results.

Cortes et al. [11] exposed carbon nanofibers to a series of chemical treatments in nitric acid prior to mixing with polypropylene. The oxidized fiber nanocomposites did not improve electrical properties of the polymer, did not produce significant changes in the mechanical properties of the composites, and showed a decrease in tensile strength. The nanocomposites had only produced 5 wt% VGCF compositions. Higher fiber content may have led to increases in the mechanical properties of the composites.

In conventional carbon fiber-reinforced composites, there have been a number of studies completed to generate strong adhesion between the fiber surface and matrix to improve stress transfer from the matrix to the reinforcing fibers. Continuous surface electrochemical oxidation has been the preferred method of fiber surface treatment to enhance interfacial bonding. Electrochemical treatments have been carried out in acid and alkaline aqueous solutions of ammonium sulfate, ammonium bicarbonate, sodium hydroxide, diammonium hydrogen phosphate, and nitric acid.

Anodic oxidation of fibers in electrolytes can produce a variety of chemical and physical changes in the fiber surface. Harvey et al. [12] examined surfaces of conventional carbon fibers by XPS after electrochemical treatment by galvanostatic and potentiostatic cell control under varying potential, reaction time, and electrolytes. They noted that the rise in interlaminar shear strength (ILSS) with surface treatment is not dependent on O-1s:C-1s ratios or the amount of carboxyl functionality on the surface, thereby supporting the view that mechanical keying of the resin to the fiber surface plays an important role in forming the resin-fiber bond.

Gulyas et al. [13] subjected PAN-based carbon fibers to electrochemical oxidation under a wide variety of conditions—varying electrolyte, electrolyte concentration, and applied voltage. The functional groups formed on the surface of the fibers were dependent on the type of electrolyte used, and the number of functional groups found on the fiber surface was dependent on electrolyte concentration and voltage. A close correlation was found between surface chemistry and fiber/matrix adhesion. The concentration of certain functional groups could be quantitatively related to ILSS.

Yue et al. [14] applied continuous electrochemical oxidation to high-strength PAN-based carbon fibers in 1% by weight potassium nitrate. Fiber weight loss increased with electrochemical oxidation. A large internal micro porous surface area was generated due to the formation of acidic functions. XPS indicated that the concentration of oxygen within the outer 50 Å of the fibers increased on oxidation. XPS C-1s and O-1s spectra showed an increase in primarily carboxyl or lactone groups. The oxygen-rich surfaces in the micro porous regions chemisorbed oxygen and water. The

O-2s—C-2s peak separation increased in the valence band spectra as the extent of oxidation increased due to carbonyl group contribution.

In this study, vapor-grown carbon nanofibers were subjected to electrochemical oxidation in 0.1 M nitric acid for varying times to modify the interface between the nanofibers and epoxide molecules in epoxide/nanofiber composites. X-ray photoelectron spectroscopy was employed to characterize surfaces with regard to the content of carbon, oxygen, and nitrogen. The strength of adhesion between the fiber and an epoxy (thermoset) matrix was characterized by the tensile strength and modulus, and the electrical and thermal properties of the composites were investigated from the viewpoint of surface treatment of carbon nanofibers.

2. EXPERIMENTAL SETUP AND PROPERTY MEASUREMENT

The carbon nanofibers used in this study were produced at Applied Sciences, Inc. (Detroit, MI, USA) and were from the Pyrograf IIITM family of fibers. This group of nanofibers (labeled PR-24) has diameters between 60 and 100 nm and lengths ranging from 30 to 100 μm . The nanofibers were electrochemically surface treated using nitric acid as an electrolyte in a concentration of 1 wt%. Approximately 15 g of nanofibers for each trial were packed into covered, porous plastic beakers and submerged in the acidic solution. Previous studies have shown that an amount of 12% by weight added to epoxy polymer has led to maximum mechanical performance. We chose a graphite electrode submerged into the packed nanofibers, and a specific applied current was set at 0.1 amps. The time of the treatments was 30 seconds, 1 minute, 2 minutes, 4 minutes, 8 minutes, and 15 minutes. Following treatment, the oxidized fibers were washed with distilled water until attaining a neutral pH and dried in a vacuum oven at 100 °C for 48 hours.

The functionalized carbon nanofibers were characterized using X-ray photoelectron spectroscopy (XPS). The samples were oriented such that the axial direction was in the plane of the X-ray source and the analyzer detection slit. During all XPS experiments, the pressure inside the vacuum system was maintained at approximately 1 torr. A nonlinear least squares curve fitting program with a Gaussian-Lorentzian mix function and background subtraction was used to deconvolve the XPS peaks.

While investigation of surface chemistry was performed by XPS using chemical shift phenomena, in several cases, relative chemical shifts of different groups are below the energy resolution attainable by XPS spectrometers due to the existence of significant intrinsic peak widths. In these cases, other sample properties, like chemical reactivity, could operate the requested discrimination. Chemical derivatization XPS (CD-XPS), based on selective reaction labeling groups of interest, was used to improve the selectivity and sensitivity of the XPS analysis. The methodology has been applied mainly to organic polymers, even though some inorganic materials have also been studied. Derivatization reactions have been established for C—OH, COOH, C=O, and C—NH₂ groups. Infor-

mation obtained by the simple XPS evidence of the marker element must be complemented by careful analysis of the main signals, to which both the organic material and the derivatizing agent contribute. This procedure will determine whether each reaction occurs according to the expected stoichiometry.

C—OH groups can be esterified by trifluoroacetic anhydride (TFAA). A procedure for the derivatization of a polymer sample calls for the sample to be introduced into a glass test tube. Two mL of TFAA were injected into the test tube below the sample, without contacting it. The test tube was sealed, and the reaction with the TFAA vapor was allowed to proceed for 15 minutes at room temperature. The sample was then removed from the test tube, and transferred to the XPS spectrometer for analysis.

Derivatizing the sample with TFAA vapor results in the conversion of the phenol substituent to a trifluoroester group. This leads to the appearance of new peaks at 290.4 and 293.7 eV which are attributed to the ester and CF₃ carbon atoms, respectively. The peak area of the trifluoroacetic ester (CF₃COO) component is used for a quantitative estimate for the C—OH groups by calculating one third of the F1s area. TFAA labels virtually all of the hydroxyl groups within the XPS sampling depth.

COOH groups can be esterified by trifluoroethanol (TFE) vapors, making use of di-*t*-butyl carbodiimide (DtC) as a dehydrating agent. A procedure for the derivatization of a polymer sample calls for the sample to be suspended in a glass test tube; TFE (0.9 mL), pyridine (0.4 mL), and DtC (0.3 mL) were sequentially injected below the sample, without contacting it, at 15 minutes intervals. The test tube was sealed with a cap and the reaction was allowed to proceed at room temperature for 12 hours. The samples were then transferred to the XPS spectrometer and analyzed.

An assumption of the reaction is that the reaction product of DtC (*N,N'*-di-(*t*-butyl)-urea) is completely removed from the surface of the reacted organic material, though no washing stage is performed. This behavior has been confirmed in literature. The reaction has been shown to yield about 99% esterification of the COOH groups by TFE. Esterification by TFE causes three fluorine atoms to be introduced into the sample for each COOH group. An enhancement of the response factor should be obtained and the XPS detectability of this functionality then improved. One source of error could be due to the presence of ionized COOH groups, which are not susceptible to esterification mediated by carbodiimides.

The carbon nanofibers were added to an epoxy resin matrix (EPON 862) forming a nanocomposite. Since bulk nanofibers are difficult to incorporate into resin matrices, the nanofibers were first dispersed in the epoxy resin. The resulting mixture was cured under pressure in a silicone mold.

The mechanical properties of the nanocomposites were measured using the three-point bending test according to ASTM D790-00. The specimen size was 3.0 in (length) by 0.5 in (width), with the depth dependent upon the composite sample. The three-point bend test had a span ratio (span-to-depth of sample) of 16 : 1. This value is suggested

TABLE 1: Atomic percentages of nanofibers as a function of electrochemical treatment time.

Sample	Oxygen %	Carbon %
As-received	2.0	98.0
30 s treatment	2.3	97.7
1 min treatment	2.8	97.2
2 min treatment	3.5	96.5
4 min treatment	4.2	95.8
8 min treatment	5.4	94.6
10 min treatment	7.6	92.4
12 min treatment	8.3	91.7
15 min treatment	8.6	91.4

by ASTM D790-00 for materials with a depth greater than 0.0625 in.

The thermal conductivity of each nanocomposite incorporated a xenon flash diffusivity test. The procedure is outlined in ASTM C714-72, with the test specimens cut to 0.5 in (length) by 0.5 in (width) by 0.03 in (depth). Thermal diffusivity is calculated according to the equation $\alpha = 0.139L^2/t_{1/2}$, where L is the thickness of the sample and $t_{1/2}$ is the time at which the rear surface of the test specimen reaches one half its maximum temperature. The thermal diffusivity parameter is used in conjunction with the specific heat and density of the nanocomposite to calculate the thermal conductivity. The tests for specific heat and density were carried out according to ASTM E1269-89 and ASTM C693-74, respectively. Thermal conductivity is calculated according to the equation $K = C_p \rho \alpha$, where C_p is the specific heat of the sample and ρ is the density of the sample.

The electrical properties of the carbon nanocomposites were studied utilizing a four-point test according to ASTM B 193-87. The two outer leads of the tester are connected to the current source and the two inner leads are used to measure the voltage drop through the nanocomposite. Ohm's law, equation 6, allows for the resistance of the sample to be determined. By coupling the calculated resistance with the known cross-sectional area and distance between leads, the resistivity ρ of the sample can be deduced

3. RESULTS AND DISCUSSION

Surface characterization of the nanofibers by XPS (see Table 1) showed an increase in oxygen content from 2% in the as-received fibers to 8.6% in the fibers treated for fifteen minutes. The N 1s peak was negligible in all cases.

Deconvolution of the C 1s spectra (see Table 2) gives the potential for five peaks: graphitic carbon (284.6 eV), carbon present in phenolic, alcohol, ether, or C=N groups (286.1–286.3 eV), carbonyl or quinone groups (287.3–287.6 eV), carboxyl or ester groups (288.4–288.9 eV), and carbonate (290.4–290.8 eV). Figure 2 shows the calculated percentage of graphitic and functional carbon atoms. There is a significant decrease in the relative content of graphitic carbon (peak I) and a rise in the relative content of carbon bonded

TABLE 2: Calculated percentages of graphitic and functional carbon atoms.

Sample	I	II	III	IV	V
30 s treatment	90	6	4	0	0
1 min treatment	87	13	0	0	0
2 min treatment	86	7	2	2	3
4 min treatment	80	14	6	0	0
8 min treatment	78	9	6	4	3
10 min treatment	79	11	9	0	0
12 min treatment	75	21	4	0	0
15 min treatment	74	23	2	0	0

TABLE 3: Calculated percentages of oxygen-containing groups.

Sample	I	II	III
30 s treatment	57	43	0
1 min treatment	67	33	0
2 min treatment	70	22	8
4 min treatment	75	20	5
8 min treatment	78	22	0
10 min treatment	81	19	0
12 min treatment	83	17	0
15 min treatment	84	16	0

to oxygen-containing functions (peaks II, III, IV, and V) with increasing amount of electrochemical treatment. The increase in relative concentration of carbon oxygen complexes occurs because the outer layers of the fibers become increasingly porous. The fraction of carbon atoms in the region which exists on the pore surfaces increases. These carbon atoms are the sights of oxidation, thereby increasing the relative amount of oxygen.

Table 3 shows the deconvolution of the O 1s spectra fitted to three component peaks: C=O groups including ketone, lactone, carbonyl (531.2–531.6 eV), C–OH and C–O–C groups (532.2–533.4 eV), and chemisorbed and adsorbed water (534.6–535.4 eV). The C=O contribution to the O 1s profile increases significantly with increasing amount of electrochemical treatment.

As shown in Figure 1 and Table 4, a modest degree of electrochemical treatment improved the flexural modulus of the nanocomposite by enhancing the interfacial adhesion between the fiber and resin. The treatment time of 30 seconds allowed for a 4.32% increase in flexural modulus. A maximum improvement of 74% occurred with an electrochemical treatment time of twelve minutes. Prolonged subjection to the electrochemical treatment beyond eight minutes showed a drop in flexural modulus. This may be due to the oxide layer actually causing failure of the fiber-resin bond or possibly the additional treatment time may have damaged the fiber surface.

The electrochemical treatment did have a slightly negative effect on the thermal conductivity of the manufactured

TABLE 4: Nanocomposite mechanical properties with relative standard deviation.

Sample	Surface treatment time (min)	Mass %	Modulus (GPa)	STD	Strength (GPa)	STD
EPON 862	—	0	1.7730	0.0688	0.0976	0.0018
PR-24-PS	0	12	2.5783	0.1267	0.1196	0.0057
PR-24-PS-ET (0.5)	0.5	12	2.6898	0.5464	0.0901	0.0143
PR-24-PS-ET (1)	1	12	2.7399	0.1619	0.1037	0.0076
PR-24-PS-ET (2)	2	12	2.8014	0.1124	0.1072	0.0150
PR-24-PS-ET (4)	4	12	3.0261	0.3434	0.1017	0.0071
PR-24-PS-ET (8)	8	12	3.4915	0.0217	0.1163	0.0093
PR-24-PS-ET (10)	10	12	3.9535	0.0118	0.1263	0.0087
PR-24-PS-ET (12)	12	12	4.4856	0.0123	0.1462	0.0068
PR-24-PS-ET (15)	15	12	3.0690	0.3558	0.1041	0.0099

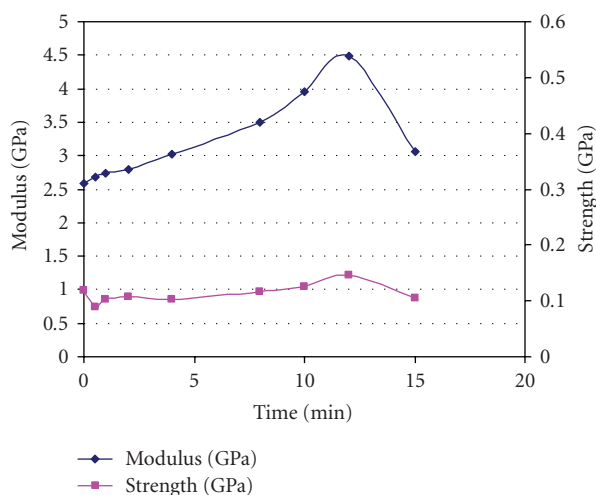


FIGURE 1: Nanocomposite mechanical properties as a function of electrochemical treatment time.

nanocomposites. As shown in Table 1, there was a significant decrease in the heat capacity of the composites with functionalized nanofibers, indicating an effect of additional oxygen content. There was not a significant change in the thermal diffusivity results. In addition, the electrical resistivity of the nanocomposites decreased with increasing electrochemical treatment time. This may be due to the increase in oxygen content causing the formation of a narrow insulating layer along the surface of the fibers (see Table 5).

The SEM examination of the fracture surface of various samples following mechanical testing has shown that the interface between the nanofiber and epoxy resin matrix has only minimal adhesion in the form of covalent bonds (Figures 2 and 3). An interfacial gap between the two phases is always present and its location may vary from one sample to another (single arrows in Figures 2 and 3).

The inability to create an effective interface between the carbon nanofiber and the neat resin prevents the transfer of mechanical loads between the two regions. This hindrance of load transference results in mechanical properties that are nominally better than those of the neat resin. To better understand the role of surface chemistry of the nanofiber, the



FIGURE 2: Longitudinal view of untreated nanofibers-based nanocomposite fracture surface.

effect of surface functionalization of nanofiber on the mechanical properties of produced nanocomposites was studied.

The fracture surface of the surface-functionalized nanocomposite is markedly different from that of the PR-24 nanocomposite. Along the length of the chemically modified nanofiber within the epoxy matrix, there is an apparent interface devoid of the gaps present in the pyrolytically stripped nanocomposite (see Figure 4). The body of the nanofiber is actually covered with lighter regions of “strings” and bumps arranged in the form of “knife teeth.” These bumps are made of resin residue. This region is more closely studied using high-resolution SEM and TEM techniques.

In Figure 5, it is shown that the surface of the functionalized nanocomposite is covered with masses of residual epoxy resin. This demonstrates that the nanocomposite did not fracture along the nanofiber/resin interface. Rather, the resin remained adhered to the nanofiber following fracture and the mechanical failure took place within the resin phase of the nanocomposite. TEM analysis offers a more thorough explanation for the interaction between the modified surface of the nanofiber and the epoxy resin.

TABLE 5: Thermal and electrical properties of nanocomposites as a function of treatment time.

Sample	Surface treatment time (min)	Mass %	Resistivity (Ohm-cm)	K (W/m-K)	Density (g/cm ³)
EPON 862	—	0	3.28E + 10	0.1768	1.198
PR-24-PS	0	12	1.58E + 00	0.3731	1.252
PR-24-PS-ET (0.5)	0.5	12	4.13E + 00	0.2992	1.237
PR-24-PS-ET (1)	1	12	5.16E + 01	0.3476	1.253
PR-24-PS-ET (2)	2	12	3.14E + 03	0.3303	1.246
PR-24-PS-ET (4)	4	12	5.57E + 06	0.3032	1.240
PR-24-PS-ET (8)	8	12	3.35E + 07	0.3290	1.235
PR-24-PS-ET (10)	10	12	5.56E + 10	0.3334	1.257
PR-24-PS-ET (12)	12	12	4.54E + 09	0.3493	1.234
PR-24-PS-ET (15)	15	12	3.69E + 10	0.3348	1.254

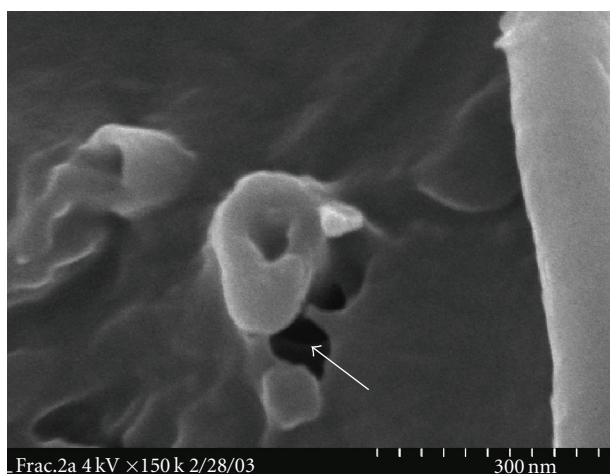


FIGURE 3: Cross view of untreated nanofibers-based nanocomposite fracture surface.

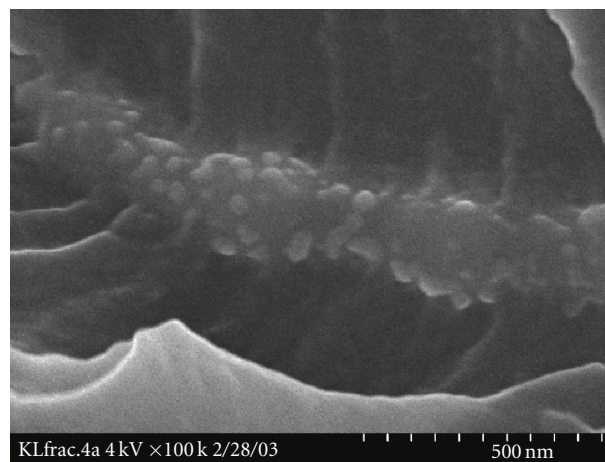


FIGURE 5: Higher magnification SEM of surface-functionalized nanocomposite fracture surface.

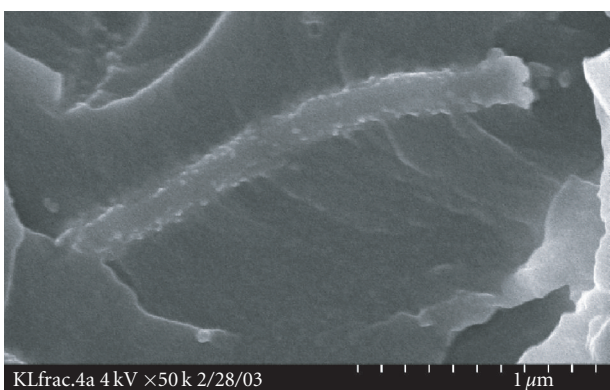


FIGURE 4: SEM micrograph of surface-functionalized nanocomposite fracture surface.

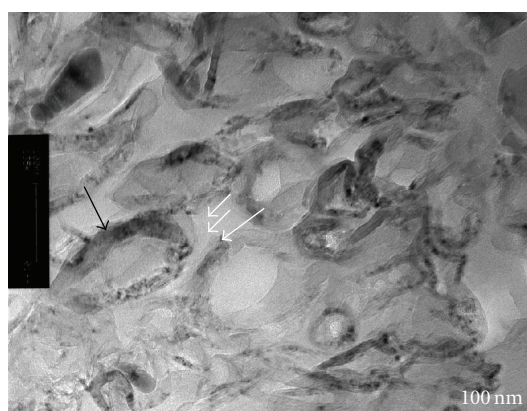


FIGURE 6: TEM micrograph of surface-functionalized transverse fracture surface.

The black arrows in Figures 6 and 7 show the exposed ends of nanofibers and their bodies within the resin matrix at the fracture site. The bright-field micrograph shows a change in a grey scale to demonstrate differences in electronic density within the resin matrix. The epoxy resin areas do not

have one consistent shade, however. The single white arrows in Figures 6 and 7 point to areas of higher electronic density than that of areas showing lighter contrast (double white arrows in Figures 6 and 7). This difference in a grey-scale may indicate some structural changes within continuous resin

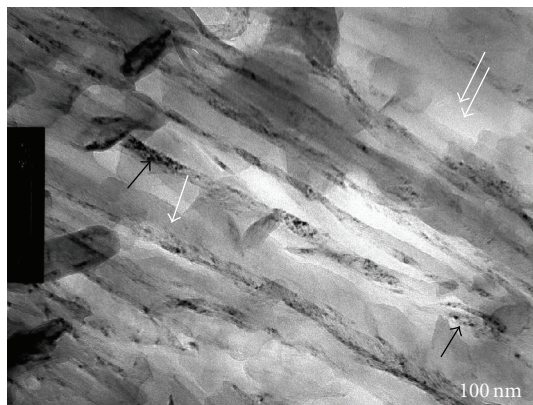


FIGURE 7: TEM micrograph of surface-functionalized longitudinal fracture surface.

matrix. A longitudinal representation offers a clearer understanding of the physical property gradient within the surface-functionalized carbon nanocomposite.

An analysis using high resolution TEM allows for a more complete understanding of the changes that occur at the interface between the surface-functionalized carbon nanofibers and the continuous epoxy resin phase.

At high resolution, the individual graphene planes of a nanofiber can be seen along with the region of the epoxy region. Moving from the upper-left towards the lower-right of the micrograph, the interface with the nanofiber is crossed into the parallel layers within the nanofiber representing the wall of nanofiber. Further down the micrograph, another interface is crossed into the epoxy resin phase with very organized turbostratic carbon (circled areas in Figure 8 with a wavy, spaghetti-like look). In this region, there is a local molecular orientation of basic structural units that are in the form of columns and clusters with discontinuous but preferential molecular orientation parallel to the nanofiber axis. The polymer interphase is no longer amorphous but has gained a two-dimensional order similar to the microstructure of carbonized PAN carbon fiber. Epoxy generally has gravel-like appearance under HR-TEM, which indicates an amorphous structure. This change in physical properties demonstrates the presence of an “interphase.” Due to the chemical interaction between the surface-functionalized nanofiber and the resin, a new material has been created with unique physical properties.

4. CONCLUSION

In principle, achieving high tensile strength composites with nanofibers as the reinforcement relies on factors including weight fraction, strength of the nanofibers, dispersion of the fibers, and the strength of the interface. Assembly of these factors may be envisioned without difficulty; however, the latter factor—strength of the interfacial bond between nanofiber and matrix—is problematic due to the inert nature of the smooth hexagonal surface commonly presented by the nanofiber class of reinforcement.

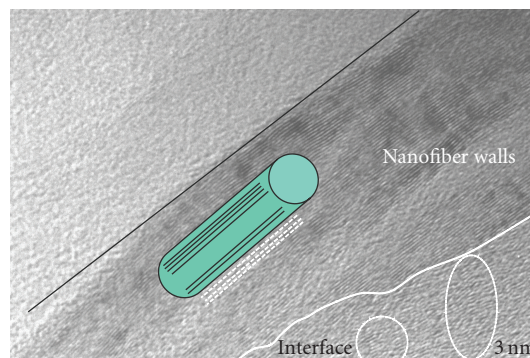


FIGURE 8: High resolution TEM showing an oriented interface between nanofiber and matrix.

Due to the exposed graphitic edge planes of nanofiber surfaces, it is possible to add functional groups. The addition of functional groups will greatly increase the ability of the nanofiber to bond to polar matrix materials such as epoxy. As a result of this surface modification, the mechanical properties of the nanocomposites were significantly enhanced, and the chemical properties such as heat capacity of the polymer were lowered. This improvement might be obtained by an internal reaction between the surface functional groups and polymer matrix. Transmission electron microscopy characterization shows that the post-synthesis surface treatment has contributed to the formation to a very dense and oriented interface between nanofiber and matrix.

The surface-treated nanofiber-based nanocomposites samples exhibit better mechanical properties than any of the nonsurface-treated nanofiber-based nanocomposites. The improvement in mechanical properties is due to the formation of gradients at interfaces and interphases between the nanofibers and epoxy resins. These interphases cause the polymeric nanocomposites to behave as a continuous phase in which the mechanical transport properties between parent individual ingredients (nanofibers and epoxy matrix) were enhanced.

There was a significant decrease in the relative content of graphitic carbon and an increase in the relative content of carbon bonded to oxygen-containing functions with increasing amount of electrochemical treatment. The increase in relative concentration of carbon oxygen complexes occurs because the outer layers of the fibers become increasingly porous allowing for additional sights of oxidation. The increasing amounts of oxygen with electrochemical treatment corresponded to an increase in the flexural modulus of nanocomposites manufactured with the treated fibers. This indicates an improvement in interfacial adhesion between the fibers and the resin. The treated nanofibers had negative impact on the heat capacity of the nanocomposites, but they did not affect the thermal diffusivity of the composites. The electrical resistivity of the nanocomposites decreased with increasing electrochemical treatment time due in part to the increased concentration of oxygen functional groups.

REFERENCES

- [1] V. Z. Mordkovich, "Carbon nanofibers: a new ultrahigh-strength material for chemical technology," *Theoretical Foundations of Chemical Engineering*, vol. 37, no. 5, pp. 429–438, 2003.
- [2] B. Maruyama and K. Alam, "Carbon nanotubes and nanofibers in composite materials," *SAMPE Journal*, vol. 38, no. 3, pp. 59–70, 2002.
- [3] E. Lonzo and V. Barrera, "Nanofiber-reinforced thermoplastic composites. I. thermoanalytical and mechanical analyses," *Journal of Applied Polymer Science*, vol. 79, no. 1, pp. 125–133, 2000.
- [4] R. J. Kuriger, M. K. Alam, D. P. Anderson, and R. L. Jacobsen, "Processing and characterization of aligned vapor grown carbon fiber reinforced polypropylene," *Composites Part A*, vol. 33, no. 1, pp. 53–62, 2002.
- [5] R. D. Patton, C. U. Pittman Jr., L. Wang, and J. R. Hill, "Vapor grown carbon fiber composites with epoxy and poly (phenylene sulfide) matrices," *Composites Part A*, vol. 30, no. 9, pp. 1081–1091, 1999.
- [6] S. Lim, S.-H. Yoon, I. Mochida, and J.-H. Chi, "Surface modification of carbon nanofiber with high degree of graphitization," *Journal of Physical Chemistry B*, vol. 108, no. 5, pp. 1533–1536, 2004.
- [7] M. L. Toebes, J. M. P. van Heeswijk, J. H. Bitter, A. J. van Dillen, and K. P. de Jong, "The influence of oxidation on the texture and the number of oxygen-containing surface groups of carbon nanofibers," *Carbon*, vol. 42, no. 2, pp. 307–315, 2004.
- [8] H. Bubert, X. Ai, S. Haiber, et al., "Basic analytical investigation of plasma-chemically modified carbon fibers," *Spectrochimica Acta Part B*, vol. 57, no. 10, pp. 1601–1610, 2002.
- [9] J. Xu, J. P. Donohoe, and C. U. Pittman Jr., "Preparation, electrical and mechanical properties of vapor grown carbon fiber (VGCF)/vinyl ester composites," *Composites Part A*, vol. 35, no. 6, pp. 693–701, 2004.
- [10] I. C. Finegan, G. G. Tibbetts, D. G. Glasgow, J.-M. Ting, and M. L. Lake, "Surface treatments for improving the mechanical properties of carbon nanofiber/thermoplastic composites," *Journal of Materials Science*, vol. 38, no. 16, pp. 3485–3490, 2003.
- [11] P. Cortés, K. Lozano, E. V. Barrera, and J. Bonilla-Rios, "Effects of nanofiber treatments on the properties of vapor-grown carbon fiber reinforced polymer composites," *Journal of Applied Polymer Science*, vol. 89, no. 9, pp. 2527–2534, 2003.
- [12] J. Harvey, C. Kozlowski, and P. M. A. Sherwood, "X-ray photoelectron spectroscopic studies of carbon fibre surfaces," *Journal of Materials Science*, vol. 22, no. 5, pp. 1585–1596, 1987.
- [13] J. Gulyás, E. Földes, A. Lázár, and B. Pukánszky, "Electrochemical oxidation of carbon fibres: surface chemistry and adhesion," *Composites Part A*, vol. 32, no. 3-4, pp. 353–360, 2001.
- [14] Z. R. Yue, W. Jiang, L. Wang, S. D. Gardner, and C. U. Pittman Jr., "Surface characterization of electrochemically oxidized carbon fibers," *Carbon*, vol. 37, no. 11, pp. 1785–1796, 1999.

Research Article

Low-Temperature Preparation of Amorphous-Shell/ Nanocrystalline-Core Nanostructured TiO₂ Electrodes for Flexible Dye-Sensitized Solar Cells

Dongshe Zhang,¹ Hengyao Hu,² Laifeng Li,³ and Donglu Shi^{1,2,4}

¹ Department of Chemical and Materials Engineering, University of Cincinnati, Cincinnati, OH 45221-0012, USA

² Institute of Micro and Nano Science and Technology, Shanghai Jiaotong University, Shanghai 200240, China

³ Technical Institute of Physics and Chemistry, Chinese Academy of Sciences, Beijing 10080, China

⁴ The Institute for Advanced Materials and Nano Biomedicine, Tongji University, 67 Chifeng Road, Shanghai 200092, China

Correspondence should be addressed to Dongshe Zhang, dongshe88@yahoo.com

Received 2 June 2007; Accepted 26 February 2008

Recommended by Hongchen Gu

An amorphous shell/nanocrystalline core nanostructured TiO₂ electrode was prepared at low temperature, in which the mixture of TiO₂ powder and TiCl₄ aqueous solution was used as the paste for coating a film and in this film amorphous TiO₂ resulted from direct hydrolysis of TiCl₄ at 100°C sintering was produced to connect the particles forming a thick crack-free uniform nanostructured TiO₂ film (12 μm), and on which a photoelectrochemical solar cell-based was fabricated, generating a short-circuit photocurrent density of 13.58 mA/cm², an open-circuit voltage of 0.647 V, and an overall 4.48% light-to-electricity conversion efficiency under 1 sun illumination.

Copyright © 2008 Dongshe Zhang et al. This is an open access article distributed under the Creative Commons Attribution License, which permits unrestricted use, distribution, and reproduction in any medium, provided the original work is properly cited.

1. INTRODUCTION

Dye-sensitized solar cells (DSSCs) [1–3] have been extensively studied more than a decade because they presented high-efficient, cost-effective, and environmentally friendly advantages. In the cell dye-sensitized semiconductor, photoelectrode plays an essential role, and conventionally nanocrystalline porous TiO₂ electrode is prepared by coating a paste containing organic additives on a rigid conductive glass substrate, following a procedure of high-temperature sintering to remove the organic additives [1, 2], which are necessary to form a thick crack-free uniform film and optimize the microstructure of the electrode for photosensitization [1–4].

Flexible DSSCs [5–14], based on the substrates of indium tin oxide (ITO) coated polyethylene terephthalate (PET), or polyethylene naphthalate (PEN) substituting for rigid glass substrates, are regarded as one possible breakthrough in the field of DSSC regarding their commercialization, because flexible DSSCs have presented great advantages of low cost of production and wide application. Conductive plastic sub-

strates, such as ITO/PET or ITO/PEN, can be processed by a continuous process like roll-to-roll production for porous nanocrystalline film coating, therefore, greatly decreasing the production cost of the solar cells. Meanwhile, flexible DSSCs can become part of a variety of every-day products and turn them into energy sources. The possibility to produce the flexible DSSCs in any shapes would open almost endless opportunities to the designers of such products. In addition, it is light weight, having portable character.

Underlying the flexible DSSCs, the necessary low-temperature preparation of porous nanocrystalline metal oxides semiconductor films has been a well-highlighted and on-going challenge up to today, because the conventional method of high-temperature preparation cannot be applied to prepare films on flexible plastic substrates, which only endure temperature of up to around 150°C. So far, there have been a number of efforts concerned with the preparation of nanoporous films at low temperature. The methods reported were low-temperature heating [5, 6], compression [7, 8], microwave irradiation [9, 10], electron-beam annealing [11] and chemical-vapor deposition with UV irradiation [12],

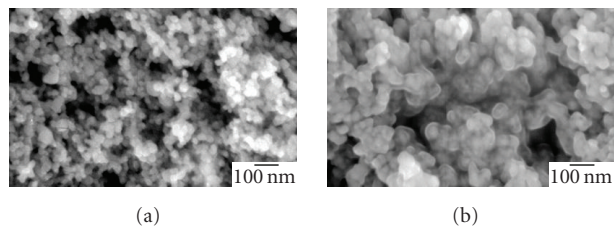


FIGURE 1: SEM photographs of the TiO₂ electrodes (a) before and (b) after sintering.

and hydrothermal crystallization [13, 14]. However, the conversion efficiencies of the flexible DSSCs achieved so far are lower than those obtained by high-temperature sintering. One main reason is that low-temperature films have low level of crystallization of interconnection between particles comparing with high-temperature film [5–14]. It is showed that low-temperature film has poor interconnection between nanocrystalline particles, because the above-mentioned methods that have been developed so far cannot result in as perfect interconnection as high-temperature sintering did [5–14]. In fact, the part of low level of crystallization worked as the interconnection of nanocrystalline particles in the low-temperature film existed in all flexible DSSCs. So the part of low level of crystallization in the low-temperature film played an important role in the chemical reaction at interface of the cell. To well understand how it works and further improve the performance of low-temperature film, therefore, in this study, we developed a simple method and prepared an amorphous shell/nanocrystalline core nanostructured film under 100°C sintering. The amorphous shell not only is responsible for the interconnection between nanocrystalline particles, but also plays an important role in the interface chemical reaction. The as-prepared films were mechanically stable. It is showed that amorphous TiO₂ can work effectively in DSSCs. Its performance was compared with that of nanocrystalline porous film prepared at both high and low temperature.

2. EXPERIMENTAL

Nanostructured TiO₂ electrode with the structure of amorphous shell/nanocrystalline core was prepared by the following method. 0.8 g P25 (Degussa, Germany, 30% rutile and 70% anatase, BET surface area 55 m²/g, particle size 25 nm) and 0.5 M TiCl₄ water solution were ground in an agate mortar for about 2 hours to get viscous paste, then coated on the fluorine doped SnO₂-coated conductive glass (sheet resistance ca. 10 Ω/□) by doctor-blade technique. Subsequently, the film was sintered at 100°C for 12 hours. The resulting film thickness was 12 μm but can be varied by changing the paste concentration or the adhesive tape thickness. The electrode was directly immersed in an ethanol solution of *cis*-bis(4,4'-dicarboxy-2,2'-bipyridine)-bis(thiocyanato)ruthenium(II), N3 dye (0.05 mM) overnight at room temperature. This dye-sensitized electrode was employed as a working electrode and platinized conductive

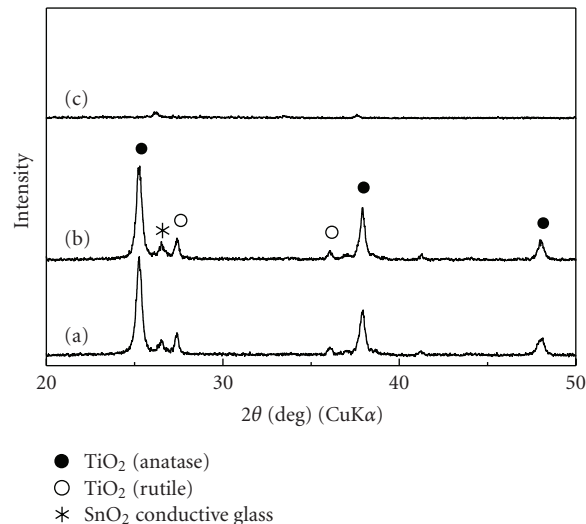


FIGURE 2: XRD patterns of the TiO₂ electrodes (a) before and (b) after sintering as well as (c) the TiO₂ resulted from 0.5 M TiCl₄ water solution sintered at 100°C for 12 hours (small peaks resulted from SnO₂ conductive glass).

glass as a counter electrode for assembling a sandwich-type dye cell. The electrolyte was 0.5 M KI and 0.03 M I₂ in ethylene carbonate-acetonitrile (4:1 by volume). No special efforts were made to optimize the composition of the electrolyte. Photoelectrochemical measurements were performed on the TiO₂ film electrodes under white light illumination by a 500 W Xe lamp equipped with IR and <420 nm cutoff filters from the side of the conductive glass back contact. Surface morphology of the electrode was observed by a Topcon ABT-150FS scanning electron microscope (SEM). X-ray diffraction patterns (XRD) of the electrodes were measured by a Rigaku RAD-2R using Cu Kα radiation at 40 kV and 20 mA by scanning at 2° 2θ min⁻¹.

3. RESULTS AND DISCUSSION

The SEM photographs of the TiO₂ electrodes before and after sintering at low temperature of 100°C are presented in Figure 1. It revealed morphological homogeneity of both electrodes with micropores and interconnected particles, but before sintering at low temperature of 100°C the average particle size was approximately like the one of P25, while after sintering it was increased obviously and the connection between particles was also improved. The XRD patterns of the TiO₂ electrodes before and after sintering at low temperature of 100°C are shown in Figure 2. No new peak was observed after sintering at low temperature of 100°C and, even both the relative intensity and line width of crystal peak were not changed before and after sintering, showing neither new compound nor crystal TiO₂ was formed in the film during the sintering. According to the Scherrer equation [$L = 0.9\lambda/B(2\theta) \cos \theta$, where L is the crystallite size and $B(2\theta)$ is the line width] together with the results of XRD measurement, the crystal size should not

be changed before and after sintering at low temperature of 100°C. Therefore, it conflicted with the results of SEM measurement. Figure 2 also shows XRD pattern of TiO₂ resulted from 0.5 M TiCl₄ water solution sintered at 100°C for 12 hours. From Figure 2, one can see no any crystal TiO₂ peaks were observed, showing that amorphous TiO₂ was formed during the sintering. So we can think that in the film TiCl₄ was condensed at the surface of the crystal TiO₂ of P25 before sintering and, during the sintering at low temperature of 100°C amorphous TiO₂ resulted from TiCl₄ grew on the surface of crystal TiO₂ of P25 forming amorphous shell/nanocrystalline core particles, resulting in increments of the sizes of particles as well as improvement of the connection between particles in the film. So the formed electrode was crack free, robust, and uniform.

The amount of adsorbed N3 dye on the nanostructured TiO₂ electrode was 1.1×10^{-7} mol/cm²,² and from this data the calculated surface roughness factor was about 1000,¹⁵ showing that the electrode had large surface area and the dye of N3 can also strongly adsorb on the amorphous TiO₂ surface. The photocurrent-voltage characteristic of the cell based on this nanostructured TiO₂ electrode after sintering at low temperature of 100°C is presented in Figure 3. Under 1 sun illumination, a short-circuit photocurrent density (I_{sc}) of 13.58 mA/cm², an open-circuit voltage (V_{oc}) of 0.647 V, and a fill factor of 51% were obtained, yielding an overall 4.48% light-to-electricity conversion efficiency. Figure 4 shows the dependence of V_{oc} on illumination intensity. Within the range of the measurement the open-circuit voltage versus incident light intensity was a liner relationship and its slope was 130 mV per decade, yielding a rectification coefficient of 2.5. This value was higher than that of 1 to 2 [15–17] of dye-sensitized solar cell based on the nanocrystalline TiO₂ electrode sintered at 450°C for 30 minutes, meaning the density of surface state in this amorphous electrode was higher which may result in larger recombination [15]. However, this value was lower than that of 3.2 [5] of the cell based on TiO₂ electrode sintered at 100°C for 24 hours, showing that amorphous TiO₂ improved the connection between particles in the film and decreased some recombination therefore, larger I_{sc} and conversion efficiency was observed. All these experiments showed that the dye of N3 can inject electrons into amorphous TiO₂ effectively and the recombination rate was lower and amorphous TiO₂ can also collect and transport electrons effectively. Therefore, the cell based on the amorphous shell/nanocrystalline core nanostructured TiO₂ electrode prepared at low temperature had high-conversion efficiency up to 4.48%. However, when this amorphous electrode was further sintered at 450°C the amorphous became into well crystal, which was confirmed by XRD measurement of TiO₂ from the decomposition of TiCl₄ with 450°C sintering. A DSSC based on it presented a short-circuit photocurrent density of 20.2 mA/cm², an open-circuit voltage of 0.69 V, and a fill factor of 51% were obtained, yielding an overall 7.1% light-to-electricity conversion efficiency under 1 sun illumination. Obviously, both photocurrent and photovoltage were improved with the improvement of the level of nanocrystalline interconnection, suggesting that amorphous interconnection has lower collec-

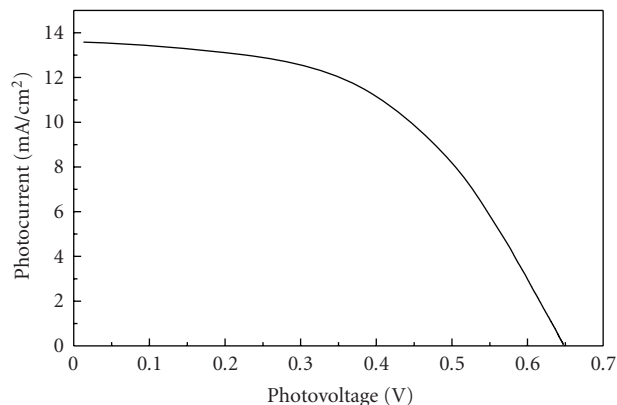


FIGURE 3: Photocurrent-voltage characteristic of a cell based on the amorphous shell/nanocrystalline core nanostructured TiO₂ electrode after sintering. Light intensity was 100 mW/cm². Electrode area was 0.28 cm².

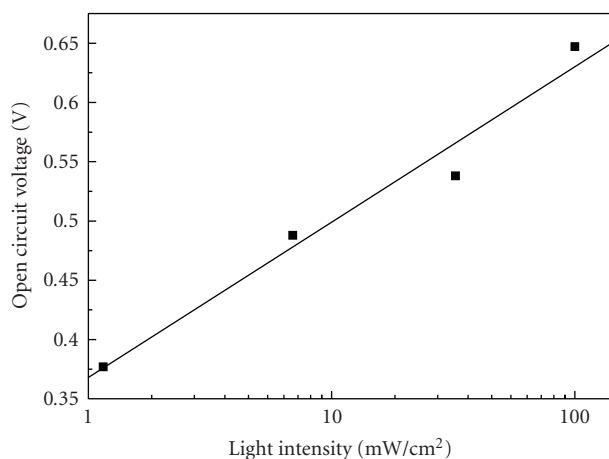


FIGURE 4: Open circuit voltage as a function of incident light intensity for N3-sensitized amorphous shell-nanocrystalline core nanostructured TiO₂ electrode.

tion efficiency of electrons and higher recombination rates of electrons. The unchanged fill factor implies that amorphous interconnection has close resistance in the real cell when it works. The lower photocurrent and photovoltage should come from the higher surface states in the amorphous shell which worked as interconnection.

In summary, amorphous TiO₂ can effectively work as interconnection to form robust nanostructured films, however, it is not effective for electron collection. It presented large recombination rate of electrons comparing with nanocrystalline porous films with nanocrystalline interconnection. It is suggested that low-temperature preparation methods should improve the crystal lever of the interconnection, which plays essential roles in the forming of film and chemical reaction in the interface, while it is not easy to achieve at low temperature. The flexible DSSCs would present as high conversion efficiency as that of sintered DSSCs when it would be achieved.

ACKNOWLEDGMENTS

The research fund from Chemat Technology Inc. is acknowledged. Donglu Shi and Lifeng Li are grateful to the support from the Chinese Academy of Sciences, and Chinese Oversea Outstanding Scholar Foundation (2005-2-9).

REFERENCES

- [1] B. O'Regan and M. Grätzel, "A low-cost, high-efficiency solar cell based on dye-sensitized colloidal TiO₂ films," *Nature*, vol. 353, no. 6346, pp. 737–740, 1991.
- [2] M. K. Nazeeruddin, A. Kay, I. Rodicio, et al., "Conversion of light to electricity by *cis*-X₂bis(2,2'-bipyridyl-4,4'-dicarboxylate)ruthenium(II) charge-transfer sensitizers (X = Cl⁻, Br⁻, I⁻, CN⁻, and SCN⁻) on nanocrystalline TiO₂ electrodes," *Journal of the American Chemical Society*, vol. 115, no. 14, pp. 6382–6390, 1993.
- [3] T. Yoshida, K. Terada, D. Schlettwein, T. Oekermann, T. Sugiura, and H. Minoura, "Electrochemical self-assembly of nanoporous ZnO/Eosin Y thin films and their sensitized photoelectrochemical performance," *Advanced Materials*, vol. 12, no. 16, pp. 1214–1217, 2000.
- [4] C. J. Barbé, F. Arendse, P. Comte, et al., "Nanocrystalline titanium oxide electrodes for photovoltaic applications," *Journal of the American Ceramic Society*, vol. 80, no. 12, pp. 3157–3171, 1997.
- [5] F. Pichot, J. R. Pitts, and B. A. Gregg, "Low-temperature sintering of TiO₂ colloids: application to flexible dye-sensitized solar cells," *Langmuir*, vol. 16, no. 13, pp. 5626–5630, 2000.
- [6] C. Longo, A. F. Nogueira, M.-A. De Paoli, and H. Cachet, "Solid-state and flexible dye-sensitized TiO₂ solar cells: a study by electrochemical impedance spectroscopy," *Journal of Physical Chemistry B*, vol. 106, no. 23, pp. 5925–5930, 2002.
- [7] H. Lindström, A. Holmberg, E. Magnusson, S.-E. Lindquist, L. Malmqvist, and A. Hagfeldt, "A new method for manufacturing nanostructured electrodes on plastic substrates," *Nano Letters*, vol. 1, no. 2, pp. 97–100, 2001.
- [8] S. A. Haque, E. Palomares, H. M. Upadhyaya, et al., "Flexible dye sensitised nanocrystalline semiconductor solar cells," *Chemical Communications*, no. 24, pp. 3008–3009, 2003.
- [9] T. Miyasaka, Y. Kijitori, T. N. Murakami, M. Kimura, and S. Uegusa, "Efficient nonsintering type dye-sensitized photocells based on electrophoretically deposited TiO₂ layers," *Chemistry Letters*, vol. 31, no. 12, p. 1250, 2002.
- [10] S. Uchida, M. Tomiha, H. Takizawa, and M. Kawaraya, "Flexible dye-sensitized solar cells by 28 GHz microwave irradiation," *Journal of Photochemistry and Photobiology A*, vol. 164, no. 1–3, pp. 93–96, 2004.
- [11] T. Kado, M. Yamaguchi, Y. Yamada, and S. Hayase, "Low temperature preparation of nano-porous TiO₂ layers for plastic dye sensitized solar cells," *Chemistry Letters*, vol. 32, no. 11, p. 1056, 2003.
- [12] T. N. Murakami, Y. Kijitori, N. Kawashima, and T. Miyasaka, "UV light-assisted chemical vapor deposition of TiO₂ for efficiency development at dye-sensitized mesoporous layers on plastic film electrodes," *Chemistry Letters*, vol. 32, no. 11, p. 1076, 2003.
- [13] D. Zhang, T. Yoshida, and H. Minoura, "Low-temperature fabrication of efficient porous titania photoelectrodes by hydrothermal crystallization at the solid/gas interface," *Advanced Materials*, vol. 15, no. 10, pp. 814–817, 2003.
- [14] D. Zhang, T. Yoshida, and H. Minoura, "Low temperature synthesis of porous nanocrystalline TiO₂ thick film for dye-sensitized solar cells by hydrothermal crystallization," *Chemistry Letters*, vol. 31, no. 9, p. 874, 2002.
- [15] Y. Liu, A. Hagfeldt, X.-R. Xiao, and S.-E. Lindquist, "Investigation of influence of redox species on the interfacial energetics of a dye-sensitized nanoporous TiO₂ solar cell," *Solar Energy Materials and Solar Cells*, vol. 55, no. 3, pp. 267–281, 1998.
- [16] S. Y. Huang, G. Schlichthörl, A. J. Nozik, M. Grätzel, and A. J. Frank, "Charge recombination in dye-sensitized nanocrystalline TiO₂ solar cells," *Journal of Physical Chemistry B*, vol. 101, no. 14, pp. 2576–2582, 1997.
- [17] S. Sodergerm, A. Hagfeldt, J. Olsson, and S.-E. Lindquist, "Theoretical models for the action spectrum and the current-voltage characteristics of microporous semiconductor films in photoelectrochemical cells," *Journal of Physical Chemistry*, vol. 98, no. 21, pp. 5552–5556, 1994.

Research Article

Nanostructural Organization of Naturally Occurring Composites—Part II: Silica-Chitin-Based Biocomposites

Hermann Ehrlich,¹ Dorte Janussen,² Paul Simon,³ Vasily V. Bazhenov,⁴
Nikolay P. Shapkin,⁴ Christiane Erler,¹ Michael Mertig,¹ René Born,¹ Sascha Heinemann,¹
Thomas Hanke,¹ Hartmut Worch,¹ and John N. Vournakis⁵

¹Max Bergmann Center of Biomaterials and Institute of Materials Science, Dresden University of Technology, 01069 Dresden, Germany

²Forschungsinstitut und Naturmuseum Senckenberg, Senckenberganlage 25, 60325 Frankfurt am Main, Germany

³Max Planck Institute of Chemical Physics of Solids, 01187 Dresden, Germany

⁴Institute of Chemistry and Applied Ecology, Far Eastern National University, 690650 Vladivostok, Russia

⁵Marine Polymer Technologies, Inc., Danvers, MA 01923, USA

Correspondence should be addressed to Hermann Ehrlich, hermann.ehrlich@tu-dresden.de

Received 2 November 2007; Accepted 26 February 2008

Recommended by Donglu Shi

Investigations of the micro- and nanostructures and chemical composition of the sponge skeletons as examples for natural structural biocomposites are of fundamental scientific relevance. Recently, we show that some demosponges (*Verongula gigantea*, *Aplysina* sp.) and glass sponges (*Farrea occa*, *Euplectella aspergillum*) possess chitin as a component of their skeletons. The main practical approach we used for chitin isolation was based on alkali treatment of corresponding external layers of spicules sponge material with the aim of obtaining alkali-resistant compounds for detailed analysis. Here, we present a detailed study of the structural and physicochemical properties of spicules of the glass sponge *Rossella fibulata*. The structural similarity of chitin derived from this sponge to invertebrate alpha chitin has been confirmed by us unambiguously using physicochemical and biochemical methods. This is the first report of a silica-chitin composite biomaterial found in *Rossella species*. Finally, the present work includes a discussion related to strategies for the practical application of silica-chitin-based composites as biomaterials.

Copyright © 2008 Hermann Ehrlich et al. This is an open access article distributed under the Creative Commons Attribution License, which permits unrestricted use, distribution, and reproduction in any medium, provided the original work is properly cited.

1. INTRODUCTION

This is the second paper on naturally occurring silica-based biocomposites of sponges origin. The initial paper [1] studied the presence of fibrillar collagen as a component of glassy anchoring spicule of *Monorhaphis* sp. glass sponge.

Biocomposites of marine origin including sponge skeletal formations are a constant source of inspiration for finding solutions to a variety of technical challenges in bionics, architecture, optics, engineering, as well as materials science and biomedicine (reviewed in [2, 3]). The biomimetic potential of marine sponges seems to be a goldmine to material scientists. Several main aspects relating to sponges as biomaterials and biocomposites are recently described as follows [3]:

(i) hexactinellid spicules as natural glass-based composites with specific mechanical properties [4, 5];

(ii) skeleton of *Euplectella* sp. (Hexactinellida) as a hierarchical natural structural material of remarkable design [6, 7];

(iii) basal spicules of Hexactinellida as biological glass fibers with specific optical properties [8–10];

(iv) silicatein-based biocatalytic formation of nanocomposite materials (reviewed in [11]);

(v) biomimetically inspired hybrid materials based on sili-cified sponge collagen [12–14].

In case of hexactinellid spicules, it is reported that they are highly flexible and tough, possibly not only because of their layered structure and the hydrated nature of the silica as suggested earlier [15], but of the presence of collagen [16] or chitin [17]. According to paleontological and molecular data, the sponge class Hexactinellida may be the oldest

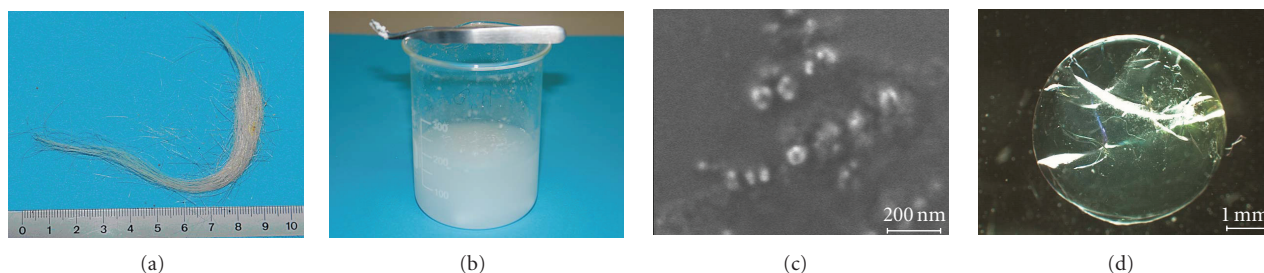


FIGURE 1: Highly flexible spicules of marine glass sponge *Rossella fibulata* (a). Pieces of clean spicules were placed in deionized water and disrupted using magnet stirrer. Visual observations show that the water solution became of a milky color typical for colloidal suspensions of silica (b). Silica nanoparticles are associated around oriented organic matrix of nanofibrillar nature (c). Transparent hard glassy spheres were obtained using this fraction of colloidal suspension after dropping into 99% TMOS solution at room temperature (d).

metazoan taxon in earth's history [18, 19]. Recently, we suggested that silica-chitin scaffolds may be key templates for skeleton formation also in ancestral unicellular organisms, rather than silica-protein composites [17]. From this point of view, we hypothesized that chitin molecules are probably part of very old organic template system involved in a biosilicification phenomenon, which was established a long time before the origin of glass sponges and collagen as structural protein with respect to high templating activity for biomineralization.

The objective of the current study was to test the hypothesis that chitin is an essential component of the silica spicules of Antarctic glass sponge *Rossella fibulata* (Figure 1(a)) as well, and if so, to unravel its involvement in the mechanical behavior of these spicules. Nanomechanical properties, nanohardness and elastic modulus, of a closely related sponge *Rossella racovitzea* were determined previously by using a vertical indentation system attached to an atomic force microscope [15]. The *Rossella* spicules, known to have optical wave conduction properties, are 10–20 cm long with a circular cross-section of diameter 200–600 μm . The spicules are composed of 2–10 μm -thick layers of siliceous material that has no detectable crystallinity. Measurements through the thickness of the spicules indicated uniform properties regardless of layering. Both the elastic modulus and nanohardness values of the spicules are about half of that of either fused silica or commercial glass optical fibers. The fracture strength and fracture energy of the spicules, determined by 3-point bend tests, are several times those of silica rods of similar diameter. The spicules offer bioinspired lessons for potential biomimetic design of optical fibers with long-term durability that could potentially be fabricated at room temperature in aqueous solutions [8]. Unfortunately, the nature and origin of organic matrix were not investigated in these pioneering studies.

We decided also to re-examine the results of some previously reported studies concerning the presence of polysaccharides within silica-containing spicules of another hexactinellid sponge. For example, Travis et al. [20] reported the presence of parallel-oriented cellulose-like filaments with an average width of 1.9 nm observed in organic matrix material after HF-based desilicification of the spicules of hexactinellid

Euplectella sp. These matrices also contain considerable amounts of hexosamine.

In this study, we performed structural, spectroscopic, and biochemical analysis of organic matrix isolated from spicules of *R. fibulata*. Finally, the present work includes a discussion relating to strategies for the practical application of silica-chitin- and silica- N-acetyl glucosamine (NAG)-based composites as biomaterials.

2. EXPERIMENTAL

2.1. Chemical etching of glass sponge skeletons

The object of our study was *Rossella fibulata* Schulze & Kirkpatrick, 1910 (Hexactinellida: Porifera), collected in 2005 in the Scotia Sea, Antarctic, at a depth of 200 m.

Spicules of *R. fibulata* were treated according to the following procedure. Sponge material of *R. fibulata* was stored for several days in fresh sea-water. The sponge was dried afterwards for 4 days at 45°C. Finally, the sponge skeleton was cleaned in 10% H_2O_2 and dried again at 45°C. Tissue-free dried sponge material was washed three times in distilled water, cut into 3 cm long pieces and placed in a solution containing purified *Clostridium histolyticum* collagenase (Sigma Aldrich, Saint Louis, USA) to digest any possible collagen contamination of exogenous nature. After incubation for 24 hours at 15°C, the pieces of glass sponge skeleton were again washed three times in distilled water, dried, and placed in a 15 mL vessel containing chitinase solution (as described below) to digest any possible exogenous chitin contaminations. After incubation for 48 hours at 25°C, fragments of skeleton were again washed, dried, and placed in 10 mL plastic vessel containing 8 mL 2.5 M NaOH solution. The vessel was covered and placed under thermostatic conditions at 37°C without shaking.

The effectiveness of the alkali etching was also monitored using optical and scanning electron microscopy (SEM) at different locations along the length of the spicular material and within the cross-sectional area. The colourless alkali-insoluble material obtained after alkali treatment of the glass sponge samples was washed with distilled water five times and finally dialysed against deionized water on Roth

(Germany) membranes with a MWCO of 14 kDa. Dialysis was performed for 5 days at 4°C. The dialyzed material was dried at room temperature and used for structural and analytical investigations.

2.2. Development of the silica nanoparticulate fraction using mechanical disruption of cleaned *R. fibulata* spicules.

The spicules of *R. fibulata* were treated using enzymes as described above, cleaned, dialyzed, and cut in 3 cm long pieces. These fragments of clean spicules were placed in deionized water and disrupted mechanically using glass covered stirring bars (25 × 6 mm) and magnet stirrer during 24 hours at 25°C. After centrifugation (1500 × g) for 5 minutes the debris of mechanically disrupted spicules was collected and milky colour supernatant was carefully decanted. Obtained debris-free suspension (Figure 1(b)) was used for SEM and TEM investigations.

2.3. FTIR spectroscopy

IR spectra were recorded with a Perkin Elmer FTIR Spectrometer Spectrum 2000, equipped with an AutoImage Microscope using the FT-IRRAS technique (Fourier transform infrared reflection absorption spectroscopy) as described previously [21].

2.4. Transmission electron microscopy (TEM)

Conventional transmission electron microscopy [1] was performed with a Philips CM200 FEG\ST Lorentz electron microscope at an acceleration voltage of 200 kV. For electron microscopy, a drop of the water suspension containing the sample was placed on the electron microscopy grid. After one minute, the excess was removed using blotting paper and thereafter dried in air. The electron microscopy grids (Plano, Germany) were covered with a holey carbon film.

2.5. Scanning electron microscopy (SEM) analysis

The samples were fixed in a sample holder and covered with carbon, or with a gold layer for 1 minute using an Edwards S150B sputter coater. The samples were then placed in an ESEM XL 30 Philips or LEO DSM 982 Gemini scanning electron microscope.

2.6. Chitinase digestion and test

Dried 20 mg samples of purified sponge spicules, previously pulverized to a fine powder in an agat mortar, were suspended in 400 µL of 0.2 M phosphate buffer at pH 6.5. Positive control was prepared by solubilizing 0.3% colloidal chitin in the same buffer. Equal amounts of 1 mg/mL of three chitinases (EC 3.2.1.14 and EC 3.2.1.30): N-acetyl-β-glucosaminidase from *Trichoderma viride* (Sigma-Aldrich) number C-8241, and two poly (1,4-β-[2-acetamido-2-deoxy-D-glucoside]) glycanohydrolases from *Serratia marcescens* (Sigma-Aldrich) number. C-7809 and *Streptomyces*

griseus (Sigma-Aldrich) number. C-6137, respectively, were suspended in 100 mM sodium phosphate buffer at pH 6.0. Digestion was started by mixing 400 µL of the samples and 400 µL of the chitinase-mix. Incubation was performed at 37°C and stopped after 114 hours by adding 400 µL of 1% NaOH, followed by boiling for 5 minutes. The effectiveness of the enzymatic degradation was monitored using optical microscopy (Zeis, Axiovert). The Morgan-Elson assay was used to quantify the N-acetylglucosamin released after chitinase treatment as described previously [22]. The sample which contains chitinase solution without substrate was used as a control.

2.7. Preparation of α-chitin

Alpha-chitin was prepared from a commercially available crab shell chitin (Fluka). The material was purified with aqueous 1 M HCl for 2 hours at 25°C and then refluxed in 2 M NaOH for 48 hours at 25°C. The resulting α-chitin was washed in deionized water by several centrifugations until neutrality was reached. The whole procedure was repeated twice. α-chitin was also used as a standard for FTIR and for Fourier transform (HRTEM) studies.

2.8. Preparation of colloidal chitin

Ten grams of α-chitin (Fluka) was mixed with 500 mL of 85% phosphoric acid and stirred for 24 hours at 4°C. The suspension was poured into 5 L of distilled water (DW) and centrifuged (15000 × g for 15 minutes). The resulting precipitate was washed with DW until the pH reached 5.0 and then neutralized by addition of 6 N NaOH. The suspension was centrifuged (15000 × g for 15 minutes) and washed with 3 L of DW for desalting. The resulting precipitate was suspended in DW and dialyzed. The chitin content in the suspension was determined by drying a sample.

2.9. Silicification of colloidal chitin and NAG

In the first step, 0.93 g of colloidal chitin or NAG (Sigma-Aldrich, Miss, USA) previously suspended in 34.6 g of methanol was added to 51.8 mL of deionized water. The suspension pH was then raised above 10 with the addition of 100 µL of 1 N NaOH solution. Finally, 169 µL of tetramethylorthosilicate (TMOS, 99 wt%, ABCR GmbH, Germany) were added and the solution was stirred at room temperature. After 1 hour the suspension was filtered and the recovered precipitate rinsed with deionized water, then with methanol, and finally air-dried.

3. RESULTS AND DISCUSSION

Most of the glass sponges inhabit soft muddy substrates. One of the strategies of survival under such conditions is the formation of root structures that prevent the body of the animal from sinking into the ground [23]. Due to their preferred deep-sea habitat, the Hexactinellida have been poorly investigated with respect to their general biology [24, 25] and the nature of organic components which build their skeletal

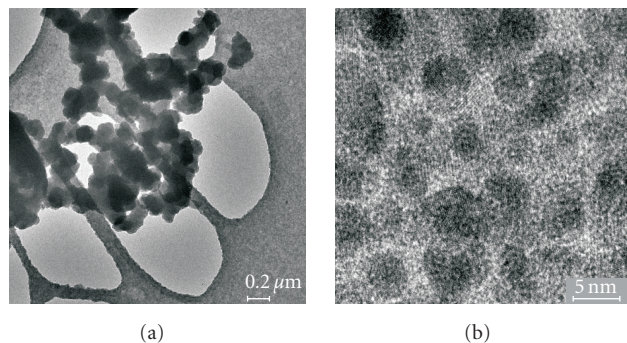


FIGURE 2: TEM images of silica-organic matrix-based suspension obtained after mechanical disruption of spicules in deionized water (a). Crystallites of organic nature are embedded in amorphous silica (b).

structures. It was generally accepted that their skeletons are composed of concentric layers of amorphous hydrated silica, containing varying amounts of organic material [26, 27] deposited around a proteinaceous axial filament [28, 29].

The finding of collagen within basal spicules of *H. sieboldi* [12, 16] and chitin in skeletons of *F. occa* [17] and in spicules of *E. aspergillum* [3], stimulated our attempts to find materials of organic nature in other species of glass sponges. In the case of *R. fibulata*, we have not observed any visible signs of demineralization of these materials using optical microscopy and SEM after 14 days and at the similar experimental conditions as in the study on *H. sieboldi* and *Monorhaphis sp.* On the contrary, spicules of *R. fibulata* show high resistance to alkali treatment even after 3 months of demineralization. This was similar the resistance observed for *E. aspergillum* [3]. This phenomenon led us to the assumption that siliceous skeletons of investigated sponges possess a material which protects amorphous silica from dissolution in alkali, and is highly resistant to alkali digestion. It is well known that chitin in alkali is stable with respect to degradation [30]. Correspondingly, in our experiments, chitin was the first candidate for a biomaterial with this property.

Initially, we performed experiments on mechanical disruption of cleaned *R. fibulata* spicules (Figure 1(a)) in deionized water as described above. This method of desintegration of spicules was very effective. Visual observations show that water solution became of a milky color typical for silica colloidal suspensions (Figure 1(b)) even after 6 hours. Debris-free suspensions obtained in this way were stable during 3-4 days. SEM of the suspensions confirmed their nanoparticulate structure (Figure 1(c)). Silica nanoparticles of diameter between 20 and 35 nm are associated around oriented organic matrix of nanofibrillar nature as shown in Figure 1(c). To verify whether this kind of silica-organic matrix obtained from the colloidal suspension mimic the biosilicification, we carried out in vitro experiments in which we exposed it to silicic acid solution derived from TMOS. We developed hard and transparent glassy spheres (Figure 1(d)) which were stable in water and in air during several months.

TEM investigation of these colloidal suspensions (Figure 2(a)) used for the development of spherical glassy

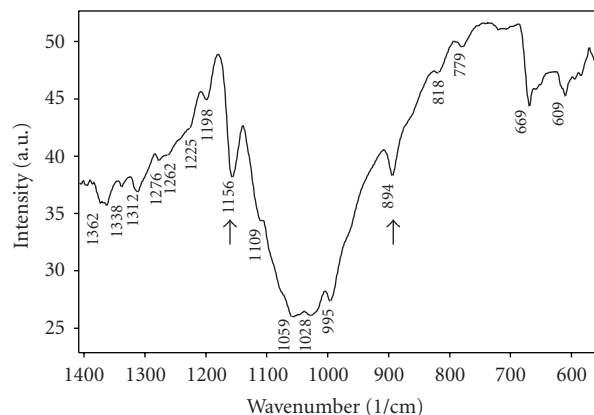


FIGURE 3: FTIR spectra of organic matrix isolated after desilicification of *R. fibulata* spicules show strong evidence for β -1, 4-glycosidic linkage at 890–896 cm^{-1} and for ether bond in pyranose ring at 1153–1157 cm^{-1} (arrows). There is no evidence for the presence of Si–O–Si bonds.

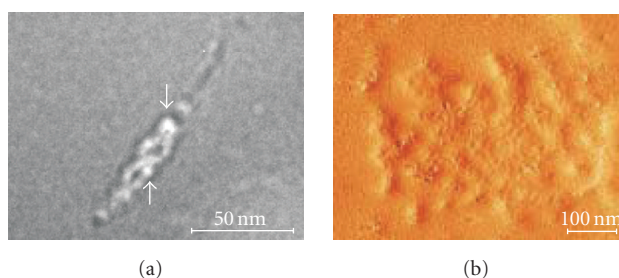


FIGURE 4: High-resolution transmission electron microscopy image of the fragment of isolated chitin nanofibril (a); the arrows indicate the presence of crystallite-like structures with a diameter which corresponds to that of chitin crystallites (2 nm). AFM micrograph of chitin nanofibrillar matrix (b).

materials clearly revealed that organic crystallites of approximately 3 nm in diameter are embedded in amorphous silica matrix. Observed HRTEM image (Figure 2(b)) is highly similar to previously reported HRTEM images of chitin nanocrystallites of the same diameter [31]. Therefore, in following experiments it was decided to isolate organic matrix from silica-containing spicules of *R. fibulata* using a desilicification procedure based on alkali treatment [16, 17].

To test our hypothesis that alkali-insoluble residues of *R. fibulata* spicules are of chitinous nature, we carried out different highly sensitive structural and biochemical analysis as described below.

FTIR observation of purified, dialysed, and dried samples of the alkali-insoluble organic matrix isolated after demineralization of *R. fibulata* spicules (Figure 3) confirmed occurrence of pyranose rings and β -1, 4 linkages, with peaks at 1156 cm^{-1} and at 894 cm^{-1} very similar to those of α -chitin. It was reported previously that the spectral feature between 1153 and 1157 cm^{-1} is mainly associated with an ether bond in a pyranose ring [32, 33]. The β -linkage was also indicated

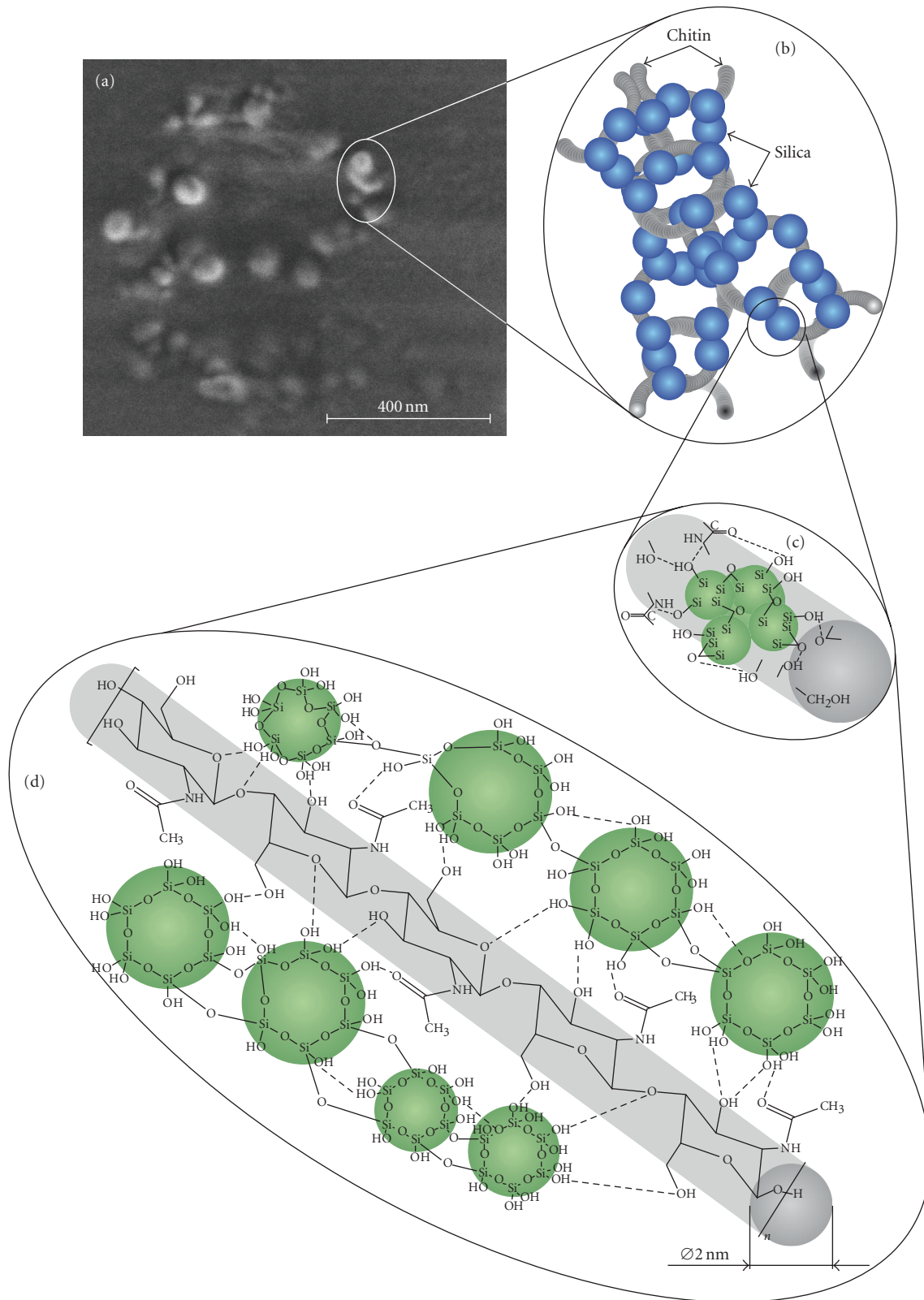


FIGURE 5: Proposed model of nanostructural organization of the naturally occurring silica-chitin composite unit (a) isolated from spicules of *R. fibulata*. Silica nanoparticles tightly surround chitinous nanofibrils (b). Schematic view (c) shows a possible nanodistribution of silica on the surface of chitinous nanofibril. Image (d) represents the hypothesized scheme of interaction between silica and poly-N-acetyl glucosamine-fragment of the chitin nanofibril and formation of the corresponding hydrogen bonds.

by the infrared absorption, in which a typical peak at $890\text{--}892\text{ cm}^{-1}$ for α -chitin was observed [34, 35].

In recent years, high-resolution electron microscopy has proved to be an important tool for analysis of the structure of fibrous crystalline polysaccharides, such as cellulose and chitin [36–39]. Therefore, the samples of organic matrix used for FTIR were subsequently submitted to HR-TEM analyses in order to examine the crystalline nature of this material and the plausible additional occurrence of chitin. HRTEM and AFM studies (Figures 4(a) and 4(b), resp.) of the organic matrix residue obtained after demineralization of *R. fibulata* spicules revealed the presence of nanocrystallites having a diameter of 2 nm. These structures were extremely similar to those previously reported by TEM observations of chitinous skeletal formations in insects, crustaceans, and arachnid species [40–42]. For further examination, high-resolution electron micrographs were taken from particular sample regions (data not shown). The Fourier transform of the high-resolution micrograph revealed a spacing of 4.79 \AA (a -axis), 10.2 \AA (fiber axis), 3.73 \AA , and 2.77 \AA . Such distances, corresponded to [(100) (040)], (001), [(130), (050)], and [(103), (043) (113)] reflections, proving the orthorhombic structure typical for α -chitin, as described in detail by Carlström [34] and Minke and Blackwell [42]. These measurements confirm our earlier observations [17, 21] that chitin in marine sponges appear to be consistently in the α -modification.

To quantify chitin in our samples, we measured the amount of N-acetyl glucosamine released by chitinases using a Morgan-Elson colorimetric assay [22], which is the most reliable method for the identification of alkali-insoluble chitin because of its specificity [43]. We detected $19.2 \pm 1.5\text{ }\mu\text{g}$ N-acetyl-glucosamine per mg of spicule of *R. fibulata*.

The finding of silica-chitin natural composites as the component of the *R. fibulata* spicules is in good agreement with results of *in vitro* experiments on silicification of a β -chitin-containing cuttlebone-derived organic matrix as reported by Ogasawara et al. [44]. These authors suggest that silicate ions and silica oligomers preferentially interact with glycopyranose rings exposed at the β -chitin surface, presumably by polar and H-bonding interactions. We believe that chitin is acting as an organic template for silica mineralization in *Rossella* species in a very similar fashion as in *F. occa* [17] and *E. aspergillum* [3]. On the basis of the results presented in this work, we propose a model for the nanostructure of the naturally occurring silica-chitin composite unit, including interaction between poly-N-acetyl glucosamine-fragment of the chitin nanofibril and silica nanoparticles, which can be seen in Figure 5.

Because sponges are often regarded as the most ancient metazoans (630 to 542 My) [45, 46], the finding of chitin within skeletal formations of these organisms is of major scientific significance, since it gives important indications to the basic pattern of the Metazoa. As chitin also serves as a template for calcium carbonate deposition in sponges [21], this suggests that the evolution of mineralized skeletons in early metazoans share a common origin with respect to chitin as a unified template for biomineralization, similar to collagen as common structural protein in nature [12]. This feature

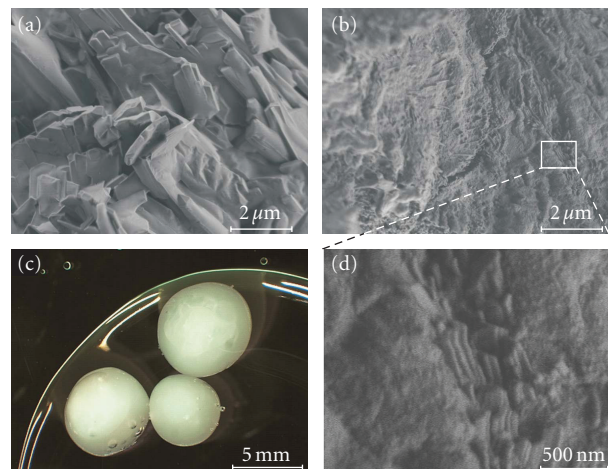


FIGURE 6: Crystals of N-acetyl glucosamine obtained from solution (a) could be also visualized using SEM even if being included into amorphous silica matrix (b). SEM image (d) revealed strong evidence that oriented crystals of NAG are observed in form of nanocrystals compactly embedded within this matrix. Light micrograph (c) of the silica-NAG spherical composites, which are highly stable in water-containing solutions.

may be considered a basic metazoan character and thus also has implications for the question of establishing the monophyletic status of the taxon Metazoa.

A comprehensive understanding of silica-chitin-based sponge skeletons with respect to chemical composition and structure may prove to be a novel model for the biomimetic synthesis also of N-acetyl glucosamine (NAG) and poly-NAG-based composites analogous to well established chitosan-silica hybrid materials [47, 48] with very attractive bioactive properties for applications in biomedicine. It was reported [49] that silicon was found to be a constituent of certain glycosaminoglycans. It was concluded that Si is present as silanolate, that is, an ether (or ester-like) derivative of orthosilicic acid, and that $R_1\text{--O--Si--O--}R_2$ bridges play a role in the structural organisation of glycosaminoglycans. Thus Si may function as a biological cross-linking agent and contribute to architecture and resilience of connective tissue [49].

To test our hypothesis that also NAG as monomer unit of poly-NAG and chitin could be used as substrate for silicification, we obtained silica-NAG-based materials in the form of rods or spheres (Figure 6) using TMOS and sol-gel techniques *in vitro* as described in Section 2. The diameter of these spheres could be varied between 2 and 10 μm . SEM investigations on micro- and nanostructural organization of silica-NAG composites revealed strong evidence that oriented nanocrystals of NAG (Figure 6(a)) could be also observed in form of nanocrystals compactly embedded within amorphous silica matrix (Figures 6(b) and 6(d)). Probably this kind of NAG nanodistribution is responsible for observed high mechanical stability and resistance of these composite materials to swelling and following dissolution in water containing solutions (Figure 6(c)). These properties could be probably of interest for technical purposes similar to

intercalated chitosan/layered silicate nanocomposites prepared to develop robust and stable sensors useful for anionic detection in aqueous media as reported on [50, 51].

We suggest that silica-chitin and silica-NAG (-poly NAG) composites could be highly optimized biocompatible structures that would support and organize functional tissues if applied in tissue engineering of bone and cartilage replacements similar to silica-chitosan-based biomaterials [52]. Experiments on biocompatibility of silica-chitin and silica-NAG composites derived in vitro are currently in progress.

4. CONCLUSION

Chitin and poly-N-acetyl glucosamine are well investigated materials of biological origin with wide fields of application in biomedicine because of their unique multifunctional engineering mechanical properties and biocompatibility [53–56]. With respect to polysaccharides, including sponge chitin, it is theoretically possible that inorganic Si binds after the macromolecular structure has been formed. An alternative, more plausible from stereochemical considerations [49], would consist in the incorporation of preformed mono- or disaccharide Si derivatives during the synthesis of the polysaccharide chain. The finding of nanostructured silica-chitin biocomposites as structural scaffolds of glass sponge skeletons introduces a new aspect into the discussion surrounding the chemistry, diversity, and nanolocalization of these materials. Chitin as a template for biomineralization probably belongs to the basic pattern of the Metazoa.

ACKNOWLEDGMENTS

This work was partially supported by a joint Russian-German program “DAAD-Mikhail Lomonosov.” We thank Professor H. Lichte for the possibility to use the facilities at the Special Electron Microscopy Laboratory for high-resolution and holography at Triebenberg, TU Dresden, Germany. The authors are deeply grateful to Mariana Tasso, Heike Meissner, Gert Richter, Axel Mensch, and Ortrud Trommer for helpful technical assistance.

REFERENCES

- [1] H. Ehrlich, S. Heinemann, C. Heinemann, et al., “Nanostructural organization of naturally occurring composites. Part I. Silica-collagen-based biocomposites,” *Journal of Nanomaterials*. In press.
- [2] P. Fratzl, “Biomimetic materials research: what can we really learn from nature’s structural materials?” *Journal of the Royal Society, Interface*, vol. 4, no. 15, pp. 637–642, 2007.
- [3] H. Ehrlich and H. Worch, “Sponges as natural composites: from biomimetic potential to development of new biomaterials,” in *Porifera Research-Biodiversity, Innovation & Sustainability*, M. R. Custodio, G. Lobo-Hajdu, E. Hajdu, and G. Muricy, Eds., Museu Nacional, Rio de Janeiro, Brasil, 2007.
- [4] G. Mayer, “Rigid biological systems as models for synthetic composites,” *Science*, vol. 310, no. 5751, pp. 1144–1147, 2005.
- [5] S. L. Walter, B. D. Flinn, and G. Mayer, “Mechanisms of toughening of a natural rigid composite,” *Materials Science and Engineering C*, vol. 27, no. 3, pp. 570–574, 2007.
- [6] J. Aizenberg, J. C. Weaver, M. S. Thanawala, V. C. Sundar, D. E. Morse, and P. Fratzl, “Skeleton of *Euplectella* sp.: structural hierarchy from the nanoscale to the macroscale,” *Science*, vol. 309, no. 5732, pp. 275–278, 2005.
- [7] J. C. Weaver, J. Aizenberg, G. E. Fantner, et al., “Hierarchical assembly of the siliceous skeletal lattice of the hexactinellid sponge *Euplectella aspergillum*,” *Journal of Structural Biology*, vol. 158, no. 1, pp. 93–106, 2007.
- [8] R. Cuttaneo-Vietti, G. Bavestrello, C. Cerrano, et al., “Optical fibres in an Antarctic sponge,” *Nature*, vol. 383, no. 6599, pp. 397–398, 1996.
- [9] J. Aizenberg, V. C. Sundar, A. D. Yablon, J. C. Weaver, and G. Chen, “Biological glass fibers: correlation between optical and structural properties,” *Proceedings of the National Academy of Sciences of the United States of America*, vol. 101, no. 10, pp. 3358–3363, 2004.
- [10] W. E. G. Müller, K. Wendt, C. Geppert, M. Wiens, A. Reiber, and H. C. Schröder, “Novel photoreception system in sponges? Unique transmission properties of the stalk spicules from the hexactinellid *Hyalonema sieboldi*,” *Biosensors and Bioelectronics*, vol. 21, no. 7, pp. 1149–1155, 2006.
- [11] H. C. Schröder, D. Brandt, U. Schloßmacher, et al., “Enzymatic production of biosilica glass using enzymes from sponges: basic aspects and application in nanobiotechnology (material sciences and medicine),” *Naturwissenschaften*, vol. 94, no. 5, pp. 339–359, 2007.
- [12] H. Ehrlich and H. Worch, “Collagen, a huge matrix in glass-sponge flexible spicules of the meter-long *Hyalonema sieboldi*,” in *Handbook of Biomineralization Vol.1. The Biology of Biominerals Structure Formation*, E. Bäuerlein, Ed., Wiley VCH, Weinheim, Germany, 2007.
- [13] S. Heinemann, H. Ehrlich, C. Knieb, and T. Hanke, “Biomimetically inspired hybrid materials based on silicified collagen,” *International Journal of Materials Research*, vol. 98, no. 7, pp. 603–608, 2007.
- [14] S. Heinemann, C. Knieb, H. Ehrlich, et al., “A novel biomimetic hybrid material made of silicified collagen: perspectives for bone replacement,” *Advanced Engineering Materials*, vol. 9, no. 12, pp. 1061–1068, 2007.
- [15] M. Sarikaya, H. Fong, N. Sunderland, et al., “Biomimetic model of a sponge-spicular optical fiber-mechanical properties and structure,” *Journal of Materials Research*, vol. 16, no. 5, pp. 1420–1428, 2001.
- [16] H. Ehrlich, A. Ereskovsky, A. L. Drozdov, et al., “A modern approach to demineralization of spicules in glass sponges (Porifera: Hexactinellida) for the purpose of extraction and examination of the protein matrix,” *Russian Journal of Marine Biology*, vol. 32, no. 3, pp. 186–193, 2006.
- [17] H. Ehrlich, M. Krautter, T. Hanke, et al., “First evidence of the presence of chitin in skeletons of marine sponges. Part II. Glass sponges (Hexactinellida: Porifera),” *Journal of Experimental Zoology Part B*, vol. 308B, no. 4, pp. 473–483, 2007.
- [18] J. Reitner and D. Mehl, “Early Paleozoic diversification of sponges: new data and evidences,” *Geologisch Paläontologische Mitteilungen Innsbruck*, vol. 20, pp. 335–347, 1995.
- [19] J. P. Botting and N. J. Butterfield, “Reconstructing early sponge relationships by using the Burgess Shale fossil *Eiffelia globosa*, Walcott,” *Proceedings of the National Academy of Sciences of the United States of America*, vol. 102, no. 5, pp. 1554–1559, 2005.
- [20] D. F. Travis, C. J. Francois, L. C. Bonar, and M. J. Glimcher, “Comparative studies of the organic matrices of invertebrate mineralized tissues,” *Journal of Ultrastructure Research*, vol. 18, no. 5–6, pp. 519–550, 1967.

- [21] H. Ehrlich, M. Maldonado, K.-D. Spindler, et al., "First evidence of chitin as a component of the skeletal fibers of marine sponges. Part I. Verongidae (Demospongia: Porifera)," *Journal of Experimental Zoology Part B*, vol. 308B, no. 4, pp. 347–356, 2007.
- [22] N. Boden, U. Sommer, and K.-D. Spindler, "Demonstration and characterization of chitinases in the *Drosophila* K_c cell line," *Insect Biochemistry*, vol. 15, no. 1, pp. 19–23, 1985.
- [23] K. Tabachnik, "Adaptation of the hexactinellid sponges to deep-sea life," in *Fossil and Recent Sponges*, J. Reitner and H. Keupp, Eds., pp. 378–386, Springer, Berlin, Germany, 1991.
- [24] H. M. Reiswig and D. Mehl, "Tissue organization of *Favosites* (Porifera, Hexactinellida)," *Zoomorphology*, vol. 110, no. 6, pp. 301–311, 1991.
- [25] S. P. Leys, G. O. Mackie, and H. M. Reiswig, "The biology of glass sponges," *Advances in Marine Biology*, vol. 52, pp. 1–145, 2007.
- [26] F. E. Schulze, "Hexactinellida," in *Wissenschaftliche Ergebnisse der Deutschen Tiefsee-Expedition auf dem Dampfer "Valdivia" 1898-1899*, C. Chun, Ed., vol. 4, pp. 1–266, Gustav Fischer, Jena, Germany, 1904.
- [27] C. L. De La Rocha, "Silicon isotope fractionation by marine sponges and the reconstruction of the silicon isotope composition of ancient deep water," *Geology*, vol. 31, no. 5, pp. 423–426, 2003.
- [28] J. C. Weaver and D. E. Morse, "Molecular biology of demosponge axial filaments and their roles in biosilicification," *Microscopy Research and Technique*, vol. 62, no. 4, pp. 356–367, 2003.
- [29] M. J. Uriz, X. Turon, M. A. Becerro, and G. Agell, "Siliceous spicules and skeleton frameworks in sponges: origin, diversity, ultrastructural patterns and biological functions," *Microscopy Research and Technique*, vol. 62, no. 4, pp. 279–299, 2003.
- [30] A. Einbu, S. N. Naess, A. Elgsaeter, and K. M. Varum, "Solution properties of chitin in alkali," *Biomacromolecules*, vol. 5, no. 5, pp. 2048–2054, 2004.
- [31] E. Atkins, "Conformation in polysaccharides and complex carbohydrates," *Journal of Biosciences*, vol. 8, no. 1-2, pp. 375–387, 1985.
- [32] G. Cárdenas, G. Cabrera, E. Taboada, and S. P. Miranda, "Chitin characterization by SEM, FFTIR, XRD, and ¹³C cross polarization/mass angle spinning NMR," *Journal of Applied Polymer Science*, vol. 93, no. 4, pp. 1876–1885, 2004.
- [33] J. Maitan, K. Bilikova, O. Marcovic, et al., "Isolation and characterization of chitin from bumblebee (*Bombus terrestris*)," *International Journal of Biological Macromolecules*, vol. 40, no. 3, pp. 237–241, 2007.
- [34] D. Carlström, "The crystal structure of α -chitin (poly-*N*-acetyl-D-glucosamine)," *Journal of Biophysical and Biochemical Cytology*, vol. 3, no. 5, pp. 669–683, 1957.
- [35] K. Bachmed, F. Quilès, M. Wathier, et al., "Use of dancyl *N*-acetyl glucosamine as substrate for chitin synthetase activities," *Progress Biochemistry*, vol. 40, no. 7, pp. 2523–2529, 2005.
- [36] A. Gemperle, Z. Holan, and V. Pokorny, "The Glucan-chitin complex in *saccharomyces cerevisiae*. IV. The electron diffraction of crustacean and yeast cell wall chitin," *Biopolymers*, vol. 21, no. 1, pp. 1–16, 1982.
- [37] W. Helbert and J. Sagiya, "High-resolution electron microscopy on cellulose II and α -chitin single crystals," *Cellulose*, vol. 5, no. 2, pp. 113–122, 1998.
- [38] M.-M. Giraud-Guille, H. Chanzy, and R. Vuong, "Chitin crystals in arthropod cuticles revealed by diffraction contrast transmission electron microscopy," *Journal of Structural Biology*, vol. 103, no. 3, pp. 232–240, 1990.
- [39] A. C. Neville, D. A. D. Parry, and J. Woodhead-Galloway, "The chitin crystallite in arthropod cuticle," *Journal of Cell Science*, vol. 21, no. 1, pp. 73–82, 1976.
- [40] M.-M. Giraud-Guille, "Plywood structure in nature," *Current Opinion in Solid State & Materials Science*, vol. 3, no. 3, pp. 221–227, 1998.
- [41] J. D. Goodrich and W. T. Winter, " α -chitin nanocrystals prepared from shrimp shells and their specific surface area measurement," *Biomacromolecules*, vol. 8, no. 1, pp. 252–257, 2007.
- [42] R. Minke and J. Blackwell, "The structure of α -chitin," *Journal of Molecular Biology*, vol. 120, no. 2, pp. 167–181, 1969.
- [43] C. E. Bulawa, "Genetics and molecular biology of chitin synthesis in fungi," *Annual Review of Microbiology*, vol. 47, pp. 505–534, 1993.
- [44] W. Ogasawara, W. Shenton, S. A. Davis, and S. Mann, "Template mineralization of ordered macroporous chitin-silica composites using a cuttlebone-derived organic matrix," *Chemistry of Materials*, vol. 12, no. 10, pp. 2835–2837, 2000.
- [45] M. Brasier, O. Green, and G. Shields, "Edicarian sponge spicule clusters from southwestern Mongolia and the origins of the Cambrian fauna," *Geology*, vol. 25, no. 4, pp. 303–306, 1997.
- [46] J. Reitner and D. Mehl, "Monophyly of the taxon Porifera," *Verhandlungen des naturwissenschaftlichen Vereins Hamburg*, vol. 36, pp. 5–32, 1996.
- [47] Y. A. Shchipunov, T. Y. Karpenko, A. V. Krekoten, and I. V. Postnova, "Gelling of otherwise nongelable polysaccharides," *Journal of Colloid and Interface Science*, vol. 287, no. 2, pp. 373–378, 2005.
- [48] Y. Shirosaki, K. Tsuru, S. Hayakawa, et al., "In vitro cytocompatibility of MG63 cells on chitosan-organosiloxane hybrid membranes," *Biomaterials*, vol. 26, no. 5, pp. 485–493, 2005.
- [49] K. Schwarz, "A bound form of silicon in glycosaminoglycans and polyuronides," *Proceedings of the National Academy of Sciences of the United States of America*, vol. 70, no. 5, pp. 1608–1612, 1973.
- [50] M. Darder, M. Colilla, and E. Ruiz-Hitzky, "Biopolymer-clay nanocomposites based on chitosan intercalated in montmorillonite," *Chemistry of Materials*, vol. 15, no. 20, pp. 3774–3780, 2003.
- [51] S. S. Ray and M. Bousmina, "Biodegradable polymers and their layered silicate nanocomposites: in greening the 21st century materials world," *Progress in Materials Science*, vol. 50, no. 8, pp. 962–1079, 2005.
- [52] S. F. Wang, L. Shen, Y. J. Tong, et al., "Biopolymer chitosan/montmorillonite nanocomposites: preparation and characterization," *Polymer Degradation and Stability*, vol. 90, no. 1, pp. 123–131, 2005.
- [53] M. Rinaudo, "Chitin and chitosan: properties and applications," *Progress in Polymer Science*, vol. 31, no. 7, pp. 603–632, 2006.
- [54] J. N. Vournakis, E. R. Pariser, and S. Finkielstein, "Poly-*N*-acetyl glucosamine," US patent no. 5,623,064, 1997.
- [55] J. Vournakis, E. R. Pariser, S. Finkielstein, and M. Helton, "Biocompatible poly-beta-1, 4-*N*-acetyl glucosamine," US patent no. 6,686,342, 2004.
- [56] Q. K. Kang, C. M. Hill, M. V. Demcheva, J. Vournakis, and Y. H. An, "Poly-*N*-acetyl glucosamine-SO₄ for repairing osteochondral defect in rabbits," *Key Engineering Materials*, vol. 288-289, pp. 83–86, 2005.